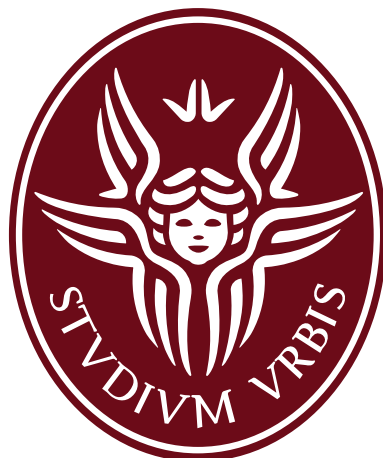


DIRECT NUMERICAL SIMULATION OF TRANSCRITICAL MIXING



A dissertation for Master of Science in
Space and Astronautical Engineering

Advisor:
Prof. Francesco Creta, Ph.D.

Co-advisor:
Pasquale Eduardo Lapenna, Ph.D.

Mechanical and Aerospace Engineering
La Sapienza University of Rome
Via Eudossiana 16, 00185 Rome, Italy

by
SUMAN BASNET
January 2020

Suman Basnet

Direct Numerical Simulation of transcritical mixing

A dissertation submitted in a partial fulfilment of the requirements for the

degree of Master of Science in

Space and Astronautical Engineering

✉ basnet.1772815@studenti.uniroma1.it

© Suman Basnet, January 2020

मेरो परिवारका सबै सदस्यहरु, साथीहरु र शिक्षकहरुप्रति समर्पित ॥

I am an old man now, and when I die and go to heaven there are two matters on which I hope for enlightenment. one is quantum electrodynamics, and the other is the turbulent motion of fluids. And about the former I am rather optimistic.

— British physicist Horace Lamb,

Turbulence is a rule, and not exception in fluid dynamics

— Moin P.

ACKNOWLEDGEMENT

Firstly, I would like to express my gratitude to Prof. Dr. Francesco Creta and Dr. Pasquale E. Lapenna at La Sapienza University of Rome, for allowing me to work alongside them in an exciting state-of-the art DNS database, for their continuous support, encouragement and guidance towards carrying out a quality thesis work. This short period of time has taught me a lot in terms of research and its prospectives, and there is still a long way forward, such learning curve would have been steeper without the help of my mentors. I would like to thank my family, close friends and colleagues who were always there for me throughout the course plus this masters thesis. I would also like to thank my seniors Rachele Lamioni and Giuseppe Indelicato here at La Sapienza for the guidance and support during this thesis work.

Suman Basnet

December 19, 2019

NOMENCLATURE

List of acronyms

CALTECH	California Institute of Technology
CD	Convergent-Divergent
CFD	Computational Fluid Dynamics
CINECA	Italian Super-Computing Inter-university Consortium
CP	Critical Point
DLR	Deutsches Zentrum für Luft- und Raumfahrt
DNS	Direct Numerical Simulation
EoS	Equation of State
FDM	Finite Difference Method
FEM	Finite Element Method
FVM	Finite Volume Method
GN	Gaseous Nitrogen
JPL	Jet Propulsion Laboratory
LES	Large Eddy Simulation
LN	Liquid Nitrogen
LOX-LH₂	Liquid Oxygen - Liquid Hydrogen
LOX-RP1	Liquid Oxygen - Refined Petroleum-1
LRE	Liquid Rocket Engine
NIST	National Institute of Standards and Technology
PB	Pseudo- Boiling
PDE	Partial Differential Equation
PDF	Probability Density Function
PR Eos	Peng - Robinson Equation of State
RANS	Reynolds Averaged Navier-Stokes

RK EoS	Redlich-Kwong Equation of State
SEM	Spectral Element Method
SGS	Sub Grid Scale
SM	Spectral Method
SRK EoS	Soave-Redlich-Kwöng Equation of State
TU	Technical University
URANS	Unsteady Reynolds averaged Navier-Stokes equations
vdW EoS	van der Waals Equation of State (or mixing rule)
3D	Three Dimension

Greek Symbols

α	Thermal diffusivity	m^2/s
δ_{ij}	Kronecker delta	—
ϵ	Dissipation rate of the turbulent k.e.	m^2/s^3
λ	Thermal conductivity	$W/(mK)$
μ	Dynamic Viscosity	Pas
ν	Kinematic viscosity	m^2/s
ω_k	Production rate of species k	$kg/(m^3s)$
ρ	Density	kg/m^3
γ	Specific heat ratio	—
τ_0	Integral time scale	s
ξ	Non-dimensional enthalpy	—
θ	Non-dimensional temperature	—

Roman Symbols

a	Speed of sound	m/s
A_e	Exit area of nozzle	m^2
c	Effective exhaust velocity	m/s
C_c	Isochoric heat capacity	J/kgK
C_F	Thrust coefficient	—
C_p	Isobaric heat capacity	J/kgK

\mathcal{C}	Crosses stresses	—
D_t	Throat diameter	m
e	Specific energy	J/kg
F	Thrust	N
\mathfrak{F}	Body forces	—
g_0	Acceleration due to gravity	m/s^2
h	Enthalpy	J
I_{sp}	Specific impulse	s
k	Turbulent kinetic energy	J
l_k	Kolmogorov lenght scale	m
L_0	Integral length scale	m
\mathcal{L}	Leonard Stresses	—
p_a	Ambient pressure	Pa
p_e	Exit pressure	Pa
q	Heat flux	W/m^2
R	Specific gas constant ($= \mathcal{R}/M_W$)	J/kgK
\mathbb{R}	Universal gas constant	$8314.46J/(molK)$
Re	Reynolds number	—
\mathcal{R}	Reynolds stresses	—
S	Viscous stress tensor	$kg/(ms^2)$
Sc_t	Turbulent Schmidt number	—
t	Time	s
T	Temperature	K
u, v, w	x- y- and z- velocity components	m/s
\dot{W}	Weight flow rate	$N/(m^3)$
Y_k	Mass fraction of species k	—
Z	Compressibility factor	—

Subscripts

\square_a	Value at ambient
\square_c	Value in combustion chamber
\square_{cr}	Value at critical point
\square_{vac}	Value in vacuum
$\dot{\square}$	Rate
\square_e	Value at exit
$\square_{i,j,k}$	Component index along the spatial directions
\square_k	Species index

\square_{max}	Maximum value in the field
\square_{min}	Minimum value in the field
\square_{pb}	Pseudo-boiling
\square_r	Reduced values
\square_{ref}	Reference value
\square_{RMS}	Root mean square value
\square_t	Turbulent property
\square_{tp}	Value at the triple point
\square_x	Property component along x-direction
\square_y	Property component along y-direction
\square_z	Property component along z-direction
\square_∞	Undisturbed flow property (far-field)

Superscripts

$\bar{\square}$	Reynolds mean value
$\tilde{\square}$	Favre mean value
\square'	Fluctuation with respect to Reynolds mean value
\square''	Fluctuation with respect to Favre mean value
\square^+	Upper bound
\square^-	Lower bound
\square^{iG}	Ideal gas
\square^{rG}	Real gas

ABSTRACT

The liquid rocket engine is considered to be one of the efficient rocket engines with considerably large specific impulse and has been an integral part of launch vehicles propelling man-made objects into outer-space ever since its first flight in 1926. In a quest for smaller, efficient and powerful launch vehicle, such engines are designed to operate in an elevated pressure conditions, such that the operating pressure in the combustion chamber is way above the critical point of most of the pure propellants which are usually stored in sub-critical conditions (liquid-state) occupying smaller volume. Because of its compactness and increase in efficiency supercritical working conditions and supercritical fluids are preferred in wide spectrum of modern engineering applications ranging from the carbon-free power generation plant, pharmaceutical applications, nuclear power plant all the way to rocket launch vehicles. Unlike sub-critical or atmospheric pressure condition, the fluid at such elevated regions are characterized largely by diffusive turbulent mixing with no distinct liquid-gas interface. And, since most of the combustion phenomenon thereafter is governed by the process of turbulence, it is vital to understand the behaviour of jet disintegration and mixing, and to have an elaborate idea on the transfer of heat and momentum within the fluid flow. And since it is very unlikely to carry out detail experimental study at such harsh environment, the most promising tool would be the numerical study, however, the ad-hoc models used in modelling the behaviour of heat and momentum transfer typically considered valid under sub-critical regime are questionable in the critical – transcritical – supercritical conditions. A way to validate such modelling technique is through a precise and detail simulation of fluid flow at such conditions described by the governing equation, known as the Direct Numerical Simulation (DNS).

The present work is devoted to understanding, the mixing behaviour of temporally evolving planar trans-critical nitrogen jet with the help of previously generated DNS dataset, followed by validation of the ad-hoc models and modelling techniques used in less intensive and economic simulations such as RANS (Reynolds Averaged Navier-Stokes) simulation and LES (Large Eddy Simulation). In widely used RANS simulations, the solution is acquired for the mean flow field while averaging out the unsteadiness in time, since minute details might not be of extreme importance. However, the contribution of small and large eddies are modelled with the turbulence models, which are considered to be perfect in one situations and might not be the same in others. We would like to know if such turbulence models works well under flow with large thermodynamic non-linearities like that in trans-critical mixing. LES on the other hand resolves the anisotropic large eddies while modelling the isotropic small eddies called the sub-grid scale modelling,

thus LES is more computationally intensive and accurate compared to RANS and therefore, is gaining popularity these days.

This work demonstrates study of pressure dependencies on thermodynamics and flow variables involved in trans-critical jet largely governed by mixing. It also sheds lights on some considerably important aspects such as isotropic heat flux hypothesis, approximations such as beta-functions and no-model used in RANS framework, etc., which can help improve understanding of small scale contribution to the trans-critical fluid flow and dynamics of mixing under elevated temperature and pressure conditions.

CONTENTS

I OVERVIEW AND FUNDAMENTALS	
1 INTRODUCTION	4
1.1 Motivation: Supercritical Fluid	5
1.2 Stratified atmosphere of gas giants	7
1.3 Supercritical fluid and Liquid Rocket Engines	8
1.3.1 Need for high T_c and P_c	9
1.4 Supercritical Injection	11
1.5 Need for CFD	13
1.6 Overview of turbulence	15
1.6.1 Energy cascade	17
1.7 Overview of numerical modelling and simulation	18
1.7.1 RANS and Turbulence Modelling	22
1.7.2 LES and SGS modelling	26
1.7.3 Direct Numerical Simulation	30
1.8 Challenges in DNS	31
1.8.1 Spatial resolution	31
1.8.2 Temporal advancement	32
1.8.3 Boundary conditions	33
1.8.4 Classical assumptions to reduce computational costs in DNS	33
1.9 State-of-the-Art trans-supercritical mixing	34
1.10 State-of-the-Art DNS	38
1.11 Summary	43
2 THERMODYNAMICS AND MODELLING OF SUPERCRITICAL INJECTION	45
2.1 Thermo-physical properties of supercritical fluids	46
2.1.1 Pseudo-boiling line or Widom line	47
2.1.2 Pseudo-boiling	48
2.2 Subcritical versus supercritical injection	51
2.3 Real versus Ideal gas	52
2.4 Modelling Equation-Of-State (EOS) of real fluids	52
2.4.1 Ideal gas EoS and real gas effect	53
2.4.2 Real gas EOS	55
2.5 Summary	57
II NUMERICAL TREATMENT	
3 THEORETICAL FRAMEWORK FOR DNS	61
3.1 Introduction	62
3.2 Reference nitrogen EoS	63
3.2.1 Solid-liquid and vapour-liquid co-existence properties .	63
3.2.2 EoS for nitrogen	64

3.2.3	Ideal gas behaviour	65
3.3	Spectral method (SM)	66
3.3.1	SM versus FEM	66
3.4	Spectral element method (SEM)	67
3.5	Need for low-mach-number assumption	68
3.6	Boundary conditions	68
3.7	Governing equation	69
3.7.1	Filtered (LES) equation	71
3.8	DNS database	73
3.8.1	DNS computational domain	74
3.8.2	Initial conditions	74
3.8.3	Simulation regimes	76
3.9	Summary	80
 III RESULTS AND DISCUSSIONS		
4	RESULTS AND DISCUSSION	86
4.1	Study of laminar properties	87
4.2	Overview of the flow field	91
4.2.1	Density profiles	97
4.2.2	Isobaric specific heat profiles	98
4.2.3	Enthalpy profiles	99
4.2.4	Reynolds versus Favre averages	100
4.3	Variance study	102
4.3.1	Variance of isobaric specific heat	102
4.3.2	Variance of velocity component	104
4.3.3	Variance of scalars	108
4.4	Modelling	110
4.4.1	Probability density function (pdf) approach	111
4.4.2	Statistics and SGS Modelling	112
4.5	Reynolds stress and Turbulent heat flux	121
4.5.1	Reynolds stress	121
4.5.2	Turbulent heat flux	124
4.5.3	Turbulent Prandtl number	126
4.6	Anisotropy study	127
4.7	Summary	129
5	SUMMARY AND OUTLOOK	133
 IV BIBLIOGRAPHY		

LIST OF FIGURES

Figure 1	Illustration of a typical 2D phase diagram, marking the <i>triple point</i> (<i>TP</i>), where theoretically there different phases (namely solid, liquid and vapour) co-exists and <i>critical point</i> (<i>CP</i>), the end-point of a solid red line (above TP - which represents the phase equilibrium between liquid and vapour).	6
Figure 2	Visual snapshots showing the phase existence of ethane in three different states: 1) Sub-critical state (where liquid phase is distinct), 2) Critical point (Ethane: $T_{cr} = 32.17 \text{ }^{\circ}\text{C}$; $p_{cr} = 48.72 \text{ bar}$) and 3) Supercritical state (where liquid and gas phases are indistinguishable) [29, Horstmann S.,2000]	7
Figure 3	Injector plate assembly with injectors (a) [53, Lapenna P.,2016] & (b) [7, Banauti D., 2015].	12
Figure 4	Shadowgraphs of cryogenic nitrogen when injected into an ambient filled with gaseous helium [40, Mayer et al., 1998].	13
Figure 5	The energy cascade showing the transfer of energy in different sub-ranges. Concept from: [29, Horstmann S.,2000]	18
Figure 6	Illustration of velocity fluctuation in time when measured at a point in the flow field, is decomposed into mean and instantaneous fluctuations. Plus, the level of resolution RANS, LES and DNS can account for in the simulation.	21
Figure 7	Comparison between different filters used in sub-grid scale modelling [73, Stoll,R., 2014].	27
Figure 8	(a) DNS, (b) LES and (c) RANS prediction of a turbulent jet. [38, Maries, A.]	31
Figure 9	Shadowgraphs of LO_2 - LH_2 co-axial injection at three different pressures, showing the macroscopic behaviour of the oxygen jet taken in a backlight setup, where the six photographs show the time transient behaviour of the oxygen jet during startup transients. [39, Mayer, W. 1996]	35
Figure 10	Shadowgraph images of round liquid nitrogen injected into gaseous nitrogen at different chamber pressures (denoted by reduced chamber pressure: P_r , i.e. ratio of chamber pressure by critical pressure of injected nitrogen) [14, Chehroudi, 2012]	36

Figure 11	Schematic representation of cryogenic flames. (A) Subcritical oxygen, gaseous methane, (B) Transcritical oxygen, gaseous methane and (C) Transcritical oxygen, transcritical methane [71, Singla,G., et al., 2005].	37
Figure 12	DNS of N_2/CO_2 at $Re = 1000$ and LES of N_2/N_2 jet, carried out by , to study high pressure jet injection and mixing. [6, Bellan,J., et al., 2017]	39
Figure 13	Visualization of mass fraction of (a) C_7H_{16} and (b) O_2 in DNS of high pressure multispecies temporal mixing layer [6, Bellan,J. et al., 2017].	39
Figure 14	The DNS of chilled nitrogen injection in a round jet fashion into supercritical environment reported by [66, 67, Ries,F. et al.].	40
Figure 15	The evolution enthalpy of temporal jet at trans- and supercritical conditions, studied by [54, Lapenna, P.E., & Creta, F., 2017].	40
Figure 16	Sequence of unsteady jet evolution in time showing the density field and its unsteadiness and flow entrainments [76, Terashima,H. et al., 2011].	41
Figure 17	Illustration of unsteady flow structures appearing in supercritical planar jet [76, Terashima,H. et al., 2011].	41
Figure 18	Density and temperature contour of inert and reactive flow obtained with DNS [16, Chong,S.T., et al., 2017].	42
Figure 19	Instantaneous temperature (top-row) and density (bottom-row) distribution for cold flow (left-column) and combustion (right-column) [83, Wang,X., et al., 2018].	42
Figure 20	Thermodynamics illustration (a) & (b) [9, Banuti et al.& Hickey, 2017].	46
Figure 21	p-T state diagram (log scale) showing the Triple Point (TP), Critical Point (CP), widom line extending to supercritical regime along with transcritical injection which passes through critical and pseudo-boiling temperature.	48
Figure 22	Illustrative representation of isobaric specific heat capacity distribution over finite temperature range where $\Delta h_{structural}$ amount of enthalpy is used to overcome the intermolecular forces (like latent-heat spread over finite range of temperature) while $\Delta h_{thermal}$ is used to raise the temperature from T^- to T^+ by heating the fluid.	49
Figure 23	(a) The pressure dependants of isobaric specific heat for nitrogen. & (b) Position of maximum isobaric specific heat relative to coexistence line for nitrogen. [8, Banuti, D.T., 2015].	50

Figure 24	Specific enthalpy versus temperature profiles for three different pressures (one subcritical and two supercritical cases), for oxygen. Each curves are isobaric. The asymptotes are enthalpy for ideal gas and liquid [9, Banauti,D.T., 2017]	50
Figure 25	C_p evolution with temperature of Oxygen at subcritical (4 MPa) and supercritical (6 MPa) pressures along with the phase transition enthalpy Δh_{pb} at an interval of temperature ΔT . The enthalpy asymptotes are ideal gas h^{iG} and liquid reference state h^L [9, Banauti,D.T., 2017]	51
Figure 26	Density evolution of oxygen ($T_{cr} = 154.6$ K, $P_{cr} = 5.048$ MPa) with temperature at sub and supercritical pressure values. The real fluid approaches incompressible liquid at low temperatures while on the other hand, ideal gas at high temperatures. The solid-line are obtained with NIST database while the dashed-line follow the idea equation state [9, Raju,M. et al., 2017].	53
Figure 27	Pressure ratio ($p_r = p / p_{cr}$) versus Temperature ratio ($T_r = T / T_{cr}$) for Nitrogen, showing Z (with solid-line) and isochors (dashed-lines). The maroon line represent ideal gas ($z = 1$) and shaded region show ideal gas behaviour with 5% deviation [9, Raju,M. et al., 2017]. The red dot marks the critical point of nitrogen.	54
Figure 28	Thermodynamic parameters against temperature for Nitrogen at pressure 3.98 MPa (where $T_{cr} = 126.19$ and $p_{cr} = 3.3958$), computed with discussed EoS: PR (Peng-Robinson), PRC (Corrected Peng-Robinson), RK(Redlich-Kwong), SRK (Soave-Redlich-Kwong) and vdW (van der Walls).	56
Figure 29	Spectral element mapping from canonical 7th-order quadrilateral domain $\hat{\Omega}$ to physical sub-domain Ω_e [32, Kerkemeier, S. G., 2010].	67
Figure 30	Illustration of different injection processes: A) Sub-critical injection B) Trans-critical injection C) Near-critical injection D) Super-critical injection and E) High-pressure-ratio expansion. B) Trans-critical injection process is studied in the present work. The dashed-line represent the Widom line.	73
Figure 31	DNS configuration showing the computational domain of the temporal-planar transcritical jet. T_{jet} is the (cold) temperature of the injection jet while, T_{env} is the temperature of the (warm) supercritical nitrogen environment and U_{jet} is the initial mean shear. [55, 57, Lapenna,P.E. & Creta,F., 2019,2018]	74

Figure 32	Modified von Karman spectrum (wave number k versus kinetic energy E) used to trigger initial turbulence disturbance of velocity component [53, Lapenna,P.E., 2016].	76
Figure 33	The computational domain with dimensions where, $H = 2$ mm is the initial jet width, L_x , L_z and L_y are the length, width and height of the domain stretching in stream-wise, span-wise and cross-wise directions respectively.	77
Figure 34	Non-dimensionalized pressure-temperature plot with superimposed compressibility factor Z , showing four isobaric simulations carried out in the present work. The symbols \square , \circ and \diamond on each isobaric transcritcal injection line represent T^- , T_{pb} and T^+ temperatures while * shows critical-point. [55, Lapenna,P.E. & Creta,F., 2019]	77
Figure 35	(a) and (b) profiles are for N at $p_0/p_{cr} = 1.17$ which is close to R2P1 case (1.25) with $T^+ = 134.74$ K and $T^- = 127.73$ K. \circ represents the jet initial condition for the DNS reported by [55, 57, Lapenna,P.E. & Creta,F., 2019,2018].	79
Figure 36	Laminar thermodynamic properties against the temperature for different reduced pressure values ranging from near-to-critical-point to far-from-critical-point.	88
Figure 37	Molecular Prandtl number Pr against temperature at different reduced pressure values. The ' - ' vertical line represents the critical temperature of nitrogen at critical pressure i.e. reduced pressure $p_0/p_{cr} = 1$	89
Figure 38	Isobaric specific heat capacity C_p , density ρ , thermal conductivity λ or k and dynamic viscosity μ plotted against temperature at near-to-critical point and far-from-critical point.	90
Figure 39	Enthalpy H contour field of the flow, where $H = 0$ for cold transcritical injected jet at $T = 100$ K and $H = 1$ for warm supercritical N environment at $T = 300$ K.	91
Figure 40	Density ρ contour field of the flow along streadwise direction, where $\rho \approx 700$ for cold transcritical injected jet at $T = 100$ K and $\rho \approx 100$ for warm supercritical N environment at $T = 300$ K. The iso-line is mean density between inlet and ambient N.	92
Figure 41	Density ρ contour field of the flow along spanwise direction, where $\rho \sim 700$ for cold transcritical injected jet at $T = 100$ K and $\rho \approx 100$ for warm supercritical N environment at $T = 300$ K. The iso-line is mean density between inlet and ambient N.	93

Figure 42	The contours showing the Reynolds averaged fields with superimposed isolines of temperatures corresponding to T^+ (continuous line), T_{pb} (dashed line) and T^- (dashed dotted line) i.e. gas-like state, pseudo-boiling and liquid-like state respectively, as discussed previously in enthalpy budget (see 2.1.2 and Figure 22) [58, 55, Lapenna,P.E. et al., 2018-19].	95
Figure 43	Reynolds averaged Non-dimensional density profiles at 4 different pressure levels each at 4 different time instances. The averaging has been carried out along the stream-wise and span-wise direction.	97
Figure 44	Reynolds averaged isobaric specific heat $\overline{C_p}$ evolution along cross-wise direction, at four-different pressures each at four-different time instances.	98
Figure 45	2D contour plot of isobaric specific heat C_p at four different pressure levels (rows) each for four time instances (columns).	99
Figure 46	Reynolds averaged enthalpy \overline{H} evolution along the cross-wise direction. $\overline{H} = 1$ corresponds to the warm environment ($T = 300$ K), while $\overline{H} = 0$ corresponds to the cold jet ($T = 100$ K).	100
Figure 47	Reynolds (solid —) and Favre (dashed ——) averaging compared with the isobaric density profiles.	101
Figure 48	The variance of isobaric specific heat capacity $\overline{C'_p C'_p} / \Delta C_p^2$, denoted by \circ and its average $\overline{C'_p}$, denoted by \square along the cross-wise direction, at four different reduced pressures and corresponding four time instances.	103
Figure 49	Velocity variance field computed <i>on-the-flow</i> at each simulation time reported by [55, Lapenna,P.E. & Creta,F., 2019]. The superimposed isolines represents temperatures corresponding to T^+ (continuous line), T_{pb} (dashed line) and T^- (dashed dotted line) i.e. gas-like state, pseudo-boiling and liquid-like state respectively, as discussed previously in enthalpy budget (see 2.1.2 and Figure 22).	104
Figure 50	Normalized variance of stream-wise velocity component $\overline{u'u'} / \Delta u^2$ marked by (\circ) and normalized \overline{u} marked by (\square) , against cross-wise direction, at four different reduced pressure levels.	105
Figure 51	Normalized variance of cross-wise velocity component $\overline{v'v'} / \Delta u^2$ marked by (\circ) and normalized \overline{v} marked by (\square) , against cross-wise direction, at four different reduced pressure levels.	106

Figure 52	Normalized variance of span-wise velocity component $w'w'/\Delta u^2$ marked by (○) and normalized \bar{w} marked by (□), against cross-wise direction, at four different reduced pressure levels.	107
Figure 53	The peaks of the normalized variance of span-wise, cross-wise and stream-wise velocity components at four different reduced pressure levels.	108
Figure 54	Density and enthalpy variance field computed <i>on-the-flow</i> at each simulation time reported by [55, Lapenna,P.E. & Creta,F., 2019].	108
Figure 55	Normalized variance of density $\rho'\rho'/\Delta\rho^2$ marked by (○) and normalized $\bar{\rho}$ marked by (□), against cross-wise direction, at four different reduced pressure levels.	109
Figure 56	Variance of non-dimensional enthalpy $\overline{\xi'\xi'}$ marked by (○) and average enthalpy $\bar{\xi}$ marked by (□), against cross-wise direction, at four different reduced pressure levels.	110
Figure 57	The peaks of the normalized variance of ρ , ξ and C_p at four different reduced pressure levels.	111
Figure 58	Probability density function forms for a conserved scalar in various types of flow [17, Law,C.K., 2012].	112
Figure 59	The behaviour of β -pdf function (as a function of a variable ξ) for different values of α and β [37, Malasekara,H.K., <i>et al.</i> , 2012].	113
Figure 60	Non-dimensional enthalpy ξ pdf at 4-different reduced pressure levels and respective 4-time instances, with additional subplot in semi-logarithmic scale, computed at $y/H_{jet} = 0$	114
Figure 61	Non-dimensional density ρ^* pdf at 4-different reduced pressure levels and respective 4-time instances, with additional subplot in semi-logarithmic scale, computed at $y/H_{jet} = 0$	115
Figure 62	Non-dimensional isobaric specific heat capacity C_p^* pdf at 4-different reduced pressure levels and respective 4-time instances, with additional subplot in semi-logarithmic scale, computed at $y/H_{jet} = 0$	116
Figure 63	Prandtl number Pr^* pdf at 4-different reduced pressure levels and respective 4-time instances, with additional subplot in semi-logarithmic scale, computed at $y/H_{jet} = 0$	117
Figure 64	The non-dimensional enthalpy ξ , density ρ^* , isobaric heat capacity C_p^* and Prandtl number Pr^* pdf at 4-different reduced pressure levels, with additional subplot in semi-logarithmic scale, computed at $y/H_{jet} = 16$	118

Figure 65	Non-dimensional density ρ^* pdf at 4-different reduced pressure levels and respective 4-time instances, with additional subplot in semi-logarithmic scale, computed at $y/H_{jet} = pb$	119
Figure 66	The average thermodynamic properties C_p (left column) and ρ (right column) computed along the cross-wise direction $Y-axis$ at $t/t_{jet} = 12$, for various reduced pressure levels, with three different approaches (see Table ??).	122
Figure 67	The average thermodynamic properties C_p (left column) and ρ (right column) computed along the cross-wise direction $Y-axis$ at $t/t_{jet} = 16$, for various reduced pressure levels, with three different approaches (see Table ??).	123
Figure 68	The Reynolds stress normalized by squared mean shear computed for at all reduced pressure level for all time instances $t/t_{jet} = t^*$	124
Figure 69	The turbulent heat flux normalized by the product of enthalpy and mean shear computed for at all reduced pressure level for all time instances $t/t_{jet} = t^*$	125
Figure 70	Turbulent heat flux at the last time instant $t/t_{jet} = 16$, for all 4-reduced pressure levels.	126
Figure 71	Turbulent Prandtl number Pr_t at the last time instant $t/t_{jet} = 16$, for all 4-reduced pressure levels.	127
Figure 72	Comparison of anisotropy with that by Ries et al. [66, Ries,F. et al., 2017].	128
Figure 73	Joint pdf of anisotropy at 4-reduced pressure levels and last time instant $t/t_{jet} = 16$	128
Figure 74	Joint pdf of the anisotropy computed at all 4-reduced pressure levels and their 4-respective time instances. .	129

LIST OF TABLES

Table 5	Comparison of I_{sp} and p_c of few prominent LREs [11, Bianchi D.]. Noble propellants in these cases are liquid Oxygen (LOX); as an oxidiser, Liquid Hydrogen (LH ₂); as a fuel and Refined Petroleum (highly refined form of kerosene: RP1).	11
Table 6	Critical properties of some substances [7, 53, Banauti D., Lapenna P.].	11
Table 7	Closure models to evaluate the turbulent viscosity (μ_t).	25
Table 8	Well known standard turbulence models used in popular commercial CFD codes [37, Malasekera W. & Versteeg H. K.].	25
Table 9	Some important SGS closure models used in LES.	29
Table 11	Thermo-physical difference between fluid under supercritical and subcritical conditions.	52
Table 12	The critical values of nitrogen reported by [47, Nowak,P. <i>et al.</i> , 1997] and adopted for EoS by[81, Wagner, W., Span, R., <i>et al.</i> , 2001].	64
Table 13	The triple-point values of nitrogen reported by [47, Nowak,P. <i>et al.</i> , 1997] and adopted for EoS by [81, Wagner, W., Span, R., <i>et al.</i> , 2001].	64
Table 14	Primary computational parameters of transcritical temporal jets at four different pressure levels. $H = 2$ mm is the jet width [55, Lapenna,P.E. & Creta,F., 2019].	78
Table 15	The simulation cases, each reduced pressures consists four time instances.	94
Table 16	Three approaches used to obtain the mean or filtered values along cross wise direction in the present work.	120

Part I

OVERVIEW AND FUNDAMENTALS

1 Introduction

Outline

This chapter gives insight to high pressure injection process typically seen in the injection of propellants into the combustion chamber of Liquid Rocket Engines and several other engineering applications. The behaviour of the fluid at such elevated pressure and temperature, called supercritical fluids, begin different from its subcritical counterpart is also discussed in this chapter.

- Section 1.1 begins with the preliminary definition of fluid and its various forms, both from natural and engineering point of view. *What is fluid ? What distinguishes air from water, and water from supercritical fluid ? Why are supercritical fluid so important ?*
- Section 1.2 gives a glimpse on the existence of supercritical fluid in nature like the gas-giants like Jupiter due to its high pressure and temperature. *Does supercritical fluid exist in nature, if so where, may be gas-giants like Jupiter ? How do they exist and why is it of our interest ?*
- Section 1.3 discusses the importance, and challenges of high pressure combustion, from aerospace engineering point of view, which leads the fluid to be in its supercritical state in the very first place. *Why high pressure combustion in the first place ? What are the challenges ?*
- Section 1.4 reviews the concept of supercritical injection in LRE. *How does injection and mixing occur in LRE ? Is mixing that important, Why ?*
- Section 1.5 gives idea on the importance and advantages of numerical modelling which should go in parallel with the classical experimental approach. *What is CFD ? What advantage and challenges do we have with CFD ?*
- Section 1.6 gives a glimpse of the chaotic behaviour of fluid and basic mathematical approach to understand such process. *What is turbulence, how does it exit and propagate and what are its signatures ? What does it do to the fluid flow ? Is it advantageous for the combustion ? What are basic mathematical tools used to understand turbulence ?*

- Section 1.7 gives an overview of the major numerical simulation approaches in particular LES, RANS, and DNS, with their pros and cons. *What are the governing equations, to be solved in the numerical simulation ? Is it viable to solve the equation in its minute details, if not how to resolve it ? How the averaged field give raise to unclosed terms and how are they closed ? What are most popular closure models ?*
- Sections 1.8 and 1.10 aims to give better insight to DNS approach. *Why DNS and what are its state-of-the art in supercritical injection ?*
- Section 1.9 recalls the experiments and state-of-the-art numerical techniques employed to understand the trans- super- critical injection and mixing process. *What were the pioneering studies on trans-supercritical injection ? How they changed the idea mindset from classical atomization and mixing process under sub-critical conditions ?*

1.1 MOTIVATION: SUPERCRITICAL FLUID

Fluids, like air that we feel around, breath in-and-out, and make air/space travel possible; beverages that we drink to hydrate our body; the blood that transport necessary ingredients to different part of our body for its full functionality, and so on, is one of the key aspect of our everyday life. Nonetheless, our understanding of such 'fluid', so vital for your existence, to its full extent is still a challenge. Moreover, with improvement of science and technology, and understanding physics of fluids, we can exploit even more and optimize our technologies. Fluid exists in various forms and phases with different temperatures and pressures, they behave differently under different circumstances and we give names to them accordingly, but share some commonalities: ability to flow (fluids take shape of a container it's kept in) and ability of non-resistance to permanent deformation. Therefore, we can define fluid as, phase of matter including liquid, gases and plasma, that can continually deform when subjected to external force (shear stress) [33, A.D.Kraus et al.].

Temperature and pressure are among those thermodynamic properties that substantially influence fluid behaviour. For an instance, the presence of water in liquid state on Earth's surface is due to the fact that the amount of gravity is perfect enough to hold sufficient layers of atmosphere within its gravitational vicinity, which in turn induce perfect amount of atmospheric pressure and temperature on the Earth's surface such that water is available

in liquid and not in gaseous or solid (ice) state. The life form as we live today might not exist all or would have been in completely different form, otherwise, like our neighbour planet Mars, which for some reasons, has slightly less strong gravitational field ($g = 3.711m/s^2$) than Earth ($g = 9.807m/s^2$), has thinner atmosphere, and thus lesser atmospheric pressure on Martian surface (which is less than 1% that of Earth's), not enough for water to exist in its liquid form [23, A. Diez2018]. However, radar data reported by [46, Orosei et al.] from Mars Express mission, shows the presence of liquid water close to South Pole beneath 1.5 km of icy surface.

As we all are very familiar with a process of ice (solid) when heated under constant pressure (isobaric) condition, undergo phase transition to water (liquid) and further to vapour (gas). The transition from liquid to gaseous state is well defined with latent heat of vaporization concept, which is defined as, "the heat required to change one mole of liquid at its boiling point under standard atmospheric pressure" [20, Datt P. et al. 2011]. The phase change is a constant temperature (isothermal) process, where the molecules arrange themselves to new state. If the new phase has higher amount of thermal energy, substance absorbs the necessary thermal energy from the environment (called heat of vaporization) and vice versa. This concept works very well until a certain temperature and corresponding certain pressure called *critical temperature* (T_{cr}) and *critical pressure* (p_{cr}). And therefore the point representing T_{cr} and p_{cr} in T-p coordinate (phase diagram) is called a *critical point*. The supercritical region exceeds both T_{cr}

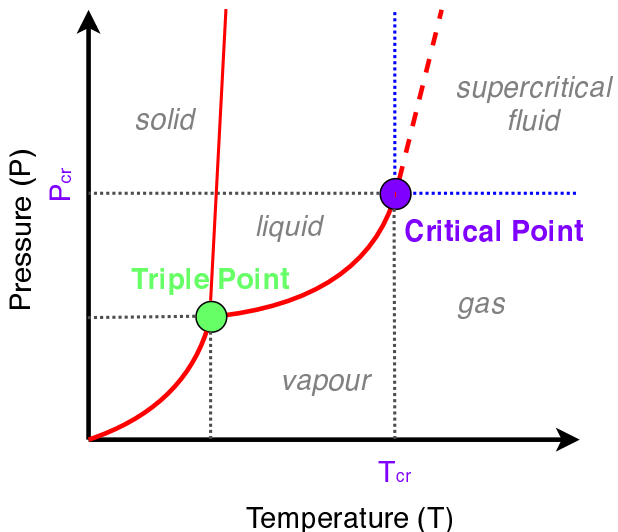


Figure 1: Illustration of a typical 2D phase diagram, marking the *triple point* (TP), where theoretically three different phases (namely solid, liquid and vapour) co-exists and *critical point* (CP), the end-point of a solid red line (above TP - which represents the phase equilibrium between liquid and vapour).

and P_{cr} , there exists no sharp transition and hence no distinctive distinction between the liquid phase to gas phase. Instead, in the process of isobaric heat

addition leads from liquid like to gaseous like transition. In detail description of thermodynamic properties can be found on later chapters. However, some very important properties of supercritical fluids are worth mentioning here, which are the following:

- The gas-liquid interface vanishes and appears fuzzy, as surface tension that held the small structures together (for e.g. force glueing H_2O molecules together to form water droplet) no longer exists [7, Banauti D.,2015].
- At near critical pressure, the fluid properties become very sensitive to change in temperature. Most vividly, the thermodynamic properties like the density diminishes very sharply and is accompanied by sharp rise in the isobaric specific heat (C_p). Plus, the thermal diffusivity reaches distinct minimum value [52, Oschwald, Chehraudi et al., 2006].

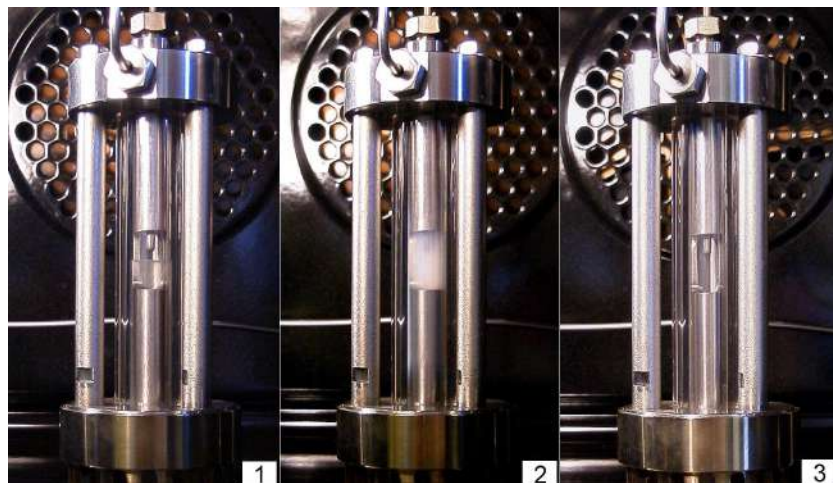


Figure 2: Visual snapshots showing the phase existence of ethane in three different states: 1) Sub-critical state (where liquid phase is distinct), 2) Critical point (Ethane: $T_{cr} = 32.17 \text{ }^{\circ}\text{C}$; $p_{cr} = 48.72 \text{ bar}$) and 3) Supercritical state (where liquid and gas phases are indistinguishable) [29, Horstmann S.,2000]

The thermodynamic conditions where the fluid is in trans- and supercritical conditions are very likely and in some applications are even favoured like in rocket propulsions system, gas turbine engines, diesel engines, supercritical steam generators in power plants, refrigerating systems with supercritical CO_2 , theoretical mineral extraction in future planet exploration missions (like Mars due to high solubility of supercritical fluids), supercritical drying and cleaning etc., the reason always begin higher efficiency in the process [66, Ries F. et al.,2017].

1.2 STRATIFIED ATMOSPHERE OF GAS GIANTS

Gas giants like Jupiter, Uranus and Neptune are mostly composed of hydrogen and helium [22, D'Angelo G.,2018]. The gravitational pull is so strong

that the gaseous layer is compressed upto high temperature and pressure well beyond the critical point of hydrogen ($T_{cr} = 33K$ and $p_{cr} = 1.3MPa$). Therefore, in gas giants such as Jupiter, Saturn, exoplanets and brown dwarfs, molecular hydrogen is in supercritical state. In Jupiter and Saturn, supercritical molecular hydrogen undergoes dynamic transition around 10 GPa and 3000 K from liquid state to gas-like fluid state [79, Trachenko K. et al., 2014]. Trachenko et al. mentions that in such gas giants, it has been considered to be the case up to high as 100-200 GPa pressures where hydrogen fluid dissociates and metallizes. Unlike rocky planets like Earth, Mars, Venus, etc. the boundary between atmosphere and exterior (atmosphere) of such gas giant planets are not separate and distinguishable due to the fact that the supercritical fluids like that in gas giants are considered to be homogeneous and smooth (also seen in Figure 2). Thus, understanding transitional boundary between liquid-like and gas-like phase will let us understand the planet's interior even better.

1.3 SUPERCRITICAL FLUID AND LIQUID ROCKET ENGINES

Revising some basic rocket performance equations, give some important reasons for the analysis of supercritical fluid (in other words, the fluid in supercritical condition, thermodynamically) in rocket propulsion. The term *fluid* until now, shall be addressed by the name *propellant* (oxidizer and fuel), as we would like to understand its importance in rocket engine. The overall performance of rocket engine is usually expressed in a number called *Specific Impulse* (I_{sp}) which gives a measure of weight flow rate (\dot{W}) of the propellant to generate a certain level of thrust (F). There are several ways of expressing I_{sp} to analyse dependences of various aspects to overall performance of the vehicle.

$$I_{sp} = \frac{F}{\dot{W}} = \frac{F}{g_0 \dot{m}} = \frac{c}{g_0} \quad (1)$$

- where,
- g_0 acceleration due to gravity $\approx 9.801 m/s^2$
 - \dot{m} mass flow rate of the propellant [kg/m^3]
 - c effective exhaust velocity [m/s]
 - A_e Exit area of the nozzle [m^2]

$$c = v_e + (p_e - p_a) \frac{A_e}{\dot{m}} \quad (2)$$

If we look at equation 1 and 2, in case of adapted condition (i.e. when the ambient pressure (p_a) is balanced by the exit pressure of the exhaust gas (p_e)), $c = v_e$ and thus,

$$I_{sp} = v_e / g_0 \quad (3)$$

Equation 3, now gives an idea that the overall rocket performance is mostly hinged or largely dependent on the exhaust gas velocity which can be thought of a direct outcome of the combustion process and acceleration of the combus-

tion products (the exhaust gas) out of the CD (Convergent-Divergent) rocket nozzle. In fact such dependencies can be clearly seen in the relations below:

$$c = c^* C_F \quad (4)$$

$$I_{sp} = \frac{c^* C_F}{g_0} \quad (5)$$

$$v_e = \sqrt{\frac{2\gamma}{\gamma-1} \mathbb{R} \left[1 - \left(\frac{p_e}{p_c} \right)^{\frac{\gamma-1}{\gamma}} \right] \frac{T_c}{M_W}} \quad (6)$$

$$c^* = \frac{p_c A_t}{\dot{m}} = \frac{1}{\Gamma} \sqrt{\mathbb{R} \frac{T_c}{M_W}} \quad (7)$$

$$C_F = \Gamma \sqrt{\frac{2\gamma}{\gamma-1} \left[1 - \left(\frac{p_e}{p_c} \right)^{\frac{\gamma-1}{\gamma}} \right]} + \left(\frac{p_e}{p_c} - \frac{p_a}{p_c} \right) \frac{A_e}{A_t} \quad (8)$$

c^*	characteristic velocity
C_F	thrust coefficient
v_e	exit velocity of gas out of nozzle
$p_c = p_0$	combustion chamber pressure
where, $T_c = T_0$	combustion chamber temperature
γ	specific heat ratio ($\frac{C_p}{C_v}$)
\mathbb{R}	universal gas constant
A_t	throat area
M_W	molecular weight of gas
Γ	$\frac{2\gamma}{\gamma-1}$

The parameter characteristic velocity (c^*) gives the notion of rate of propellant combustion performance while the thrust coefficient (C_F) is used to measure the gas expansion performance through the nozzle. Their combined effect can be seen in the overall rocket performance (Equation 5). Working on c^* influences v_e and therefore I_{sp} .

1.3.1 Need for high T_c and P_c

Its quiet straight forward from Equation 6 and 7 that, the increment of chamber temperature, leads to higher value of characteristic velocity and thus higher value of specific impulse. Similar analysis can be done from the prospective of combustion pressure, for simplicity and to have clear picture, consider an ideal case of complete expansion process (where $T_{exit} = 0K$ and $p_e = p_a$), such condition ideally yields the maximum possible exit velocity and I_{sp} . The Equation 6 and 3 is simplified as:

$$v_e|_{max} = \sqrt{\frac{2\gamma \mathbb{R} T_c}{\gamma-1}} = \sqrt{\frac{2\gamma}{\gamma-1} \frac{p_c}{\rho_c}} \quad (9)$$

And the corresponding specific impulse is given as;

$$I_{sp}|_{max} = \frac{1}{g_0} \sqrt{\frac{2\gamma}{\gamma - 1} \frac{p_c}{\rho_c}} \quad (10)$$

The higher value of chamber pressure have higher value of I_{sp} . The better performing rocket engines require high values of pressure and temperature, plus lighter combustion products. For this reason, the lighter propellants (like hydrogen and oxygen) and engines (Liquid Rocket Engines (LRE)) operating at higher values of chamber conditions have better performance. The typical I_{sp} values of LRE ranges between 250 s to 450 s while that of Solid Rocket Motor (SRM) ranges between 200 s to 300 s.

The important factor for the need of such high chamber pressure is the reduction of engine size. For a given thrust value (F), the throat area (A_t) proportionality can be expressed as;

$$A_t = \frac{F}{p_c C_F} \propto D_t^2 \quad (11)$$

The increase in chamber pressure can have an advantage of reduction in engine dimension. Therefore, the advantages associated to high value of operating chamber pressure are enhancement of engine performance and reduction in engine dimension. However, there exists some serious consequences and are listed below:

- The heat transfer increases almost linearly with chamber pressure. The heat flux (q) proportionality with p_c is

$$q \propto \frac{p_c^{0.9}}{F^{0.1}} \quad (12)$$

The inverse proportionality is worth mentioning; the larger engine with higher thrust level considerably encounter less heat flux. However, the dependencies in this case is not that strong as in case of p_c

- Thicker chamber walls supported by considerably heavier piping systems, valves, and pumps to withstand high p_c increases the engine mass.
- To maintain high pressure in the chamber the turbo-pumps should be powerful enough and thus the gas flow from the gas generator to drive turbines increases with p_c . This makes the pump and housing heavier contributing to overall engine mass.

Therefore, the optimum value of the chamber pressure is usually compromised between performance, engine mass and possible development problems. In any case, the value of the operating chamber pressure and temperature in LRE is well beyond the critical values. Therefore, It is important to understand how the propellant injected into such supercritical atmosphere

behave and more importantly how they mix before combustion occurs.

Some of the characteristic parameters of few representative LREs (see Table: 5) when compared against the critical pressure and temperature values of some fluids (and/or noble propellants for LRE) (see Table:6), gives more idea on the issue of supercritical injection. With an idea of the typical chamber

Rocket Engine	Lunch Vehicle	Propellant Combination	$I_{sp} _{vac}$ [s]	p_c [MPa]
RS-25 (USA)	Space Shuttle	LOX-LH2	453	22.6
Vulcain-2 (Europe)	Arian-5,6	LOX-LH2	429	11.7
Vulcain (Europe)	Arian-6	LOX-LH2	431	10.2
RD-180 (Russia)	Atlas-V	LOX-RP1	338	26.7
NK-33(Russia)	Soyuz-2-1V	LOX-RP1	331	14.5
F-1 (USA)	Saturn-V	LOX-RP1	304	7.0
Merlin-1D (USA)	Falcon-9 & Falcon Heavy	LOX-RP1	311	9.7

Table 5: Comparison of I_{sp} and p_c of few prominent LREs [11, Bianchi D.]. Noble propellants in these cases are liquid Oxygen (LOX); as an oxidiser, Liquid Hydrogen (LH2); as a fuel and Refined Petroleum (highly refined form of kerosene: RP1).

pressure values (see Table 5) of some notable liquid rocket engines, one can also compare the critical pressure and temperature of some substances as listed below:

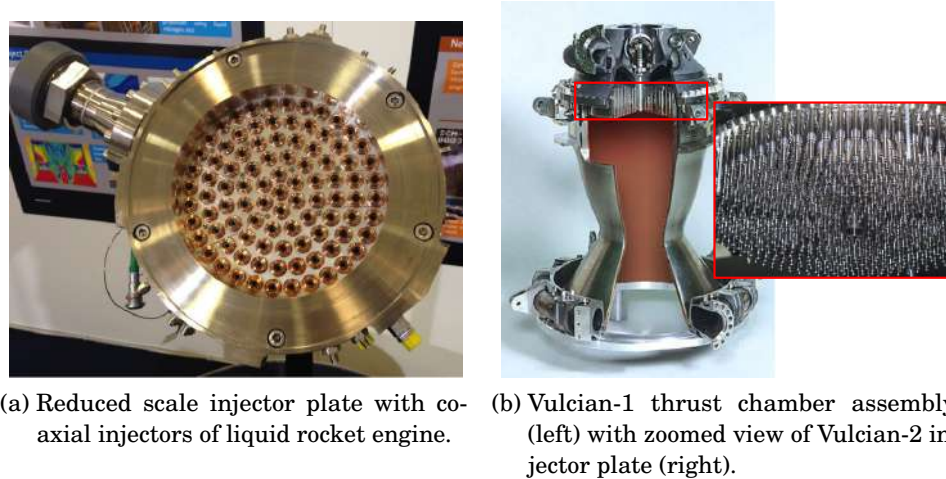
Name	Formula	T_{cr} [K]	p_{cr} [MPa]	ρ_{cr} [kg/m^3]
Hydrogen	H_2	33.15	1.315	30.12
Helium	He	5.210	5.040	41.45
Nitrogen	N_2	126.19	3.396	313.28
Oxygen	O_2	154.0	5.043	436.11
Methane	CH_4	190.56	4.592	162.65
Water	H_2O	647.10	22.064	312.96
Ethane	C_2H_6	154.6	4.872	203.00
Propane	C_3H_8	307.32	4.251	217.00

Table 6: Critical properties of some substances [7, 53, Banauti D., Lapenna P.].

1.4 SUPERCRITICAL INJECTION

As the name suggests, the propellant in the Liquid Rocket Engines are in liquid state for some of its advantageous nature like smaller storage tanks

(as compared to when stored in gaseous state), controllability in flow rate and cooling properties. Further, such liquid propellants could be monopropellants, bipropellants, cryogenic propellants or storable liquid propellants (more details can be found on classic rocket propulsion textbook *Basic Propulsion Elements* [74, Sutton & Oscar, 2001] and *Liquid propellant rocket engine*[30, Huang & Huzel, 1971]). Mostly commonly used (cryogenic) propellants like oxygen and hydrogen are stored in a chilled ambient tanks and are pumped to the combustion chamber (mostly hydrogen is pumped through rocket nozzle cooling channel, called regenerative cooling). As discussed earlier, the combustion chamber is in supercritical condition and thus the injection of propellant into such heated and pressurized environment should ideally undergo effective and efficient mixing, global mixture ratio, local mixture ratio (like that near the wall to achieve film cooling effect), and homogeneous heat distribution along each cross section of the chamber (i.e. minimal stratification) [7, Banauti D., 2015].



(a) Reduced scale injector plate with coaxial injectors of liquid rocket engine. (b) Vulcian-1 thrust chamber assembly (left) with zoomed view of Vulcian-2 injector plate (right).

Figure 3: Injector plate assembly with injectors (a) [53, Lapenna P., 2016] & (b) [7, Banauti D., 2015].

Injector design has a very important role in combustion efficiency as it determines how the liquid fluid is spread, atomize and therefore, how fuel and oxidizer mix together, which finally have an impact on combustion effectiveness. Different configurations of the injectors have been designed so far which employ various technique to impinge the propellant such that proper distribution and mixing of fuel and oxidizer can be achieved. Some of the well known designs are swirl injectors, shower head, coaxial hollow post injectors and triplet impinging jets. The most common one being coaxial hollow post injector because of its geometrical simplicity and mixing efficiency due to large shear between oxidizer and fuel streams [53, Lapenna P. 2016]. The production (or suppression) of harmful combustion products can also be related to such injection process, this is one of the reason for large extent of researches in the field of combustion (typically in gasoline engines, gas

turbine engines) are still under-way. In fact, from the view point of effectiveness of combustion process (like in cylinders of internal combustion engines), turbulence enhances the mixing process of fuel and oxidizer and produces cleaner products.

The process of mixing and energy conversion in rocket chamber is completely governed by turbulence, understanding such complexity is already a huge challenge, however, the better understanding of such complex problem help engineers to design time and cost-saving modelling tools, thus help build more efficient rocket engine with higher performance. And, so is the motive of this thesis work; to understand the mixing process in such elevated pressure with highly promising numerical modelling tool.

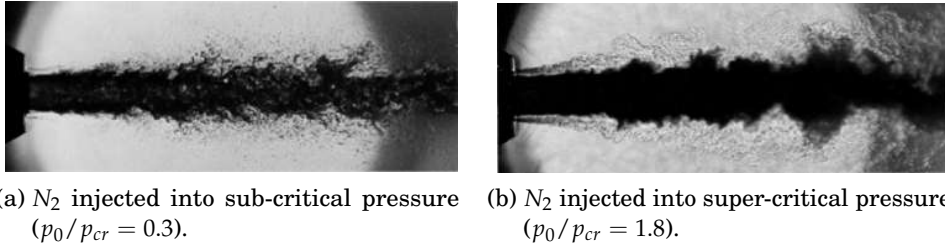


Figure 4: Shadowgraphs of cryogenic nitrogen when injected into an ambient filled with gaseous helium [40, Mayer et al., 1998].

In Figure 4, it is very interesting to see and compare the clear difference between the injection of liquid nitrogen into supercritical environment filled with gaseous helium, imitating the combustion chamber ambient. This is one of the pioneering experimental results in the literature showing some very crucial distinction in high pressure injection process, conducted by Mayer et al. [40, Mayer et al., 1998]. The sub-critical injection ($p_0 < p_{cr}$) shows distinctive jet break up as droplet move in the gaseous stream and finally vaporizes, mixes and react with the surrounding in the case of reactive flow. The jet break up is followed by atomization. While on the other hand, super-critical injection process ($p_0 > p_{cr}$) has no such distinctive droplets and neither ligaments disengaging from the jet-core. The liquid-gaseous interface is not clear and looks diffused, the interface dissolves. In fact, the process is described to resemble turbulent mixing rather than liquid jet-break up [7, Banauti D., 2015].

1.5 NEED FOR CFD

Until late 1950s, experimental techniques or rigorous analytical computation, were the only means to obtain the quantitative parameters (like the values of pressure, temperature, density etc.) in the fluid flow regime. With the advancement of computer technology and its improvement in processing and storage capabilities, computers now can compute a set of governing

equations for fluid dynamics called the *Navier-Stokes equations* to some appreciable level, better enough to understand the fluid flow properties to some extent. Such popular tool which allows to numerically solve a set of partial differential equations on a discrete points evolving in space as well as time, depending on the problem is known with a name *Computational Fluid Dynamics*.

In the study of flow properties and mixing process, at highly elevated temperature and pressure like in combustion chamber of LRE, it's not possible to insert a probe inside the chamber to obtain the thermodynamic and fluid parameters. Therefore, it was impossible to study the turbulence of supercritical fluid to upto full extent until recently, even though the concept has been around in scientific community for a while. The technique of studying the fluid behaviour with CFD reduces time and money consuming efforts drastically, and it's able to simulate more realistic conditions, the experimental results can be contaminated with the noise and disturbances inherited by the measuring devices or set-up abnormalities.

As highly promising and scientific tool CFD seems to be, it's equally challenging and complicated with lot of unsolved concepts yet to be fully understood. The solution to the problem is not always guaranteed with all initial and boundary conditions [43, Moin P. & Kim J., 1997]. The difficulty with the computation is the fact that the Navier-Stokes equations are non-linear, whose interactions generates wide range of scales creating difficulty in solving them, (Moin P. mentions that) in turbulence the range of size of whirling eddies can vary 1000-fold or even more. The other problem is dependencies of fluid parameters both in time and space, therefore simultaneous computation of such parameter at different points consume lot of computational resources and thus, enhances the complexity of the problem. Further to add as a nightmare to engineers, the combustion process requires additional computation of energy, and species conservation to the problem, which has its own non-linearities.

Turbulence enhanced combustion is well known for it – *multi-scale and multi-physics* problem. Turbulence is associated with wide range of time and length scales (i.e. in time and space). Turbulence has bigger and smaller vortices (or eddies) which continuously undergo chaotic formation and break-down. Large eddies break-down to smaller ones which further into smaller and so on. The smallest eddies dissipate viscosity into heat. There exists a cascade of energy flow from large vortices to the smallest ones. The largest motion in the flow field (large vortices; large scales) is associated with most of the kinetic energy which is then cascaded to the smallest vortices (small scales), which dissipate viscously into heat [43, Moin P. & Kim J., 1997]. Therefore, to fully understand the nature of turbulence, one need to solve NS equation to its finest level i.e. upto to the range of small scale (both in time and space). This demands smallest grid points in the computational

domain, enough to fit the smallest vortices and capture its dissipation. One can imagine the computational power required to carry out calculation at each of such points to fully understand the nature of turbulence, it can only be possible with parallel computing technology within reasonable 'wall clock' time. Such a way of computation is called *DNS (Direct Numerical Simulation)*, where all scales of motions are resolved. In fact, the number of girds to be resolved is proportional to $Re^{9/4}$ and the computational time to Re^3 . The DNS simulation is carried out to understand turbulent mixing of inert fluid (nitrogen) when injected into supercritical environment, in this thesis.

1.6 OVERVIEW OF TURBULENCE

Quantitatively small glimpse towards understanding turbulence was attempted in section 1.5. In continuation to previous explanation, the turbulent flow associated to the higher Reynolds number is chaotic and random in nature, in which the variations in velocity and pressure in time is evident. These fluctuations in velocity vector and scalars quantities like pressure, temperature, give raise to additional stresses on the fluid flow known as *Reynolds Stresses* (to be discussed in detail later).

In a pioneering study on turbulent by Irish-born British scholar Osborne Reynolds, the transition from the laminar to turbulent flow was for higher value to Reynolds number (Re, a dimensionless number, a ratio between inertial forces to viscous forces). The flow with higher value of Re is dominated by inertial forces over viscous forces and vice versa, and therefore the turbulence characterized by such elevated Reynolds number is effectively invisid [37, Malasekera W. & Versteeg H. K.]. In order to better understand the complexity with numerical modelling of turbulent flow (which are the flow of dominance in the real world), the turbulent time dependent velocity ($u(t)$) can be splitted into the steady mean value (\bar{u}) and fluctuating component ($u'(t)$), called *Reynolds decomposition*.

$$u(t) = \bar{u} + u'(t) \quad (13)$$

This decomposition is useful in the sense that the instantaneous quantities like velocity, pressure, temperature etc., can be decomposed to an average value and its instantaneous fluctuations, tricks are developed to solve only the mean quantities and model the effects due to fluctuations to reduce the computational costs. It has been discussed by Malasekera and Versteeg that even in flows where \bar{u} and \bar{p} varies in only 1D or 2D in space, the turbulence fluctuations always have 3D spatial character which are rotational flow structures called the *turbulent eddies*, which exists in a wide range of length and time scales. These eddies are responsible for mixing in turbulent flow. The fluid particles in far field are brought close together by such eddies causing effective exchange of mass, momentum and heat, and therefore, effective mixing takes place. Such effective mixing process give rise to high

value of diffusion coefficient for mass, momentum and heat [37, Malasekera W. & Versteeg H. K.]. The process of energy extraction by the large turbulent eddies from the mean flow field is described by a process called *vortex stretching*. So extracted energy is cascaded to the smallest eddies which finally dissipates into thermal energy through molecular viscosity by the action of viscous stresses, resulting to energy loss in turbulent flow. The cause of the this energy cascade arises from the inertial forces in the fluid, the driving mechanism of such energy cascade process is still not clear and is an important area of investigation , however, some purpose vortex stretching to be a candidate [13, Carbone M. & Bragg A.D., 2019].

In any case, an angular momentum is conserved in the process of vortex stretching causing the rotational rate to increase and radius of cross section to decrease thus, this process initiates the motion at smaller transverse length and time scales (detail can be found on *An Introduction to Computational Fluid Dynamics: The Finite Volume Method*, [37, Malasekera W. & Versteeg H. K.]). Larger eddies, which extract energy through strong interaction with mean flow, are associated to high energy content while the smallest eddies are associated with the least energy content.

The first statistical moment (mean) is used to describe the instantaneous flow variable (refer Eq. 13) similarly, other statistical analysis of the flow variables provide better understanding of the turbulence modelling, some important ones are attempted to introduce in this section.

Time Average: The mean ($\bar{\phi}$) of a flow property (ϕ) can be defined as:

$$\bar{\phi} = \frac{1}{\Delta t} \int_0^{\Delta t} \phi(t) dt \quad (14)$$

And that of the fluctuation is given as

$$\bar{\phi}' = \frac{1}{\Delta t} \int_0^{\Delta t} \phi'(t) dt \equiv 0 \quad (15)$$

Variance and Root Mean Square: These details are necessary to get information on the behaviour of fluctuations (ϕ') about the mean value ($\bar{\phi}$).

$$\overline{(\phi')^2} = \frac{1}{\Delta t} \int_0^{\Delta t} (\phi'(t))^2 dt \quad (16)$$

$$\phi_{RMS} = \sqrt{\overline{(\phi')^2}} = \sqrt{\frac{1}{\Delta t} \int_0^{\Delta t} (\phi'(t))^2 dt} \quad (17)$$

The root-mean-square of the velocity components (u_{RMS}, v_{RMS} , and w_{RMS}) give information on the average magnitude of velocity fluctuations while variance of velocity fluctuations ($\overline{u'^2}, \overline{v'^2}$, and $\overline{w'^2}$) that also appear in averaged Naiver-Stokes equation are proportional to momentum fluxes induced by the turbulent eddies and contribute to additional

normal stresses in fluid elements.

The second moments of fluctuations (i.e. pair of fluctuations of different variables e.g. $\bar{u'v'}$) also provide information on isotropy of the turbulence in addition to information on turbulent momentum fluxes in averaged Naiver-Stokes equation [37, Malasekera W. & Versteeg H. K.].

Turbulent Kinetic Energy: The concept of variance can further be extended to total kinetic energy (k) per unit mass contained in respective velocity fluctuations at given location.

$$k = \frac{1}{2}(\bar{u'^2} + \bar{v'^2} + \bar{w'^2}) \quad (18)$$

The values of $\bar{u'^2}, \bar{v'^2}, \bar{w'^2}$ and $-\bar{u'v'}$ are highest found in region where the mean velocity gradient $\partial U / \partial y$ is largest, which shows connection between turbulent production and shear mean flows. The rigorous mixing process in turbulent zone transport these properties towards and across the center line.

1.6.1 Energy cascade

The turbulent kinetic energy is injected into the system from the mean flow stream into the largest turbulent eddies characterized by comparatively high Reynolds number where the role of viscosity is negligible. But these large eddies are unstable in nature and break up while transferring energy to smaller and smaller eddies. This cascade of energy down to smaller eddies continuous until the Reynolds number is small enough for the eddies to be stable and energy gets dissipated into heat by the action of viscosity. The rate at which such dissipation occurs or the rate at which the energy is transferred to smaller eddies, is known as dissipation rate ($\epsilon \sim k^{(3/2)} / l$). In the absence of continuous external energy source at the beginning of the energy cascade, to keep up the turbulent motion and to compensate the dissipation at the end, turbulence and turbulent kinetic energy will decay [63, Pope]. The large scale motions are characterized by anisotropic nature while the small scales are considered to be locally isotropic.

The largest eddies in the flow contribute to the main part of transport and mixing, the length and time scale associated to such largest eddies are known as *Integral length scale* (L_0) and *Integral time scale* ($\tau_0 \sim k / \epsilon$) respectively. The increase in τ_0 corresponds to slow transfer of energy and vice-versa. The intermediate scale is known as the *Taylor micro scale* or *Turbulence length scale*, which is important to determine turbulent properties. At this length scale, the fluid viscosity significantly effect the turbulent eddies in the fluid flow. Below Taylor micro scale the fluid motions are subjected to viscous effects. The smallest scale in the fluid flow are known as the *Kolomogorov micro scale* where the viscous effect is sufficiently high that it prevents generation

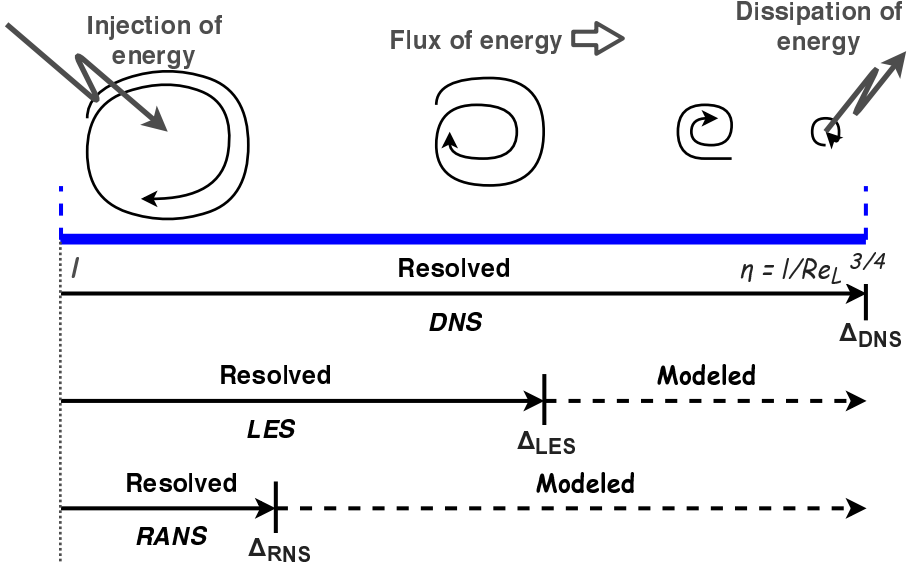


Figure 5: The energy cascade showing the transfer of energy in different sub-ranges.
Concept from: [29, Horstmann S.,2000]

of infinitely small scales of motion by dissipating such small scale energy to heat [86, Zistl, 2014]. The length and time scales associate to Kolmogorov scales are $l_k \sim (\nu^3/\epsilon)^{1/4}$ and $\epsilon \sim (\nu/l)^{1/2}$. The relationship between largest scale (l_0) and smallest scale (l_k), length and time scale is

$$\frac{l_0}{l_k} \sim Re^{(3/4)} \quad (19)$$

$$\frac{\epsilon_0}{\epsilon_k} \sim Re^{(1/2)} \quad (20)$$

As the Reynolds number is increased, the above ratio also increase, which is even more for the time ratio, i.e. the difference in time between largest to smallest scales increase with Reynolds number which is known as *Scale separation*. Such scale separation increases with Reynolds number. This can be cause a serious limitations when simulating fluid flow with high value of Reynolds number as the computational cost increases very steeply with Reynolds number.

1.7 OVERVIEW OF NUMERICAL MODELLING AND SIMULATION

The governing dynamics of the fluid are expressed in term of series of partial differential equations (PDEs), which are coupled and non-linear in nature meaning, the dynamics of one influences the other in non-linear fashion. To further complicate the situation reacting fluid flow like combustion processes, requires additional terms to be calculated in parallel which are very non linear too. Therefore, such complicated system of equations are impossible to compute in analytical fashion and requires smart numerical techniques to solve real world situations. But such techniques involving numerical computation addressing multi-physics and multi-scale problem to

minute detail in the real world situations require unimaginable amount of computational effort meaning, very fast processing and storage capabilities. Therefore, smarter and feasible ways to addressed such an issue, brings mainly three strategies of solving and understanding the fluid flow of different nature, which are briefly discussed in the following sections, in particular the following approaches are discussed:

- Reynolds Averaged Navier-Stokes (RANS)
- Large Eddy Simulation (LES)
- Direct Numerical Simulation (DNS)

It is worth mentioning that, DNS approach is used in this thesis to study the fluid behaviour of nitrogen at supercritical pressures. This section is intended to briefly introduce the above approaches while mentioning their superiorities and limitations. To begin with, it is important to understand the origination of different approaches in the first place, for which the introduction to governing equations of the fluid flow is needed.

Conservation of mass: It is a universal fact that, like energy, mass is and has to be conserved (unless it involves processes like nuclear fusion or fission), which can be simply expressed as the following (for detail refer classical textbook on theoretical and numerical combustion [62, Poinsot & Veynate, 2001]):

$$\frac{\partial \rho}{\partial t} + \frac{\partial \rho u_i}{\partial x_i} = 0 \quad (21)$$

The subscript i refers to the direction in x-y-z (cartesian co-ordinate system) where $i = 1, 2$ and 3 are x, y and z-components respectively.

Mass fraction conservation of species k : For multi-species reactive flow like that in combustion process, the above equation can be expressed in terms of every individual species as a function of mass fraction, diffusion velocity and reaction rate of each species. More the number of species involved in the process like that with the reactions involving large hydrocarbons, the more the number of equations to be solved, which complicates the problem while consuming more computational resource.

$$\frac{\partial \rho Y_k}{\partial t} + \frac{\partial \rho u_i Y_k}{\partial x_i} + \frac{\partial V_{k,i} Y_k}{\partial x_i} = \dot{\omega}_k \quad (22)$$

Conservation of momentum: For both case of reacting and non-reacting flows, the momentum equation is the same:

$$\frac{\partial(\rho u_i)}{\partial t} + \frac{\partial \rho u_i u_j}{\partial x_j} = -\frac{\partial p}{\partial x_j} + \frac{\partial \tau_{ij}}{\partial x_i} + \rho \sum_{k=1}^N Y_k F_{k,j} \quad (23)$$

$$= \frac{\partial \sigma_{ij}}{\partial x_i} + \rho \sum_{k=1}^N Y_k F_{k,j} \quad (24)$$

Where $Y_k = m_k/m$ is the mass fraction of species k , $p = \sum_{k=1}^N p_k$ is the pressure, $F_{k,j}$ is the volume force acting on species k in direction j , τ_{ij} is the viscous tensor which is defined as:

$$\tau_{ij} = \mu \left(\frac{\partial u_i}{\partial x_j} + \frac{\partial u_j}{\partial x_i} \right) - \frac{2}{3} \mu \frac{\partial u_k}{\partial x_k} \delta_{ij} \quad (25)$$

Where μ is the dynamic viscosity (the kinematic viscosity is $\nu = \mu/\rho$), δ_{ij} is the Kronecker symbol whose value is unity if $i = j$ and is null otherwise, and the σ_{ij} tensor can be defined with the pressure and viscous tensors as:

$$\sigma_{ij} = \tau_{ij} - p \delta_{ij} \quad (26)$$

Conservation of energy in terms of sensible enthalpy (h_s):

$$\begin{aligned} \rho \frac{D h_s}{D t} = & \dot{\omega}_T + \frac{D p}{D t} + \frac{\partial}{\partial x_i} \left(\lambda \frac{\partial T}{\partial x_i} \right) - \frac{\partial}{\partial x_i} \left(\rho \sum_{k=1}^N h_{s,k} Y_k V_{k,i} \right) \\ & + \tau_{ij} \frac{\partial u_i}{\partial x_j} + \dot{Q} + \rho \sum_{k=1}^N Y_k F_{k,i} V_{k,i} \end{aligned} \quad (27)$$

\dot{Q}	heat source term (due to for example radiative flux, laser, spark but NOT due to combustion)
$\rho \sum_{k=1}^N Y_k F_{k,i} (u_i + V_{k,i})$	power produced by volume forces F_k on species k
q_i	the energy heat flux = $\rho \sum_{k=1}^N h_k Y_k V_{k,i} - \lambda \frac{\partial T}{\partial x_i}$
$\lambda \frac{\partial T}{\partial x_i}$	heat diffusion expressed by Fourier Law
$\rho \sum_{k=1}^N h_k Y_k V_{k,i}$	term associated with the diffusion of species
$\dot{\omega}_T$	heat release due to combustion = $-\sum_{k=1}^N \Delta h_{f,k}^\circ \dot{\omega}_k$

If the mixture contains only one species or if all the species have same sensible enthalpy the term $\frac{\partial}{\partial x_i} \left(\rho \sum_{k=1}^N h_{s,k} Y_k V_{k,i} \right)$ in the enthalpy equation 27 is equal to zero. However, in some cases, it is neglected as compared to $\dot{\omega}_T$ [62, Poinsot & Veynante, 2001].

The above governing equations give fundamental insight to understanding the physics phenomena involved in the fluid flow. For a simplest non-reacting fluid flow the output of the above series of equation would be u_i i.e. velocity field and scalar properties like density, pressure and temperature. Turbulence and the resulting fluctuating field strongly influence the flow regime. The large fluctuating zones or large eddy motion contribute to strong mixing, while the fluid parcels are being transported by the eddies carrying momentum and energy in and out of the control volume. These momentum exchange as a result of velocity gradient in turbulent flow causes additional shear stresses, known as *Reynolds stresses*. Similarly, in the presence of

temperature gradient evokes *Turbulent heat fluxes* while, species gradients evokes *Species concentration fluxes*.

Time-averaged Navier Stokes equation give raise to the fluctuating terms in governing equation which provide insight into such fluctuating fields which are already accounted for in a simulation with finest resolution both in time and space, able to solve for the smallest scales in the domain like that in DNS. While, if not solvable due to computation constraints, such informations on fluctuations are to be modelled like in RANS or even LES. Depending on the type of fluid flow, whether constant density or variable density, the averaging process could be either Reynolds averaging or Favre averaging respectively, which are shortly introduced in following subsection.

Reynolds decomposition

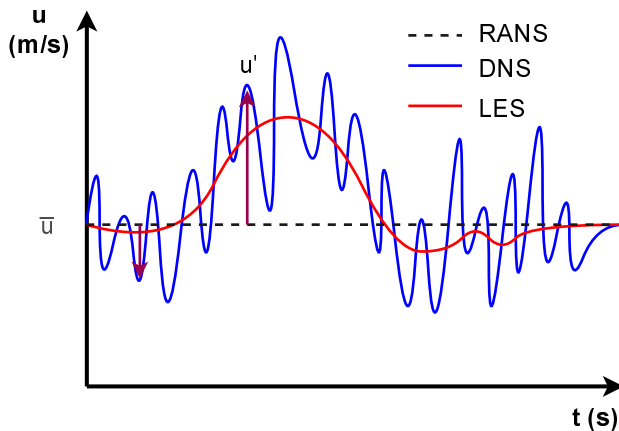


Figure 6: Illustration of velocity fluctuation in time when measured at a point in the flow field, is decomposed into mean and instantaneous fluctuations. Plus, the level of resolution RANS, LES and DNS can account for in the simulation.

Osborne Reynolds proposed that the average variable in the Navier-Stokes equations can be written as a sum of a mean and fluctuations about the mean value. Then, the averaged Navier-Stokes equations are resolved for the mean flow field. Considering ϕ a generic flow variable, the Reynolds average can be written as:

$$\phi = \bar{\phi} + \phi' \quad (28)$$

Where the $\bar{\phi}$ is the averaged value and the ϕ' is the fluctuation about the mean value. The RANS (Reynolds Averaged Navier-Stokes) equations can be derived by substituting the above Reynolds decomposition for every fluid dynamics fields in Navier-Stokes equations, while the unclosed terms requires some closure models (like $k-\epsilon$ model that makes possible to solve only the mean value of all quantities throwing the fluctuations away).

This averaging procedure is also known as the Reynolds averaging. This approach can be suitable for non-reacting flows where the density can be considered as constant and therefore, the fluctuations in density can be neglected. But in the turbulent reacting flows, the volume expansion and heat release causes considerable amount of fluctuations in density and the Reynolds averaging for variable density flows introduces many other unclosed correlations between the quantity (say) ϕ and density fluctuations $\bar{\rho}'\phi'$ [62, Poinsot & Veynante, 2001]. Therefore, the way to average the equation for changing density field is Favre averaging.

Favre averaging

Every variable is now decomposed into:

$$\phi = \tilde{\phi} + \phi'' \quad (29)$$

Where the $\tilde{\phi}$ is the Favre averaged quantity which is density-weighted quantity. Such averaging can be carried out both in time and space. Some important rules in Favre averaging are:

$$\begin{aligned} \tilde{\phi} &= \frac{\bar{\rho}\phi}{\bar{\rho}} \quad \widetilde{\phi''} = 0 \\ \overline{\rho\phi''} &= 0 \quad (\overline{\phi''} \neq 0 \text{ and } \overline{\phi''\phi''} \neq 0) \\ \alpha\tilde{\phi} &= \bar{\alpha}\tilde{\phi}; \quad \overline{\rho\alpha\phi} = \bar{\rho}\bar{\alpha}\tilde{\phi} + \overline{\rho\alpha''\phi''} \end{aligned}$$

The symbols α and ϕ are both arbitrary variables. Such averaging formulation can be applied to the governing equation to obtain the filtered or averaged governing equation used in RANS and LES. However, averaging process can only be applied to some particular direction in time or space known as homogeneous direction. For the simulation discussed in the thesis, the averaging or homogeneous direction is y-direction (which is also cross-wise direction) and time.

The relationship between Reynolds and Favre averages is not very straight forward, and requires correlation between density and variable fluctuation $\bar{\rho}'\phi'$. In contrast to reynolds decomposition, where ϕ' represents a turbulent velocity fluctuation, the quantity ϕ'' also includes the effect of density fluctuations. If the flow is incompressible, the density is constant, so $\tilde{\phi} = \bar{\phi}$ and $\phi'' \equiv \phi'$. The main advantage of Favre averaging, is the reduction of unknown correlations (products of fluctuating quantities).

$$\overline{\rho\tilde{\phi}} = \overline{\rho\bar{\phi}} + \overline{\rho'\phi'} \quad (30)$$

1.7.1 RANS and Turbulence Modelling

In most of the engineering real world applications, where the solution to a problem is require fast with significant understanding to address the problem, where minute details might not be of extreme importance. In such cases,

time independent mean values of the turbulent quantities can tell most the the important information on the flow field. This convenient and simplified approach is used widely and known as *Reynolds Averaged Navier-Stokes* method, which average out the unsteadiness in *time*. The averaged Navier-Stokes equations are then solved for the mean flow field.

The conservation of mass, momentum and energy equation (discussed in first portions of section 1.7), can now be averaged with above mentioned Favre averaging to obtain the following set of averaged equations (detail discussion on this topic can be found in [62, Poinsot & Veynante, 2001], [63, Pope S.B., 2000] and [37, Malasekera W. & Versteeg H. K.]):

- **Conservation of mass:**

$$\frac{\partial \bar{\rho}}{\partial t} + \frac{\partial (\bar{u}_i \bar{\rho})}{\partial x_i} = 0 \quad (31)$$

- **Conservation of momentum:**

$$\frac{\partial \bar{u}_i \bar{\rho}}{\partial t} + \frac{\partial (\bar{\rho} \bar{u}_i \bar{u}_j)}{\partial x_i} + \frac{\partial \bar{p}}{\partial x_j} = \frac{\partial}{\partial x_i} (\bar{\tau}_{ij} - \bar{\rho} \widetilde{u''_i u''_j}) \quad (32)$$

- **Conservation of energy** in terms of sensible enthalpy:

$$\begin{aligned} \frac{\partial \bar{\rho} \widetilde{h}_s}{\partial t} + \frac{\partial}{\partial x_i} (\bar{\rho} \widetilde{u}_i \widetilde{h}_s) &= \widetilde{\omega}_T + \overline{\frac{Dp}{Dt}} + \frac{\partial}{\partial x_i} \left(\lambda \overline{\frac{\partial T}{\partial x_i}} - \overline{\rho u''_i h''_s} \right) \\ &\quad + \overline{\tau_{ij} \frac{\partial u_i}{\partial x_j}} - \left(\overline{\rho \sum_{k=1}^N V_{k,i} Y_k h_{s,k}} \right) \end{aligned} \quad (33)$$

where, the term $\overline{\frac{Dp}{Dt}}$ can be expressed as

$$\overline{\frac{Dp}{Dt}} = \frac{\partial \bar{p}}{\partial t} + \overline{u_i \frac{\partial p}{\partial x_i}} \quad (34)$$

$$= \frac{\partial \bar{p}}{\partial t} + \widetilde{u}_i \overline{\frac{\partial p}{\partial x_i}} + \overline{u''_i \frac{\partial p}{\partial x_i}} \quad (35)$$

- **Conservation of species mass fraction:**

$$\frac{\partial (\bar{\rho} \widetilde{Y}_k)}{\partial t} + \frac{\partial}{\partial x_i} (\bar{\rho} \widetilde{u}_i \widetilde{Y}_k) = - \frac{\partial}{\partial x_i} (\overline{V_{k,i} Y_k} + \bar{\rho} \widetilde{u''_i Y''_k}) + \overline{\omega_k} \quad (36)$$

An issue yet to be addressed with the above mentioned time-averaged system of equation is that, those equations contain new terms like $\widetilde{u''_i Y''_k}$, $\overline{u''_i \frac{\partial p}{\partial x_i}}$, $\overline{\rho u''_i h''_s}$, $\widetilde{u''_i u''_j}$ etc. which cannot be represent as a function of the mean quantities, meaning that the system has more unknown terms than the number of equations, therefore, cannot be solved which is popularly known to be '*unclosed equations*', and has to be modelled in some way, known as *closure models*, and this problem is known to be *turbulence closure problem*. Such unknown correlation terms describe the influence of turbulent fluctuations on the mean

flow field. The unknown or the unclosed terms in the above equations are the following:

- Reynolds stress tensor ($\widetilde{u''_i u''_j}$):

It appears in the momentum equation and are the product of fluctuating velocity fields. They are associated with convective momentum transfer due to turbulent eddies, which causes additional turbulent stresses on the mean velocity components. Among six such stresses, 3 are normal components ($\overline{u_{i=1}^2}$) while other 3 are shear components ($\overline{u'_{i \neq j} u'_{j \neq i}}$). The normal components are nothing but the variance in x-y-z directions while, the shear components are the second order moments. The classical turbulence model for modelling Reynolds stresses is the *Turbulence / Eddy viscosity model*.

- Eddy viscosity closure model:

It is based on a concept that the Reynolds stresses can be related to the strain rate (which is related to the velocity gradient) of the mean flow with turbulent dynamic viscosity μ_t as a proportionality coefficient. It was proposed by Boussinesq in 1877, where the Reynolds stresses can be expressed in terms of strain rate and viscous tensor (expressed in equation 25). This shows that there exists an analogy between viscous stress and reynolds stress on the mean flow. For Newtonian fluid such relation can be expressed as:

$$\overline{\rho \widetilde{u''_i u''_j}} = \overline{\rho u''_i u''_j} = -\mu_t \left(\frac{\partial \widetilde{u}_i}{\partial x_j} + \frac{\partial \widetilde{u}_j}{\partial x_i} - \frac{2}{3} \frac{\widetilde{u}_k}{\partial x_k} \delta_{ij} \right) + \frac{2}{3} \overline{\rho k} \quad (37)$$

As discussed previously, $\mu_t = \bar{\rho} \nu_t$, ν_t and δ_{ij} are turbulent dynamic viscosity, turbulent kinematic viscosity and Kronecker delta respectively. Now, in order to evaluated μ_t , 3 popular approaches have been put forward depending on number of extra equations needed to be solved viz.

# of equations	Name	Approach
0	Mixing length Model	μ_t is algebraically expressed in terms of velocity gradient (mean stress tensor(\widetilde{S})), and mixing length $\mu_t = l_m^2 \bar{\rho} \widetilde{S}$
1	Prandtl-Kolmogorov Model	turbulent k.e. k is incorporated with characteristic length and constant $\mu_t = \bar{\rho} l_c \sqrt{k} C_\mu; \quad C_\mu = 0.09$
2	$k - \epsilon$ Model	turbulent k.e. k and its dissipation rate ϵ are expressed using two balance equations

$$\mu_t = \bar{\rho} C_\mu \frac{k^2}{\epsilon}$$

Table 7: Closure models to evaluate the turbulent viscosity (μ_t).

- Turbulent species transport ($\widetilde{u_i'' Y_k''}$):

For isotropic turbulence the transport term $\widetilde{u_i'' Y_k''}$ is traditionally described by a gradient eddy viscosity model. With the help of classical gradient assumption, the species transport turbulent fluxes can be modelled as:

$$\bar{\rho} \widetilde{u_i'' Y_k''} = - \frac{\mu_t}{Sc_{kt}} \frac{\partial \bar{Y}_k}{\partial x_i} \quad (38)$$

The turbulent Schmidt number $Sc_{kt} = \frac{v_t}{K}$ (ratio between eddy viscosity and eddy diffusivity) for species k and turbulent viscosity μ_t (which is obtained from the turbulence models), are needed. However, the reliability of this gradient assumption is still questionable for some turbulent premixed flames as pointed out by Poinsot in his book.

- Mean reaction rate ($\bar{\omega}_k$):

The fluctuating scalar like temperature or concentration can significantly affect the mean reaction rate. The rates of chemical reactions have a strong dependence on temperature. It is well known that $\bar{\omega} \neq \bar{\omega}(\bar{Y}, \bar{T})$. One of the most challenging modelling issue in combustion process is to find good models for the source term $\bar{\omega}_k$ [86, Zistl, 2014].

From the above discussion, one can have a glimpse of modelling in RANS simulation. The general-purpose CFD code is considered considerably accurate, economical and simple, thanks to such modelling approaches. The most common RANS turbulence models in commercially available CFD codes based on number of additional transport equations needed to be solved along with the RANS flow equations are listed below:

# of extra equations	Name
0	Mixing length model
1	Spalart-Allmaras model
2	k- ϵ model
	k- ω model
	Algebraic stress model
7	Reynolds stress equation model (also known as second order closure model)

Table 8: Well known standard turbulence models used in popular commercial CFD codes [37, Malasekera W. & Versteeg H. K.].

Strengths of RANS

- It is the most economical and fastest, therefore, minimizes time and costs, suitable for most of the engineering and industrial applications.
- The models like $k-\epsilon$ are robust and easily to implement in CFD codes [86, Zistl, 2014].
- Can be used for highly complex geometries [26, Gibbs,2014].

Limitations of RANS

- Only the mean flow field is resolved leaving most of the temporal and fluctuating informations unknown.
- Since all the scales are modelled, such models are not universal and due to the fact that the large scales are very sensitive to initial and boundary conditions, tuning of models is required for specific applications.
- Models contain empirical constants that cannot be optimized for several different flow at the same time [86, Zistl, 2014].
- Most accurate turbulence models give rise to highly complex set of equations leading to convergence issues [26, Gibbs,2014].

1.7.2 LES and SGS modelling

The behaviour of small eddies are isotropic and is expected to have universal behaviour [37, Malasekera W. & Versteeg H. K.], [69, Selle,L. et al., 2008]. While the larger eddies, which extract energy from the mean flow are more anisotropic and are highly sensitive to boundary and initial conditions [86, Zistl, 2014]. The turbulence models used in RANS simulation is expected to describe the collective behaviour of such small as well as large eddies, and it's intensely difficult to find the best model which does this job with perfection. Therefore, a new approach was developed in dealing such problem, i.e. instead of looking for a single model describing the behaviour of large and small eddies, larger eddies (larger than the computational mesh grid size) which is characterized by anisotropic nature and contribute to main part of the turbulent transport, can be computed for each problem with a time dependent simulation while, the universal behaviour of small eddies can be modelled. Such modelling of smaller eddies contribution used in LES is terms as *Sub-Grid Scale (SGS) modelling*. This is the concept behind the LES treatment of turbulence.

Unlike time-averaging carried out in RANS, LES employs spatial averaging or spatial filtering operation. One of the important thing in LES, is the distinction between the larger eddies (which are computed) and smaller eddies (which are modelled). The *filter cut-off-width* Δ defines such boundary

between what to be retained (via numerical computation) and what to be rejected (via filtering operation). Such filtering operations introduce unknown terms also known as sub-grid-scale stresses, and therefore their effect on the mean flow is described or modelled with the help of SGS models. LES provides instantaneous resolved field. If say ϕ is variable in consideration which is function of both time and space ($\phi(x, t) = \phi(x, y, z, t)$), the filtering function $G(x, x', \Delta)$ is such that:

$$\bar{\phi}(x, t) = \int_{-\infty}^{+\infty} G(x, x', \Delta) \phi(x', t) dx' \quad (39)$$

It should be noted that just like time averaging carried out in RANS, filtering operation is also an integration operation carried out in three-dimensional space. But unlike RANS, the $\bar{\cdot}$ represents the special filtering operation and NOT time averaging. Some of the popular filtering operations are:

- Top-hat or box-filter: It is used in Finite-Volume implementation in LES.
- Gaussian filter: It was introduced for LES by the Stanford group which is used intensively as turbulence modelling tool.
- Spectral filter: It uses Fourier series to explain the flow variables which gives sharp cut-off in energy spectrum at wavelength of Δ/π and is used very often in turbulence research [37, Malasekera W. & Versteeg H. K.].

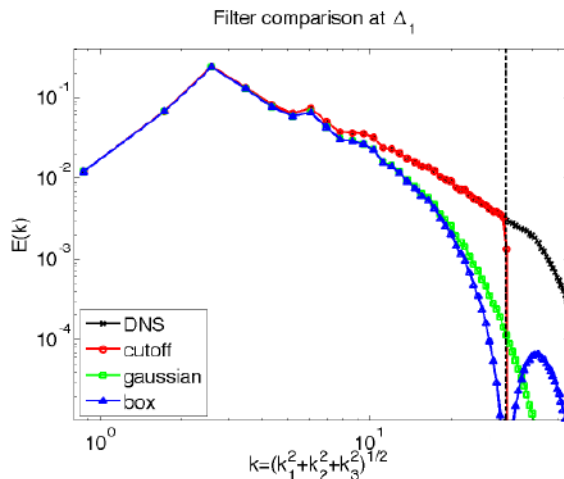


Figure 7: Comparison between different filters used in sub-grid scale modelling [73, Stoll,R., 2014].

The common practice for the selection of cut-off-width is of the same order as a grid size. In 3D computation with a grid cells $\Delta x, \Delta y$, and Δz , the cut-off-width is then defined as:

$$\Delta = \sqrt[3]{\Delta x \Delta y \Delta z} \quad (40)$$

Just like averaged equation in RANS, the filtered equation in LES consists of some resolved part (i.e. $\bar{\phi}$) and unresolved part (i.e. ϕ'). But in RANS

formulation $\bar{\phi}' = 0$ or $\langle \phi' \rangle = 0$, but in LES $\tilde{\phi}' \neq 0$, in particular $\widetilde{\phi' \alpha'} \neq \overline{\phi' \alpha'}$. In LES similar to Favre averaging process, the filtered value of perturbation is not zero and filtered value is not the same as its double filtered value i.e. ($\bar{\phi}' \neq 0$ and $\overline{\bar{\phi}} \neq \bar{\phi}$). Where as in time-averaging case $\overline{\phi(t)} = \bar{\phi}(t)$. With the above consideration, the filtered balance equations can be expressed as the following ([62, Poinsot & Veynante, 2001]):

- **Conservation of mass:**

$$\frac{\partial \bar{\rho}}{\partial t} + \frac{\partial (\tilde{u}_i \bar{\rho})}{\partial x_i} = 0 \quad (41)$$

- **Conservation of momentum:**

$$\frac{\partial \tilde{u}_i \bar{\rho}}{\partial t} + \frac{\partial (\bar{\rho} \tilde{u}_i \tilde{u}_j)}{\partial x_i} + \frac{\partial \bar{p}}{\partial x_j} = \frac{\partial}{\partial x_i} (\overline{\tau_{ij}} - \bar{\rho} (\widetilde{u_i u_j} - \tilde{u}_i \tilde{u}_j)) \quad (42)$$

- **Conservation of energy** in terms of sensible enthalpy:

$$\begin{aligned} \frac{\partial \bar{\rho} \tilde{h}_s}{\partial t} + \frac{\partial}{\partial x_i} (\bar{\rho} \tilde{u}_i \tilde{h}_s) &= \widetilde{\omega_T} + \overline{\frac{Dp}{Dt}} + \frac{\partial}{\partial x_i} \left(\overline{\lambda \frac{\partial T}{\partial x_i}} - \bar{\rho} (\widetilde{u_i h_s} - \tilde{u}_i \tilde{h}_s) \right) \\ &\quad + \overline{\tau_{ij} \frac{\partial u_i}{\partial x_j}} - \left(\rho \sum_{k=1}^N V_{k,i} Y_k h_{s,k} \right) \end{aligned} \quad (43)$$

Where,

$$\overline{\frac{Dp}{Dt}} = \frac{\partial \bar{p}}{\partial t} + \overline{u_i \frac{\partial p}{\partial x_i}} \quad (44)$$

- **Conservation of species mass fraction:**

$$\frac{\partial (\bar{\rho} \widetilde{Y}_k)}{\partial t} + \frac{\partial}{\partial x_i} (\bar{\rho} \tilde{u}_i \widetilde{Y}_k) = - \frac{\partial}{\partial x_i} (\overline{V_{k,i} Y_k} + \bar{\rho} (\widetilde{u_i Y_k} - \tilde{u}_i \widetilde{Y}_k)) + \overline{\omega_k} \quad (45)$$

In the above filtered equation, the unresolved terms include the following:

- SGS stress ($\tau_{ij} = \bar{\rho} \tilde{u}_i \tilde{u}_j - \bar{\rho} \tilde{u}_i \tilde{u}_j$):

It appears in the filtered momentum equation and is mostly attributed to convective momentum transport due to interaction between unresolved SGS eddies. It can be further expressed as

$$\widetilde{u_i u_j} - \tilde{u}_i \tilde{u}_j = \underbrace{(\widetilde{\tilde{u}_i \tilde{u}_j} - \tilde{u}_i \tilde{u}_j)}_{L_{ij}} + \underbrace{\widetilde{\tilde{u}_i u'_j} + \widetilde{u'_i \tilde{u}_j}}_{C_{ij}} + \underbrace{\widetilde{u'_i u'_j}}_{R_{ij}} \quad (46)$$

Leonard Stresses (L_{ij}) are due to unresolved scales. Mathematically, this is due to the fact that in spatial averaging/filtering operation, the second filter operation make a change to filtered flow variable as $\overline{\bar{\phi}} \neq \bar{\phi}$ [37, Malasekera W. & Versteeg H. K.].

Crosses stresses (C_{ij}) are due to interactions of SGS eddies with resolved flow field.

LES Reynolds stresses (R_{ij}) are caused by convective momentum transfer due to interaction of SGS eddies and are modelled with SGS turbulence models.

- Enthalpy fluxes ($\widetilde{u_i h_s} - \widetilde{u}_i \widetilde{h}_s$) and species fluxes ($\widetilde{u_i Y_k} - \widetilde{u}_i \widetilde{Y}_k$)
- Species diffusion fluxes ($\overline{V_{k,i} Y_k}$) and enthalpy diffusion fluxes ($\overline{\lambda \frac{\partial T}{\partial x_i}}$)
These molecular fluxes can be modelled via gradient assumption like in RANS.
- Chemical reaction rate ($\overline{\omega_k}$)
- Pressure gradient term ($\overline{u_i \frac{\partial p}{\partial x_i}}$)

The advantage of LES over RANS in terms of modelling unresolved variables, is that the resolved information of large scale turbulent motion is known as they are numerically resolved in LES. So, the closure models are based on similarity assumptions using the known largest structures and their influence on the smaller ones [62, Poinsot & Veynante, 2001]. Some of the popular SGS closure models are listed in the following table.

Closure Models	Approach
Samagorinsky - Lilly SGS model	<p>Is modelled similar to Boussinesq hypothesis i.e. local SGS stresses $\tau_{ij} \propto$ local strain rate of resolved flow</p> $\tau_{ij} = -\mu_{SGS} \left(\frac{\partial \bar{u}_i}{\partial x_j} + \frac{\partial \bar{u}_j}{\partial x_i} \right) + \frac{1}{3} \tau_{ii} \delta_{ij};$ <p>SGS viscosity is modelled as</p> $\mu_{SGS} = \rho (C_{SGS} \Delta)^2 \sqrt{2 \bar{S}_{ij} \bar{S}_{ij}}$ <p>where the Constant $C_{SGS} \in [0.1, 0.24]$, whose value is effect of mean flow strain; because small eddies are not purely isotropic, best approach would be case-by-case adjustment of C_{SGS}</p>
Higher order SGS model	<p>Replaces velocity scale by turbulent SGS kinetic energy</p> $\mu_{SGS} = \rho (C'_{SGS} \Delta) \sqrt{k_{SGS}}$
Scale Similarity model	<p>SGS stresses \propto stress due to eddies at smallest resolved scale, where C' is an adjustable constant</p> $\tau_{ij} = \rho C' (\bar{u}_i \bar{u}_j - \bar{\bar{u}}_i \bar{\bar{u}}_j)$
Mixed model	<p>Damping term added to deal with dissipating effect of Samagorinsky model i.e.</p> $\tau_{ij} = \rho C' (\bar{u}_i \bar{u}_j - \bar{\bar{u}}_i \bar{\bar{u}}_j) - 2\rho C_{SGS}^2 \Delta^2 \bar{S} \bar{S}_{ij}$ <p>value of constant $C' \sim 1$ depends on Δ</p>

Table 9: Some important SGS closure models used in LES.

Strengths of LES

- As the larger scales which are of importance in mixing process are simulated directly and not averaged, therefore, gives better result in compared to RANS simulation, especially in combustion process where mixing plays a vital role.
- Because of the fact that, the smaller scales are modelled, the low Reynolds number limitation of DNS is not applied to LES.
- LES is not as expensive as DNS in terms on computational cost.
- LES is inherited by unsteady features [62, Poinsot & Veynante, 2001].
- Since the small scales are comparatively considered to have universal behaviour modelling in LES is not as complicated as for RANS where the entire spectrum of scales are supposed to be modelled.

Limitations of LES

- Since large eddies (which are resolved in LES) are very sensitive to initial and boundary conditions, such cases (like near walls) are to be cautiously dealt with and therefore, LES requires precise codes. In addition to it, the effect of back scattering (i.e. the energy cascade from larger to smaller eddies is not always 100 %, small portion of the energy flow is reversed called *inverse energy cascade*, where the process of energy transfer is from smaller to larger eddies known as *back scattering*) has to be incorporated into the code [86, Zistl, 2014].
- Even though LES is not as expensive as DNS, it still requires lot of computer time and cost.
- Although LES has been around since 1960s, it is still under development for complex and reactive flows.

1.7.3 Direct Numerical Simulation

In DNS (Direct Numerical Simulation), complete instantaneous Navier-Stokes equation with continuity equations are solved which include equations 21, 22, 24, and 27, in sufficiently fine spatial mesh and small time steps able to resolve even the smallest eddies and fastest turbulent fluctuations in a domain, without any turbulence models.

DNS of compressible turbulent flow, where shock waves are produces and its interaction with turbulence could be pretty complicated, is comparatively new, in contrast to its incompressible counterpart. In addition to it, aero-acoustics invasion to turbulence adds further complexity to the problem. DNS can also be used to simulate ideal flows which cannot be obtained in real world laboratory to understand the physics of an idea fluid.

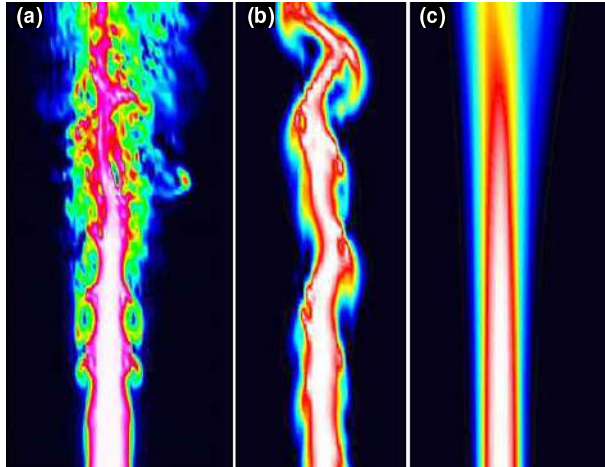


Figure 8: (a) DNS, (b) LES and (c) RANS prediction of a turbulent jet. [38, Maries, A.]

1.8 CHALLENGES IN DNS

When modelling the fluid flow, the velocity field is 3D, time-dependent and random. The difficulties lies within the Navier-Stokes equation, from the non-linear convective term in particularly from the pressure gradient term. When it is expressed in terms of velocity (via Possion equation), the pressure gradient term is both non linear and non-local (as discussed in detail by [63, Pope S.B., 2000] in his book *Turbulent Flows* Page 335-350). The precise and correct DNS of turbulence requires appropriate numerical scheme with proper discretization in space and time-marching in time, able to capture wide range of length and time scales.

1.8.1 *Spatial resolution*

The mathematical equations governing the fluid flow are described in terms of differential equations which are non-linear in nature and are normally coupled. Simulation requires approximation of such differential equations in terms of system of algebraic equations applied to small domains in space and time i.e. in discrete locations, allowing the computer to solve for it at each of such locations. Therefore, the equations demands discretizations. Finer the discretizations, better is the resolutions and therefore, the result incorporates the smallest details.

Along the homogeneous direction (i.e. the averaging direction), the largest scales in the flow is determined by physical parameters such as boundary layer thickness, channel width, or mixing layer thickness [44, Moin & Mahesh, 1998]. The resolution is has to be fine enough to accurately capture the smallest length scale and the fastest dissipation. Such smallest length scale depends on the energy spectrum in the $\mathcal{O}(\eta)$ and is typically greater than the Kolmogorov length scale ($\sim 15\eta$). The most important discretiza-

tion methods are the Finite Volume Method (FVM), Finite Element Method (FEM), Finite Difference Method (FDM) and Spectral Method. The accuracy of solution is very much dictated by the quality of discretization. As pointed out by Moin and Mahesh (1998) - spatial discretization error has coupling of differentiation error and error associated with the non-linearity of governing equations. The physics (e.g. dissipation), on the other hand dictates the smallest scales that needs to be resolved and the accuracy with which it needs to be represented. The second order central difference method requires greater resolution with lower accuracy while higher order like fourth-order central difference, sixth-order Pade and Fourier spectral scheme require mesh spacing comparatively larger with same level accuracy.

Spectral methods are based on Fourier series decomposition in periodic direction and polynomial expansions in directions with solid walls, which is economical and have high convergence rates and therefore, widely used in turbulence research [37, Malasekera W. & Versteeg H. K.]. The other method is *Spectral element method (SEM)*, which is also used in the DNS of supercritical fluid discussed in this thesis. SEM combines the geometric flexibility of FEM with good convergence property of spectral method.

The other very crucial source of error is *aliasing*, which can cause either numerical instability or excessive turbulence decay [44, Moin & Mahesh, 1998]. The small scales are characterized by larger levels of aliasing error. Spectral methods have higher level of aliasing error compared to finite differences schemes.

1.8.2 *Temporal advancement*

The wide range of time scales involved in the Turbulent flow, makes the system of equations stiff. Stiff systems are those for which certain numerical methods are numerically unstable, causing rapid variations in the solutions, unless the resolution or the step size is extremely small. In a study by Choi and Moin (1994), very large time steps were found to cause the turbulence in the channel to decay to laminar state. The implicit time advancement and large time steps employed for most of the stiff systems in general-purpose CFD are not suitable for DNS as the time resolution should be sufficiently small to capture the fastest dissipation process [37, Malasekera W. & Versteeg H. K.]. This requires, special methods that ensure numerical stability and accuracy. A common practice as pointed out by [44, Moin & Mahesh, 1998], for incompressible DNS of wall-bounded flows, implicit time advancement for the viscous terms and explicit time advancement for the convective term can be employed.

1.8.3 Boundary conditions

It is tricky and challenging to impose a correct boundary and initial conditions for DNS with turbulence. For incompressible homogeneous directions (for instance along spanwise direction in fully developed pipe flow), periodic conditions can be imposed. The main issue is inflow and outflow boundary conditions [44, Moin & Mahesh, 1998]. Compressibility causes additional boundary condition issues, the interaction of acoustic waves can have an effect onto the solution.

1.8.4 Classical assumptions to reduce computational costs in DNS

The complexities discussed in 1.8.1, 1.8.2, and 1.8.3 should be reduced in order to achieve reasonably accurate result with achievable computational cost of DNS. For that, some noble approximations or simplifications imposed in DNS code are discussed below. The fully compressible formulation (which considers both density and pressure variations) provides better understanding of the flow, like it is able to capture details into interaction of flame and aero acoustics, allowing better understanding of high speed combustion process like that in rocket nozzle, but such formulation demands higher computational cost. Simplifications based on research domain and its thermo-physical situation, provide pretty good information while reducing the computational costs and complexities.

Incompressible flow approximation

Incompressible flow approximation allows to consider a constant density and is independent of pressure and temperature, which is also called *thermo-diffusive* approximation. The major limitation of this approximation for a reacting or complex flow is that the flow modifications due to heat release are not captured in the simulation. So, it's quite a good approximation to consider constant density (incompressibility) for non-reacting flow.

Low Mach number approximation

Low mach number approximation allows variable density while filtering the acoustic waves, independent of pressure. The change is the density could be due to heat release in, changing the temperature. This is a good simplification for low-speed flows, like the ones encountered in subsonic combustion chamber in auto-mobile and aerospace applications. With this approximation, the equation in particularly, energy equation, is considerably simplified since several viscous terms become negligible [86, Zistl, 2014].

Strengths of DNS

- Instantaneous results can be generated in finest details, which can be used to validate or improve empirical turbulence models used for

RANS and/or LES. Such values are impossible to be obtained from measurements.

- The behaviour of ideal or virtual flow field can be modelled with DNS.
- Precise details related to turbulence, their budgets and transport at any given point in the flow field can be computed with DNS, without any need of turbulence models.

Limitations of DNS

- Due to wide range of length and time scales involved in the turbulent flow field, it is very difficult to directly solve the flow equations.
- The number of nodes N in the domain is proportional to the turbulent Reynolds number as $Re_t^{3/4}$. Since turbulence is characterized by its 3D behaviour, the total number of $N \propto Re^{9/4}$, while the characteristic timescale decreases with $Re^{-1/2}$, giving the total cost of simulation proportional to $Re_t^{11/4}$. As one can see that, cost increases very steeply with Re . This limits the DNS capabilities at higher Re . Therefore, the DNS of turbulent reacting flow is limited to low Reynolds number and low Damkohler numbers [63, Pope S.B., 2000].
- Careful attention should be paid on discretization, time-advancement and boundary-initial conditioning for DNS.

1.9 STATE - OF - THE - ART TRANS - SUPERCRITICAL MIXING

The thermo-physical properties of fluids near critical point in the state space diagram as shown in Figure 1, undergo drastic changes in the absence of phase change, where the molecular forces overcome the surface tension creating a single-phase sharing the property of both liquid (e.g. high density) and gas (e.g. high diffusivity). The highly non-linear behaviour near the critical point makes the ideal gas law unable to relate the thermo-physical states. Therefore, real fluid in elevated temperature and pressure conditions like that in combustion chamber of Liquid Rocket Engine requires additional modelling. In addition to it combustion instabilities occur due to strong coupling between heat release, fluid dynamics and acoustic phenomenon. It has been pointed out by [14, Chehroudi, 2012], that the trans-criticality of fluid injection may greatly influence the stability of the system as acoustic pressure oscillations near the critical point have an important effect on the flow and mixing. Therefore, the study of trans- and supercritical reacting and non-reacting flow are of interest since early 1990s.

One of the important benchmark study of supercritical jet in the literature was carried out at Deutsches Zentrum für Luft- und Raumfahrt (DLR) by Mayer *et al.*(1998) [39, Mayer, W. 1996] showing strong diffusive nature

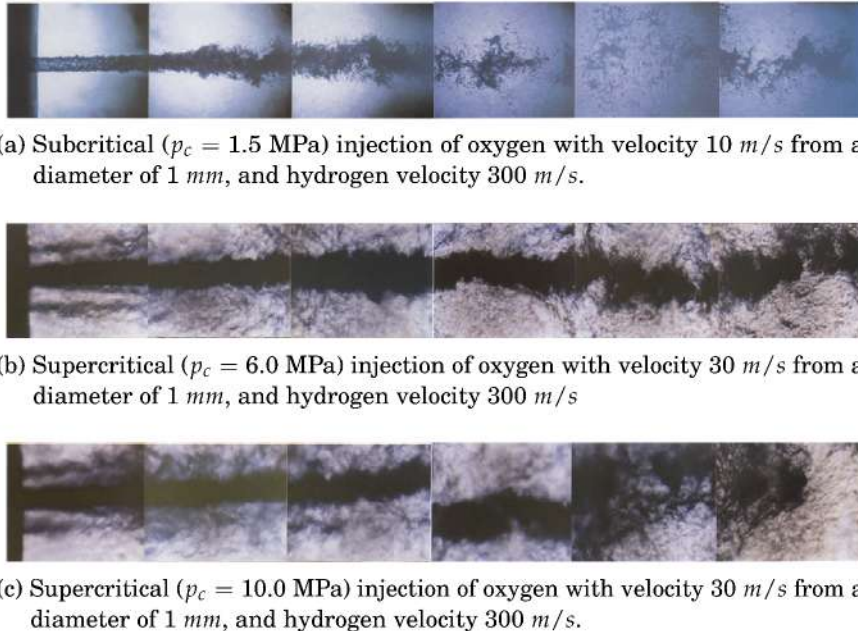
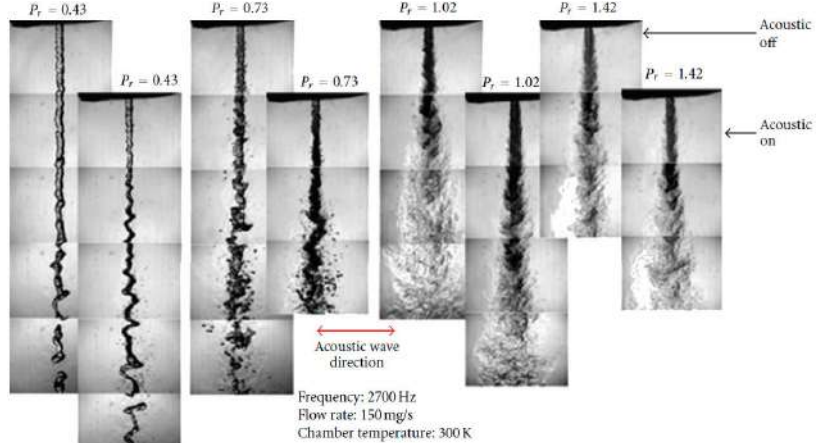


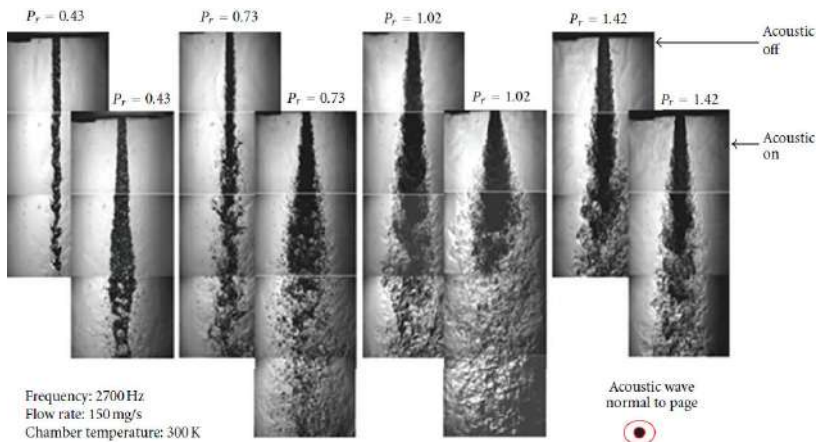
Figure 9: Shadowgraphs of LO_2 - LH_2 co-axial injection at three different pressures, showing the macroscopic behaviour of the oxygen jet taken in a backlight setup, where the six photographs show the time transient behaviour of the oxygen jet during startup transients. [39, Mayer, W. 1996]

of supercritical jet. As shown in Figure 9, the subcritical injection is characterized by process of atomization where the ligaments detach from the LOX jet surface, which form round droplets and finally evaporate. In the contrary, upon approaching and exceeding supercritical pressures, droplets are not visible instead, thread-like structures develop and grow from the liquid jet core which do not detach but rapidly dissolve and fade away. They also pointed out that the such mixing is characterized also by large scale turbulence along with other factors such as dispersion of oxygen ligaments, strong combustion radiation.

It was followed by other experiments by Oschwald & Schik (1999), Chehroudi *et al.*(2002) and Habiballah *et al.*(2006), to have better insight to physical behaviour of super critical non-reacting jets. These works showed that liquid propellant doesn't atomize due to the fact that the surface tension, which hold bounds the liquid surface disappears. Instead, the such fluid undergo a complex liquid-gas like mixing with high diffusivity and is sensitive to temperature and pressure fluctuations. Several visualization of supercritical combustion of LO_x/GH_2 has been carried out by Mayer & Tamura (1995), while Candel *et al.*(1998) investigated the high-pressure shear coaxial injector jet flame which was for the reacting flow. With the advancement of computation tools the focus was drawn towards numerical work to understand supercritical mixing and combustion in rocket engines like the ones by [48, Oefelein & Yang, 1998].



(a) Front View: Acoustic driver located at the left of the jet. The downward shifted images are those with acoustic ON.



(b) Side View: Acoustic driver located behind the page. The downward shifted images are those with acoustic ON.

Figure 10: Shadowgraph images of round liquid nitrogen injected into gaseous nitrogen at different chamber pressures (denoted by reduced chamber pressure: P_r i.e. ratio of chamber pressure by critical pressure of injected nitrogen) [14, Chehroudi, 2012]

The other important group focusing on numerical study of supercritical process is Bellan *et al.*[2, 4, Bellan-2000, 2006] at CALTECH focusing on DNS of temporally evolving mixing layers such as haptane and nitrogen stream, O_2/H_2 [49, Okong & Bellan,2002]. Together with Selle [70, Selle *et al.*, 2007] the sub-grid scale modelling in supercritical environment was studied.

Physical insight to the physic of the problem related to supercritical fluid and injection process was studied by Daniel Banauti [8, Banauti, 2015] showing that the supercritical phase transition doesn't occur in a phase equilibrium but over a finite temperature interval, i.e supercritical transitions require additional energy (apart from the one to overcome intermolecular force of attraction) to increase the temperature. Such energy sink effect

reduces with growing pressure and become negligible for $p/p_{cr} > 3$. The study of widom (pseudo-boiling) line in binary mixtures of supercritical fluids was studied by Raju,M. , Banauti. D. [64, Raju, M. *et al.*, 2017], showing the existance of multiple Widom lines in binary mixtures with the help of molecular dynamics simulations. They showed that for nobel gaeses, depending on the phase behaviour, mixture transition from liquid-like to gas-like regime is through distinctly different pathways. They showed that the binary mixtures have behaviour similar to pure fluid while supercritical state can be characterized by a single liquid-gas transition.

The study of temporal nitrogen-nitrogen gas mixing layer under trans-critical conditions with DNS was carried out by [75, Tani,H. *et al.*, 2012], to understand the influence of the pseudo vaporization at the critical temperature. They showed that the dominant eddies in the development of turbulence were not directly affected by the pseudo vaporization process and thus, the Reynold stress and turbulence heat flux were similar to ideal-gas condition. Also the mean and fluctuation profiles of streamwise velocity and specific enthalpy were similar to that of idea condition, showing that the turbulent transport mechanisms of momentum and heat were little affected by the process of pseudo vaporization. On the other hand, the density profiles were considerably influenced by the pseudo-vaporization, therefore, the mass transport mechanism under the trans-critical condition was found to be influenced by the pseudo vaporization.

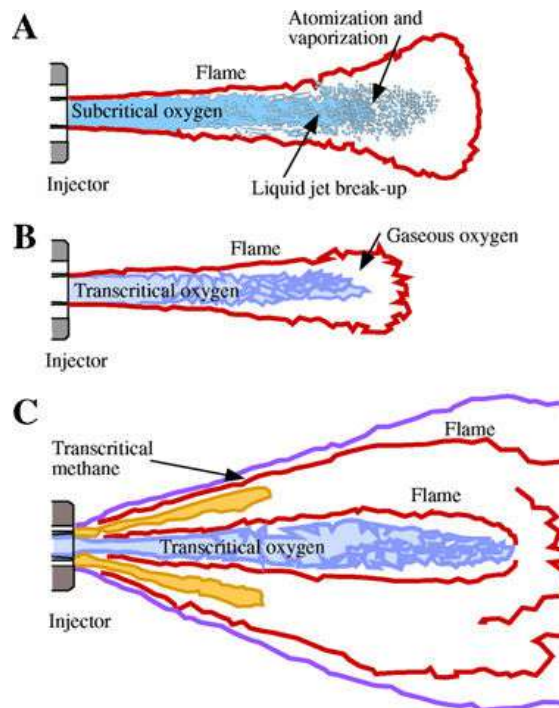


Figure 11: Schematic representation of cryogenic flames. (A) Subcritical oxygen, gaseous methane, (B) Transcritical oxygen, gaseous methane and (C) Transcritical oxygen, transcritical methane [71, Singla,G., *et al.*, 2005].

The mixing process along with investigation of SGS modeling of thermodynamic and transport properties to be used in LES, of a temporal jet under transcritical and supercritical condition with DNS, was studied by [54, Pasquale, E.L. & Creta, F., 2017], at moderate Re of 1500. The study showed that the presumed β -PDF (Probability Density Function) shows better agreement to DNS thermodynamic and transport properties, instead of No-model approximation, which neglects the sub-scale variance and is widely used in RANS and LES. It was also shown that the formation and growth of large scale turbulent structures such as Kelvin-Helmholtz vortices was more evident in the case of supercritical jet while, in the case of near-critical injection, the high density gradient damp the growth of such large scale turbulent structures.

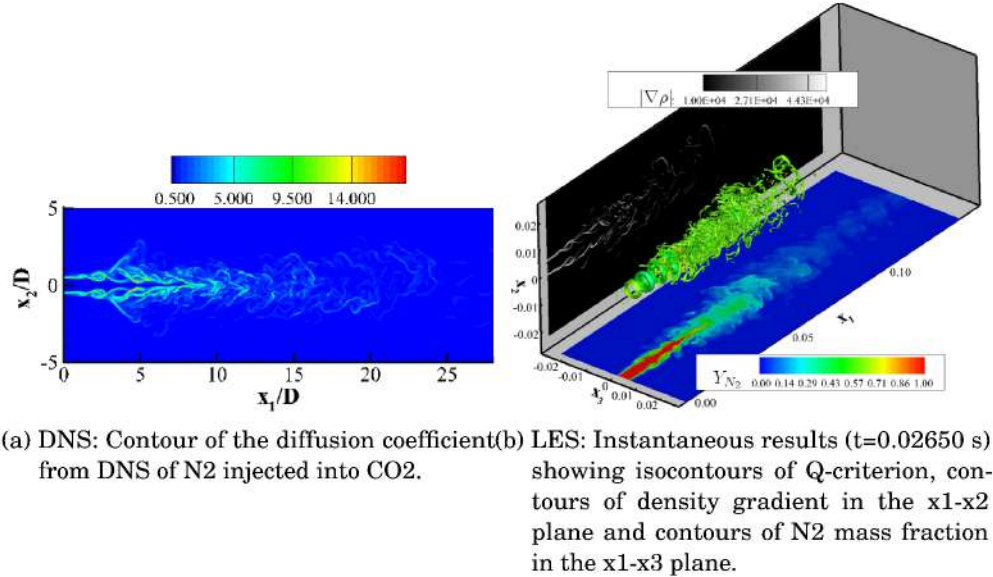
From combustion point of view an experiment investigation of combustion of cryogenic oxygen and methane injected at high pressure is attempted by [71, Singla,G., et al., 2005]. They pointed out that, that under trans-critical conditions the rate of combustion is mainly controlled by turbulent energy transfer to the propellants, which determines the mass fluxes from the dense regions to the lighter gaseous streams governing the rate of conversion into products. Also, at pressures above critical, mixing becomes the slowest and therefore most influential process.

An attempt to understand the fluid behaviour, the mixing process and SGS modelling which fluid subjected to trans-super critical pressure conditions for a non-reacting jet, has been made and discuss in this thesis, which could be simplest one of its kind but sill is physically relevant.

1.10 STATE-OF-THE-ART DNS

DNS along with advanced LES numerical techniques have been a state-of-the art tool for turbulence and combustion research. In addition to it, the supercritical simulation has been even more promising with such approach and it has been vastly exploited by wide spectrum of research group all over the world. One of such group specializing in DNS and turbulence modelling is Josetta Bellan research group at JPL [2, 3, 4, 6, Bellan,J., et al.]. One of their recent study include DNS and LES of a round nitrogen jet entering into a high pressure chamber. First LES is carried out to simulate N_2 injected into CO_2 environment to evaluate the physical model and numerical method and then, DNS is carried out to study the spatial evolution of a supercritical N_2 jet into CO_2 environment (see Figure 12).

The other study of temporal mixing layer under high pressure turbulent condition, to study the reacting multi-species mixing layer [6, Bellan,J. et al., 2017] (see Figure 13). She pointed out that under elevated pressures the reaction rate reaches higher values and occurs in regions of higher density



(a) DNS: Contour of the diffusion coefficient from DNS of N2 injected into CO₂.

(b) LES: Instantaneous results ($t=0.02650$ s) showing isocontours of Q-criterion, contours of density gradient in the x_1-x_2 plane and contours of N2 mass fraction in the x_1-x_3 plane.

Figure 12: DNS of N₂/CO₂ at Re = 1000 and LES of N₂/N₂ jet, carried out by , to study high pressure jet injection and mixing. [6, Bellan,J., et al., 2017]

gradients.

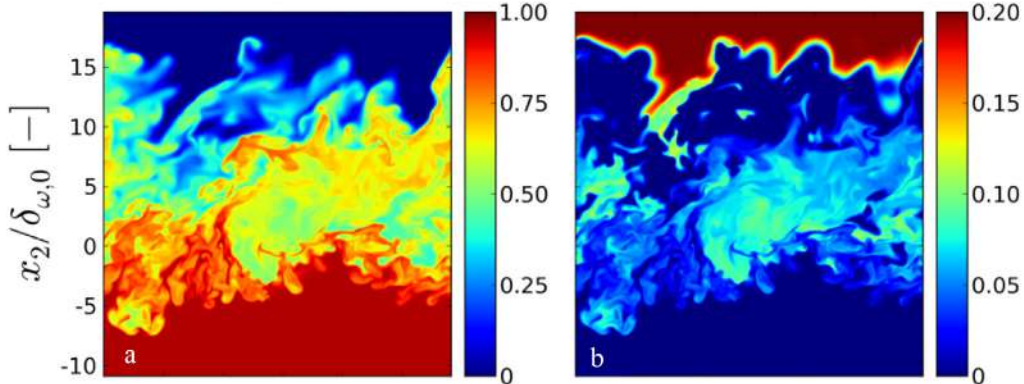
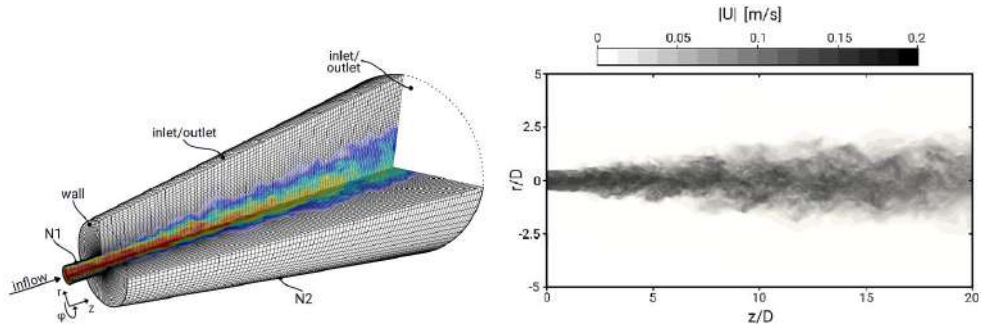


Figure 13: Visualization of mass fraction of (a) C₇H₁₆ and (b) O₂ in DNS of high pressure multispecies temporal mixing layer [6, Bellan,J. et al., 2017].

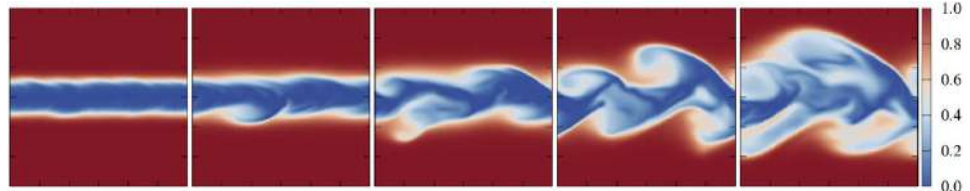
Study focused on the spatial evolving supercritical jet has also been carried out extensively in the field of energy engineering. Such as the research by Ries,F. et al.[66, 67, Ries,F. et al.] at TU Darmstadt. They used DNS of a round jet chilled nitrogen mimicking the experiment by [41, Mayer,W. et al., 2003] but at reduced Reynolds number of 5300 based on the injection diameter. They investigated the flow dynamics, jet disintegration, heat transport phenomena and provided a database for model development and validation (see Figure 14).



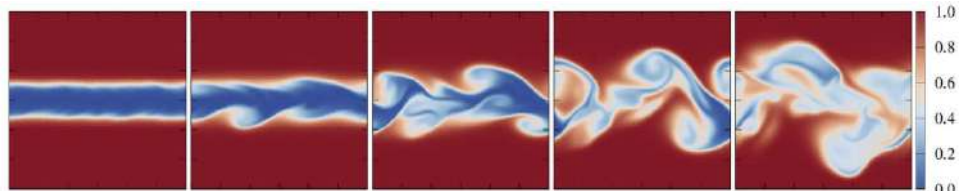
(a) Computational domain and numerical grid of the DNS of nitrogen injection at supercritical condition.
 (b) Snapshots of the velocity magnitude after the injection.

Figure 14: The DNS of chilled nitrogen injection in a round jet fashion into supercritical environment reported by [66, 67, Ries, F. et al.].

The mixing process under transcritical condition with DNS of a temporal jet has been carried out by [54, Lapenna, P.E., & Creta, F., 2017], to investigate SGS modelling of thermodynamic and transport properties for LES. It was shown that the presumed β -pdf is far superior than the extensively used *no-model* approach for thermodynamic and transport properties evaluation (see Figure 15).



(a) Non-dimensionalized enthalpy evolution of the transcritical jet.



(b) Non-dimensionalized enthalpy evolution of the supercritical jet.

Figure 15: The evolution enthalpy of temporal jet at trans- and supercritical conditions, studied by [54, Lapenna, P.E., & Creta, F., 2017].

More realistic situations encountered in the engineering applications with the supercritical fluids consists of combustion processes like those in Liquid Rocket Engines, diesel engines, gas turbine engines etc., but due to limitations of DNS involving high Reynolds number cases, the other close-to with less computational cost such as LES is becoming popular. Thus, many state-of-the art studies of supercritical jet both cold as well as reactive cases are studied with LES approach, which some are discussed in the following

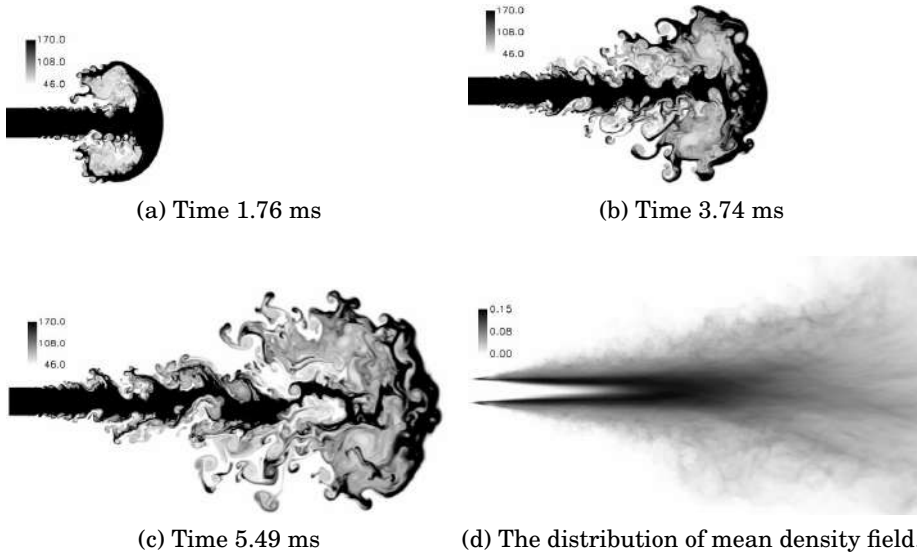


Figure 16: Sequence of unsteady jet evolution in time showing the density field and its unsteadiness and flow entrainments [76, Terashima,H. *et al.*, 2011].

portions.

A high resolution methodology with high-order compact differencing scheme is introduced and studied under supercritical condition by [76, Terashima,H. *et al.*, 2011] see Figures 16 & 17.

Turbulent mixing and combustion of supercritical jets with DNS has been studied by [16, Chong,S.T., *et al.*, 2017], to understand the flame structure at supercritical conditions. DNS of co-flowing $CH_4/O_2/CO_2$ is carried out at 200 bar pressure (see Figure 18).

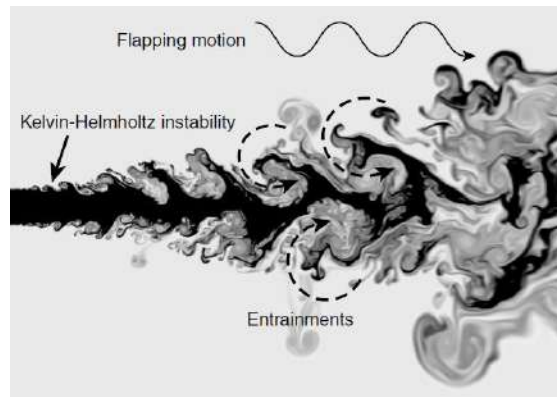


Figure 17: Illustration of unsteady flow structures appearing in supercritical planar jet [76, Terashima,H. *et al.*, 2011].

A research group at Georgia Institute of Technology [83, Wang,X., *et al.*, 2018], studied a high-fidelity modelling and efficient simulation of supercrit-

ical fluid mixing and combustion with LES technique. The study pointed out that the presumed beta-function distribution accurately describes the PDF of the mixture fraction at low mixture fraction variance but deviates at high variance. In addition to it, the computational cost can be drastically reduced using tabulation and correlated dynamic evaluation techniques to evaluate the real-fluid thermodynamic and transport properties, which are computationally expensive in nature (see Figure 19).

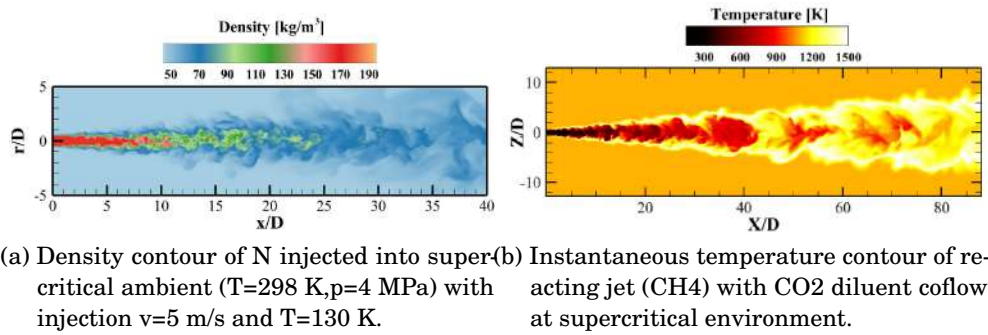


Figure 18: Density and temperature contour of inert and reactive flow obtained with DNS [16, Chong,S.T., *et al.*, 2017].

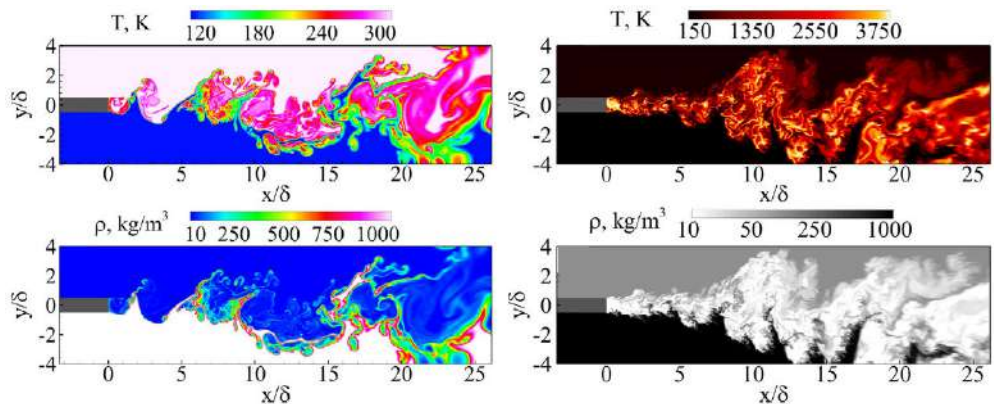


Figure 19: Instantaneous temperature (top-row) and density (bottom-row) distribution for cold flow (left-column) and combustion (right-column) [83, Wang,X., *et al.*, 2018].

1.11 SUMMARY

Summary

- The boiling process below the critical point in phase diagram is isothermal process, where the phase change is accompanied by absorption of heat called the latent heat of vaporization. Which is not true in the supercritical counterpart, as gas-liquid interface vanishes. Supercritical transitions from liquid-like to gas-like require additional energy (apart from the one to overcome intermolecular force of attraction) to increase the temperature. Such energy sink effect reduces with growing pressure and become negligible for $p/p_{cr} > 3$.
- The use of supercritical fluid is favoured in modern engineering applications like Liquid Rocket Engines, gas turbine engines, carbon-free power generation system, refrigerating system etc. due to higher efficiency and compactness. The process of mixing and energy conversion in rocket chamber is completely governed by turbulence.
- The process of jet injection, dissociation, followed by mixing in the case of sub-critical and supercritical injection process are completely different, where atomization is one of the major process involved in sub-critical injection while diffusion and mixing is vital in case of supercritical injection, where liquid propellant don't atomize due to the fact that the surface tension, which hold bounds the liquid surface disappears. Instead, the such fluid undergo a complex liquid-gas like mixing with high diffusivity and is sensitive to temperature and pressure fluctuations.
- Experimental study of fluid flow require huge resources, manpower, and is tedious and time-consuming, while numerical modelling makes it less tedious and time-consuming. However, one cannot replace other but are supplementary to each other. The challenges in the later are mostly due to multi scale and multi physics problem.
- Even in flows where \bar{u} and \bar{p} varies in only 1D or 2D in space, the turbulence fluctuations always have 3D spatial character which are rotational flow structures called the turbulent eddies, which exists in a wide range of length and time scales. These eddies are responsible for mixing in turbulent flow. The fluid particles in far field are brought close together by such eddies causing effective exchange of mass, momentum and heat, and therefore, effective mixing takes place. Such effective mixing process give rise to high value of diffusion coefficient for mass, momentum and heat.

- The turbulent kinetic energy is injected into the system from the mean flow stream into the largest turbulent eddies characterized by comparatively high Reynolds number where the role of viscosity is negligible. But these large eddies are unstable in nature and break up while transferring energy to smaller and smaller eddies. This cascade of energy down to smaller eddies continues until the Reynolds number is small enough for the eddies to be stable and energy gets dissipated into heat by the action of viscosity.
- The large scale motions are characterized by anisotropic nature while the small scales are considered to be locally isotropic. As the Reynolds number increases, the ratio between the large scale and small scale increases, which causes serious limitation when simulating fluid flow with high value of Reynolds number as the computational cost increases very steeply with Re.
- Turbulence and the resulting fluctuating field strongly influence the flow regime. The large fluctuating zones or large eddy motion contribute to strong mixing, while the fluid parcels are being transported by the eddies carrying momentum and energy in and out of the control volume. These momentum exchange as a result of velocity gradient in turbulent flow causes additional shear stresses, known as Reynolds stresses. Similarly, in the presence of the temperature gradient evokes Turbulent heat fluxes, while species gradients evokes Species concentration fluxes.
- The averaged governing equation give raise to the fluctuating terms that are unaccounted in RANS and LES simulation, making the equation unclosed, commonly called Closure problem. It is resolved by modelling the unclosed terms with turbulence and SGS modelling for RANS and LES respectively. While DNS doesn't suffer from this problem, as even the fluctuating terms are resolved during the simulation.
- The highly non-linear behaviour near the critical point makes the ideal gas law unable to relate the thermo-physical states. Therefore, real fluid in elevated temperature and pressure conditions like that in combustion chamber of Liquid Rocket Engine requires additional modelling.
- The formation and growth of large scale turbulent structures such as Kelvin-Helmholtz vortices are more evident in the case of supercritical jet while, in the case of near-critical injection, the high density gradient damp the growth of such large scale turbulent structures.

2 Thermodynamics and modelling of supercritical injection

Outline

It has been discussed briefly in previous chapter that the thermo-physical properties of trans-supercritical fluids are different than ideal and subcritical real fluids. Such fluids demand special treatment while numerically modelling the flow.

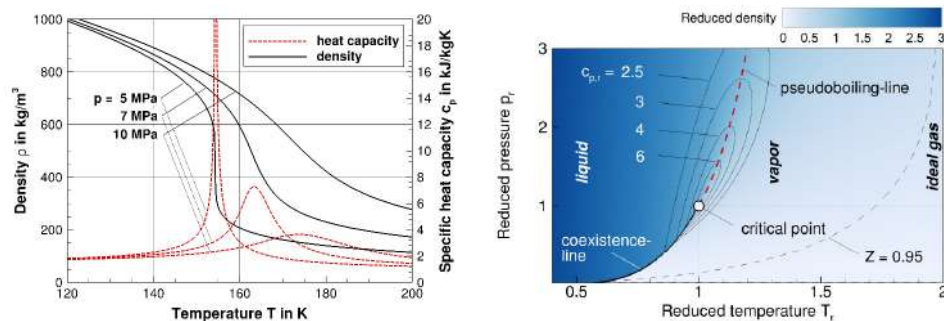
- Section 2.1 reintroduces the concept of Pseudo-boiling, and Widom line, while discussing its effect on thermodynamics of the fluid, and primary thermodynamic models. *What is Pseudo-boiling and Widom line ? How do they influence the fluid behaviour ?*
- Section 2.2 distinguishes some important properties of supercritical and subcritical processes. *Are subcritical fluid injection same as supercritical ? If not, how are they different?*
- Section 2.3 attempts to answer *if the fluids above critical point behave same as and ideal gas ? What state actually a fluid is in at such condition ?*
- Section 2.4 discusses different modern equation of states (EoS) introduced due to incorrect prediction of ideal gas at low temperature and near to the critical point. *Is supercritical fluid an ideal gas ? How is it different? How correctly modern EoS predict the real gas behaviour ? Which EoS better capture near critical behaviour under trans-supercritical injection ?*

An unclear transition from liquid-like behaviour to gas-like behaviour (as discussed preliminary in Chapter 1), occurring at elevated pressure and temperature regime beyond critical point (p_{cr} & T_{cr}) of the element has been under research radar for several decades now, meanwhile, its increasing usefulness in modern engineering applications and planetary sciences (as supercritical fluid state dominate the physical behaviour within the interiors of gas giant planets like Neptune, Saturn and Jupiter [42, McMillan & Stanley, 2010]), has drawn scientific curiosity to understand it even better. However,

the thermodynamics of such state is different from fluids in an ambient condition, therefore, modelling of such case requires a different approach. Even more delicate is near-to the critical case where specific heat at constant pressure theoretically peaks to infinity while the dynamic viscosity is at its minimum value. An attempt to address this critical aspect of supercritical fluid to some extent is behind the scope of this chapter.

2.1 THERMO-PHYSICAL PROPERTIES OF SUPERCRITICAL FLUIDS

The first and mostly quoted statement on fluids under supercritical conditions, is that such fluids are characterized by non-homogeneous nature where two-distinct regions (with gas-like and liquid-like properties) exists. Unlike subcritical phase change, where vaporization is an isothermal phase equilibrium process, supercritical state transition is non-equilibrium process which occurs over finite temperature interval. Supercritical state transition requires energy to overcome intermolecular attraction plus an additional energy to increase the temperature. The process in which the thermal energy so supplied is used to increase the temperature and overcome molecular forces simultaneously, is called *Pseudo-boiling*. A line famously known as *Widom Line* or *Pseudo-boiling line* can be established based on thermodynamic behaviour such as peak of isobaric specific heat, which marks as a transition line between liquid-like behaviour to gas-like behaviour.



(a) Density and isobaric specific heat plotted against temperature for Oxygen ($p_{cr} = 5.043 \text{ MPa}$ and $T_{cr} = 154.60 \text{ K}$, where 5 MPa is sub-critical while 7 and 10 MPa are supercritical pressures. The supercritical transition passing through Widom line in P-T diagram is indicated by peak in C_p and sharp fall of density.)

(b) The fluid state plane showing the diffusive states; low-temperature liquid state which is separated from the high temperature gaseous state separated by co-existence line upto critical point and above it by pseudo-boiling (a.k.a Widom) line.

Figure 20: Thermodynamics illustration (a) & (b) [9, Banuti et al. & Hickey, 2017].

It has also been demonstrated that [75, Tani, H. et al., 2013], in the region near-to pseudo-critical temperature where the C_p peaks to its maximum, Prandtl number exceeds unity and in such case, the smallest scale of turbulence in turbulent mixing layer to be considered is *Batchelor scale* and not the Kolmogorov scale (which is known to be smallest scales in fluid flows). Therefore, pseudo-vaporization process can be considered to have influence on turbulent structures and transport mechanism which it comes to mixing process. In the Figure 20a, at subcritical pressure (5 MPa), during the vaporization process while the heat is constantly supplied to the fluid, density drops sharply as temperature approaches separation temperature where temperature remains constant until all liquid vaporizes and only then the temperature raises. At such point where temperature remains constant even though heat is constantly been supplied, the isobaric specific heat theoretically peaks to infinity. Moving towards supercritical regime, such discontinuity is no longer observed and the C_p peaks begin to reduce and flatten around the temperature of pseudo-boiling.

The investigation of physical behaviour of supercritical fluid has been made and discussed in the literature with inelastic X-ray scattering which measures the dispersion (i.e. dependence of speed of sound on frequency, which is one of the characteristic of liquid and cannot be found on gas). An experiment carried out by Gorelli, Santoro and coworkers in 2006 [27, Gorelli,F., 2006] for oxygen and Santoro and Gorelli in 2008 [68, Santoro,M. et al., 2008] for Argon, to study the properties beyond critical point. They found that, the extended co-existence line (Widom line) separates the p-T phase diagram into liquid-like and gas-like regions, which differ in local structure, very much like the sub-critical behaviours.

2.1.1 *Pseudo-boiling line or Widom line*

Widom line, named in the honor of Benjamin Widom who first proposed fluid density fluctuation near the critical point, is defined as the locus of maximum thermodynamic response functions ¹ like isobaric heat capacity (C_p), isothermal compressibility (K_T), maximum density gradient ($\partial\rho/\partial T)_p$ or minimum thermal diffusivity (α). Plank-Riedel equation give relation of Widom line extension beyond critical point.

$$\ln\left(\frac{p}{p_{cr}}\right) = a + b\frac{T_{cr}}{T} + c \ln\left(\frac{T}{T_{cr}}\right) \quad (47)$$

The values of a , b and c vary with the fluid element. $a = 4.270$, $b = -4.271$ and $c = 1.141$ have been fit to Nitrogen, Oxygen, and Neon fluid data.

¹ Response functions relates the thermodynamic response to a stimulus e.g. C_p relates change in temperature to heat addition, K_T relates change in volume to the change in pressure

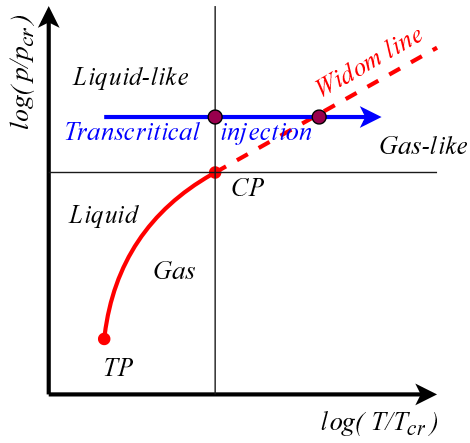


Figure 21: p-T state diagram (log scale) showing the Triple Point (TP), Critical Point (CP), widom line extending to supercritical regime along with transcritical injection which passes through critical and pseudo-boiling temperature.

2.1.2 Pseudo-boiling

During transcritical injection as shown in Figure 21, as fluid passes through Widom line or pseudo-boiling line, it experiences significant increase in specific volume ($1/\rho$) while absorbing large amount of energy to change its temperature, which is also similar to the case of subcritical boiling/vaporization process (with an involvement of latent heat of vaporization). Therefore, the process is termed as *pseudo-boiling* and the corresponding temperature is *pseudo-boiling temperature* (T_{pb}) or *Widom temperature* of a certain pressure. As it has been previously mentioned that, subcritical phase change occurs isothermally while supercritical state transition is not an isothermal process. Therefore, the supplied energy is used elsewhere other than to overcome intermolecular attraction. In particular, the supplied energy is used in two processes: to overcome intermolecular attraction and raise temperature. This can be explained with energy budget.

Enthalpy budget during pseudo-boiling

During the process of pseudo-boiling, the enthalpy associated to overcome intermolecular attraction can be referred to structural ($\Delta h_{structural}$)(following the convention of Banauti [7, Banauti,D.T., 2015]) and the rest of enthalpy associated to raise of temperature is referred to thermal ($\Delta h_{thermal}$). So, the enthalpy difference during the pseudo-boiling process (Δh_{pb}) is such that it includes both the thermal and structural contribution. If we consider a fluid which only raises the temperature upon heating, the energy required to heat such fluid isobarically from T^- to T^+ is $\Delta h_{thermal} = C_{p,liquid}(T^+ - T^-)$.

$$\Delta h_{pb} = \Delta h_{structural} + \Delta h_{thermal} = h(T^+) - h(T^-) = \int_{T^-}^{T^+} C_p(T) dT \quad (48)$$

The effect of pressure on the isobaric heat capacity can be observed in

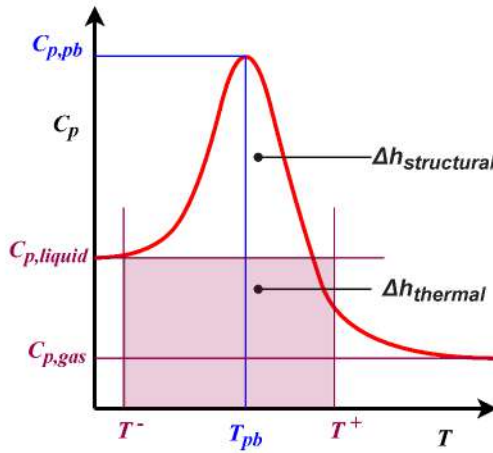


Figure 22: Illustrative representation of isobaric specific heat capacity distribution over finite temperature range where $\Delta h_{structural}$ amount of enthalpy is used to overcome the intermolecular forces (like latent-heat spread over finite range of temperature) while $\Delta h_{thermal}$ is used to raise the temperature from T^- to T^+ by heating the fluid.

Figure 23. The C_p peaks flatten, the distribution widen and move to higher temperature with the increase in temperature. Such peaks coordinates when substituted in the p-T log-log diagram, one obtains a linear line which is same as the one discussed earlier (in Figure 21). Such linear relation can be described as:

$$\frac{p_{pb}}{p_{cr}} = \exp \left[\frac{T_{cr}}{\theta_{cr}} \left(\frac{T_{pb}}{T_{cr}} - 1 \right) \right] \quad (49)$$

$$\frac{T_{cr}}{\theta_{cr}} \approx 0.55 \quad (50)$$

Figure 24 shows evolution of enthalpy with temperature for Oxygen (whose T_{cr} and p_{cr} are 154.6 K and 5.043 MPa respectively). The difference between the subcritical and supercritical behaviour can be observed in the same figure. The change of enthalpy in supercritical liquid-like to gas-like is smooth occurring through wide range of temperature while, it is discontinuous and isothermal in subcritical counterpart.

In the vicinity of low temperature (see Figure 24), all isobars converge towards same liquid enthalpy asymptote ($h_L(T)$), while on the other hand, all isobars converge towards same ideal gas asymptote ($h_G(T)$) at higher temperature. It is also important to notice that both the asymptotes are pressure independent. This shows that regardless of path followed (different isobaric enthalpy paths with different pressure values), the energy associated with the transition from liquid like to gas-like or liquid to gas in the case of supercritical and subcritical cases respectively is energetically identical. The fundamental difference between the two is that the iso-thermal vaporization is subcritical condition is replaced by non-equilibrium non-isothermal process in supercritical condition.

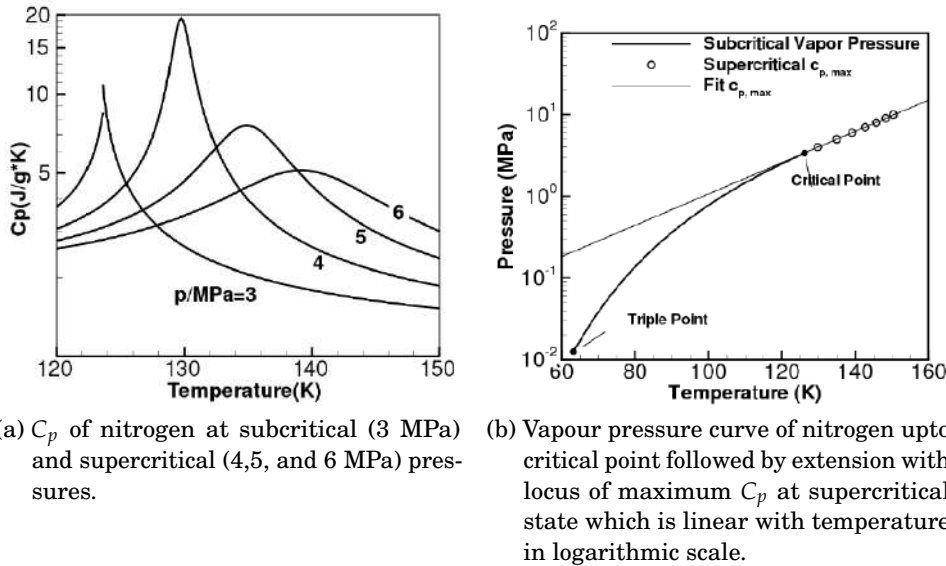


Figure 23: (a) The pressure dependants of isobaric specific heat for nitrogen. & (b) Position of maximum isobaric specific heat relative to coexistence line for nitrogen. [8, Banuti, D.T., 2015].

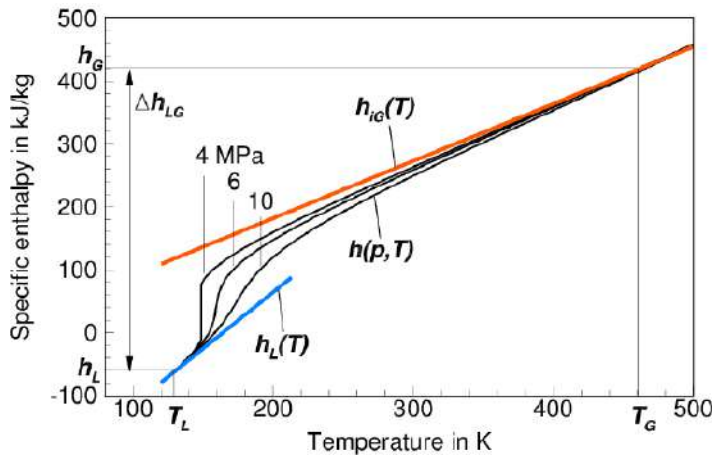


Figure 24: Specific enthalpy versus temperature profiles for three different pressures (one subcritical and two supercritical cases), for oxygen. Each curves are isobaric. The asymptotes are enthalpy for ideal gas and liquid [9, Banauti,D.T., 2017].

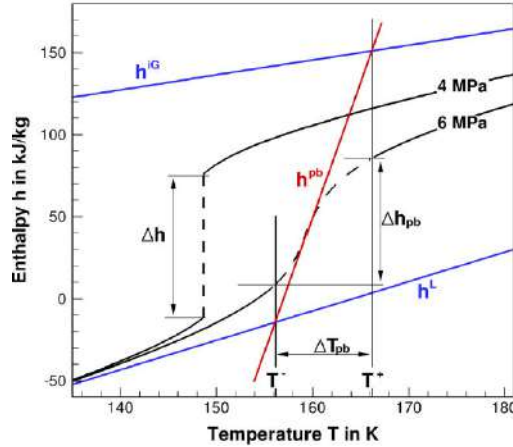
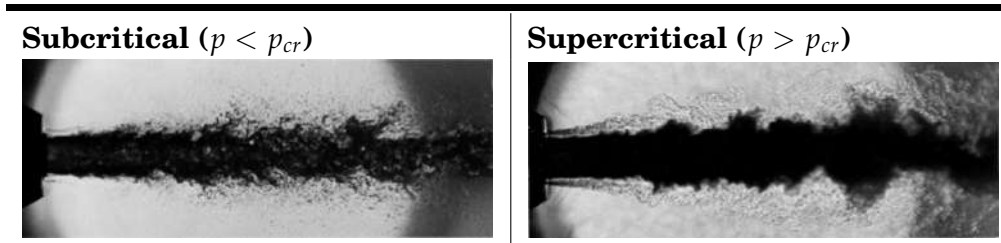


Figure 25: C_p evolution with temperature of Oxygen at subcritical (4 MPa) and supercritical (6 MPa) pressures along with the phase transition enthalpy Δh_{pb} at an interval of temperature ΔT . The enthalpy asymptotes are ideal gas h^{IG} and liquid reference state h^L [9, Banauti,D.T., 2017].

2.2 SUBCRITICAL VERSUS SUPERCRITICAL INJECTION



Thermodynamics

There exists sharp distinction between liquid and gas phase.	Such phase difference is not so distinctive where fluid properties change gradually but continuously as pressure is elevated above the critical point. Drastic change in fluid properties such as ρ is observed near critical point.
There exists iso-thermal vaporization with the latent heat vaporization.	The vaporization process is continuous non-equilibrium non-isothermal process and occurs over finite range of temperature.
During transition, supplied thermal energy is use to overcome intermolecular force without raising temperature.	The energy supplied is use to overcome molecular forces and increase temperature simultaneously.

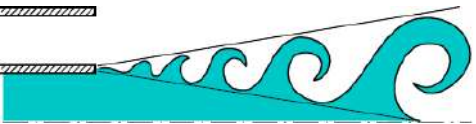
There exists surface tension to distinguish liquid from gas phase.	The effect of surface tension on fluid vanishes.
Fluid behaviour can be explained with Lagrangian droplet representation	Continuous Eulerian mixing model is required to explain the fluid behaviour at supercritical regime.
Injection process	
 <ul style="list-style-type: none"> • Fuel injection • Primary jet disintegration due to surface tension break up • Ligaments are formed, instabilities grow and are detached from the jet surface • Atomization • Droplets evaporate 	 <ul style="list-style-type: none"> • Fuel injection • Stringy-thread like structure develop and grow • they rapidly dissolve and fade away
The process involves atomization jet break up with sharp interface	The process involves diffusion and mixing with no surface tension

Table 11: Thermo-physical difference between fluid under supercritical and subcritical conditions.

2.3 REAL VERSUS IDEAL GAS

Figure 26 shows density profile under sub- and supercritical pressures. Where we can see that the towards low temperature, the density profiles converge towards liquid state (with high values of density), which is typically considered incompressible i.e. differences between the isobar density profiles are significantly small. While on the other hand, for higher temperatures, the profiles converge towards the ideal gas behaviour.

The supercritical state consists of both liquid and gaseous phase but not a different completely new state of fluid.

2.4 MODELLING EQUATION-OF-STATE (EOS) OF REAL FLUIDS

The thermodynamic properties of the fluid (such as ρ , p , T etc.) have to be related in some way as they are part of a same fluid, if such relation exists, knowing the value of one or couple of them, help to determine the rest, so that the computation cost and complexity is reduced. Simple models such as constant density can be handy for incompressible flows i.e. low Mach number gaseous flows or liquids. This simple approximation simplifies the numerical computation effort as the energy equation is decoupled from momentum and

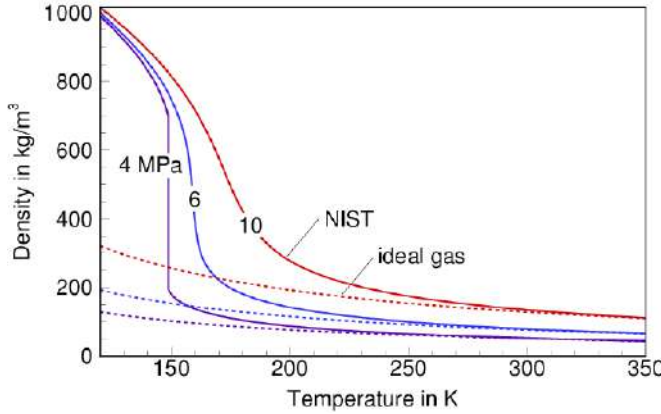


Figure 26: Density evolution of oxygen ($T_{cr} = 154.6$ K, $P_{cr} = 5.048$ MPa) with temperature at sub and supercritical pressure values. The real fluid approaches incompressible liquid at low temperatures while on the other hand, ideal gas at high temperatures. The solid-line are obtained with NIST database while the dashed-line follow the idea equation state [9, Raju,M. et al., 2017].

species transport equation and can be solved independently. The value of p can be computed with Poisson equation.

In the contrary, for incompressible flow condition, where density is no more a constant parameter and flow involves shocks or expansion fans, an ideal gas behaviour assumption is adapted. Even though, the interaction of molecules in microscopic level is neglected in ideal gas assumption, it encompasses most of the physics in the flow. However, this might not be true in the low temperature regime as discussed in section 2.3 (see Figure 26). At low temperature real fluid have different behaviour than ideal counterpart because of the fact that the neglected inter molecular effects become important in such case.

2.4.1 Ideal gas EoS and real gas effect

The most simplified relation among T , p and ρ is the ideal gas equation of state.

$$p = \rho RT \quad (51)$$

Where, R is the specific gas constant formed (which is ratio between universal gas constant \mathbb{R} and molecular weight M_W). Variable density assumption couples all the transport equations and thus, T , p and ρ fields are related. As discussed previously, intermolecular forces and molecular dynamics neglected at low temperature and high pressure regime leads to failure of Ideal gas EOS, such differences between ideal and real behaviour can be computed with a *real gas factor* or *Compressibility factor* Z , reformulated from Equation 51. Z can be defined as a ratio of real fluid pressure to the

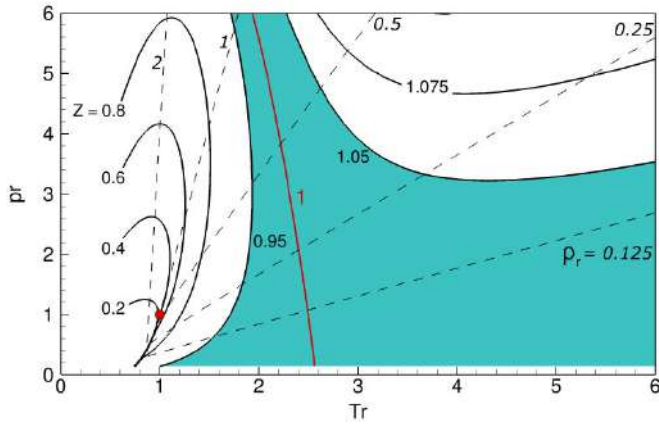


Figure 27: Pressure ratio ($p_r = p/p_{cr}$) versus Temperature ratio ($T_r = T/T_{cr}$) for Nitrogen, showing Z (with solid-line) and isochors (dashed-lines). The maroon line represent ideal gas ($z = 1$) and shaded region show ideal gas behaviour with 5% deviation [9, Raju,M. et al., 2017]. The red dot marks the critical point of nitrogen.

pressure an ideal gas at identical ρ , p and T would exert. For an ideal gas $Z = 1$.

$$Z = \frac{p}{\rho RT} \quad (52)$$

Sometimes, it is also interpreted as a measure of molecular interaction. Some important hypotheses for ideal gas EOS formulation are no chemical or mechanical intercations between molecules are considered, particles are regarded as point masses and the gas is calorically perfect with constant heat capacities. But, most importantly later assumption cannot be true for supercritical fluids.

It can be seen from Figure 27 that, for elevated pressure ($p_r > 3$) and temperature ($T_r > 3$), the ideal gas behaviour is not applicable and results to large errors. As discussed by Raju, M. , Hickey, J.P. & et al.[9], at $p_r = 0.3$, the error in pressure computed by using ideal gas EOS for equilibrium vapor is 20% ($Z = 0.8$) and at $p_r = 0.8$ the error reaches to 40% ($Z = 0.6$).

It can also be observed in Figure 27 and has been reported in literature that, the supercritical fluid may be characterized as an ideal gas for $T > 2T_{cr}$ and $p < 3p_{cr}$. In and around the critical point, the intermolecular forces play an important plus non-linearities introduced by the pseudo-boiling during transcritical conditions alter the idea relationship detected by ideal EOS, therefore demand for a better EOS, such an initial attempt had been taken in literature by Van der Wall in 1873 famously known as *Van der Waals equation*, who attempted to connect the fundamental state of the molecular forces to ideal gas law.

2.4.2 Real gas EOS

Van der Waals' EoS

The ideal gas EOS is modified with two contributions to the pressure i.e. repulsion pressure $p_{repulsion}$ and attraction pressure $p_{attraction}$. This concept is used in the formulation of equations of van der Waals' (1873), Redlich and Kwong (1949) and Soave (1972). The van der Waals' [80, van der Waal, 1873] formulation is

$$p = \underbrace{\frac{RT}{v-b}}_{p_{repulsion}} - \underbrace{\frac{a}{v^2}}_{p_{attraction}} \quad (53)$$

Where v is molar volume, a and b are constants. Constant b is volume of molecule which is considered as a hard sphere while the other constant a gives the measure of the intermolecular attraction force. This cubic form of equation in terms of specific volume is also known as *cubic EOS*. Waals' EoS has formed a basis for many higher-order EoS. Note that, in van der Waals' EOSm the constant b is treated temperature independent.

Redlich-Kwong EoS

Redlich and Kwong [65, Redlich & Kwong, 1949] worked on van der Waals' EoS in particularly on the attraction pressure term, they modified constant $a = f(T)$ (a is now a function of Temperature) and the denominator term as;

$$p = \frac{RT}{v-b} - \frac{f(T)}{v(v+b)} \quad (54)$$

$$\text{where, } \begin{aligned} f(T) &= \frac{a}{\sqrt{T}} \\ b &= \frac{(2^{1/3} - 1)RT_{cr}}{3p_{cr}} \end{aligned}$$

Soave-Redlich-Kwong EoS

Soave-Redlich-Kwong (famously known as SRK EoS) is very popular among chemical engineering, where concept of acentric factor ω introduced by Pitzer in 1955 which accounted for the non spherical nature of molecules, was introduced into the RK EoS in 1972 by Soave [72, Soave,G., 1972] and therefore termed as SRK EoS. The modifications to RK EoS in SRK EoS is $a = f(T, \omega)$ i.e.

$$a(T, \omega) = \frac{1}{9(2^{1/3} - 1)} \frac{RT_{cr}^2}{p_{cr}} \left[1 + m(1 - \sqrt{T_r}) \right]^2 \quad (55)$$

$$\text{where, } \begin{aligned} m &= 0.480 + 1.574\omega - 0.176\omega^2 \\ \omega &= -\log \left(1 + \frac{p_{sat}}{p_{cr}} \right)_{T_r=0.7} \end{aligned}$$

Peng-Robinson EoS

Peng and Robinson [59, Peng & Robinson, 1976] proposed a way to further modify the van der Waal's EOS to enhance the accuracy of density prediction and match the compressibility factor Z especially near to the critical point. D. Peng was a PhD student of Prof. D.B. Robinson at the University of Alberta (Canada). PR EOS is considered to be simple and most popular in natural gas industry and somewhat suited to gas/condensate systems.

$$p = \frac{RT}{v - b} - \frac{f(T)}{v^2 + 2bv - b^2} \quad (56)$$

$$f(T) = 0.457236 \frac{(RT_{cr})^2}{p_{cr}} \left[1 + m(1 - \sqrt{T_r}) \right]^2$$

where, $m = 0.3746 + 1.5422\omega - 0.26992\omega^2$

$$b = 0.077796 \frac{RT_{cr}}{p_{cr}}$$

It has been pointed out in the literature that, for low densities, all EoS are acceptably accurate while, only PR and SRK EoS can be used for higher densities.

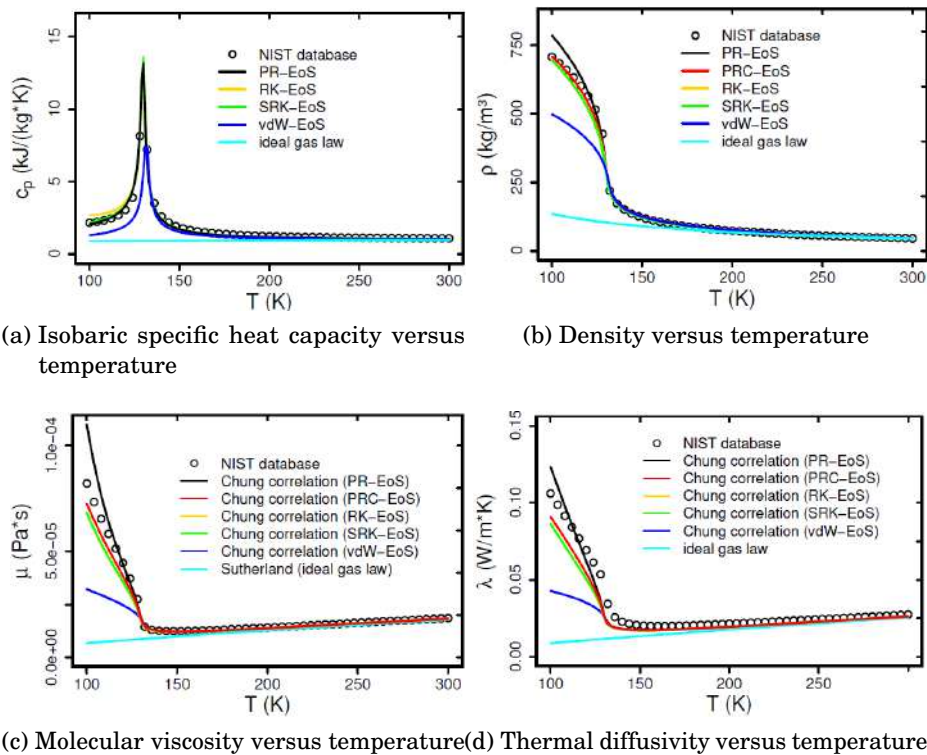


Figure 28: Thermodynamic parameters against temperature for Nitrogen at pressure 3.98 MPa (where $T_{cr} = 126.19$ and $p_{cr} = 3.3958$), computed with discussed EoS: PR (Peng-Robinson), PRC (Corrected Peng-Robinson), RK(Redlich-Kwong), SRK (Soave-Redlich-Kwong) and vdW (van der Walls).

The predictability and accuracy of above discussed EoSs for the critical injection of nitrogen has been demonstrated by [66, Ries,F. *et al.*, 2017], which are shown in Figure 28. If we closely observe the density profile and comparison with different EoSs, RK, PRC and SRK, EoS seems to adapt well with the NIST database while PR and vdW EoS as well as the ideal gas law are very much offset thus, they give poor predictions at low temperatures. Isobaric heat capacity predictions are in good agreement with the database except for vdW and ideal gas law. We can therefore, draw a conclusion that, PR, RK, and SRK-EoS are capable of capturing non-ideal behaviour of supercritical fluid close to the critical temperature (i.e. the C_p peak) while the ideal gas law and vdW-EoS are unable to do so very well. This is also true in the case of molecular viscosity and thermal diffusivity, that ideal gas law and vdW are not best candidate, especially at low temperature regime. The properties evaluated in Figure 28d and 28c are referred to the correlations of [18, Chung, Y.M. *et al.*, 1988].

2.5 SUMMARY

Summary

- The process in which the thermal energy so supplied is used to increase the temperature and overcome molecular forces simultaneously, is called Pseudo-boiling. A line famously known as Widom Line or Pseudo-boiling line can be established based on thermodynamic behaviour such as peak of isobaric specific heat, which marks as a transition line between liquid-like behaviour to gas-like behaviour. The C_p peaks flatten, the distribution widen and move to higher temperature with the increase in temperature.
- Regardless of path followed (different isobaric enthalpy paths with different pressure values), the energy associated with the transition from liquid like to gas-like or liquid to gas in the case of supercritical and subcritical cases respectively is energetically identical. The fundamental difference between the two is that the isothermal vaporization is subcritical condition is replaced by non-equilibrium non-isothermal process in supercritical condition.

- Near-to pseudo-critical temperature where the C_p peaks to its maximum, Prandtl number exceeds unity and in such case, the smallest scale of turbulence in turbulent mixing layer to be considered is Batchelor scale and not the Kolmogorov scale (which is known to be smallest scales in fluid flows). Therefore, pseudo-vaporization process can be considered to have influence on turbulent structures and transport mechanism which it comes to mixing process.
- At low temperature real fluid have different behaviour than ideal counterpart due to the fact that the neglected inter molecular forces and molecular dynamics become important in such regime. In the ideal gas EoS formulation, assumptions such as on chemical or mechanical interactions between molecules, particles with point masses and the gas is considered calorically perfect with constant heat capacity. But, later assumption cannot be true for supercritical fluids. In fact, around the critical point, the intermolecular forces play an important plus non-linearities introduced by the pseudo-boiling during transcritical conditions violet the assumptions made by ideal EOS, therefore demand for a better EOS. Eos such as PR, RK and SRK-EoS are capable of capturing non-ideal behaviour of supercritical fluid close to the critical temperature.
- for elevated pressure ($p_r > 3$) and temperature ($T_r > 3$), the ideal gas behaviour is not applicable and results to large errors. The supercritical fluid may be characterized as an ideal gas for $T > 2T_{cr}$ and $p < 3p_{cr}$.

Part II
NUMERICAL TREATMENT

3 Theoretical Framework for DNS

Outline

- Section 3.1 introduces to approach for the study of trans- super-critical mixing with some literature survey on the same.
- Section ?? talks about *Temporally evolving jet*, an approach employed to study the jet evolution (in time), the other approach being Spatially evolving.
- Section 3.2 discusses the Equation of State (EoS) for nitrogen, used in the DNS, which has to be very accurate to incorporate the smallest possible thermodynamic properties within the equation.
- Section 3.3 introduces to the Spectral Element Method and why it is preferred over other classical Finite Element Method, to solve PDEs of the governing equations.
- Section 3.5 discusses the need for low-mach-number assumption and its simplifications to the simulation.
- Section 3.6 briefly discusses the boundary condition imposed to obtain the solution of the governing equation and its relevance to our simulation condition.
- Section 3.7 gives overview of the governing equation for compressible, multi-species and reactive flow boiling down to our case of compressible, single-species and non-reactive flow, followed by filtering of the equation to obtain the LES equation.
- Section 3.8 explains the DNS configuration and database employed for the temporally evolving transcritical planer jet Direct Numerical Simulation including the computational domain, initial conditions, simulation dimensions, and the thermodynamic regime of the simulation.

3.1 INTRODUCTION

As it has been previously mentioned in the introductory chapters that, modern engineering and industrial devices such as liquid propellant rocket engines, nuclear power generation systems, especial refrigerating systems, gas turbine engines etc. exploit or fluids used in such equipments undergo a condition where pressure and temperature of the ambient is larger than their critical value, therefore, fluids at such elevated thermodynamics state termed as supercritical fluids, have different thermo-physical behaviour unlike subcritical and ideal fluids. The main reason to exploit such regime of fluid is due to compactness and increase in efficiency. In particular, we are interested combustion process like in the case of liquid propellant rocket engines, where liquid fuel (such as liquid hydrogen) when injected into the combustion chamber it undergoes transcritical injection process (previously discussed), thereafter, the mixing and combustion takes place.

Several studies like the one by [71, Singla, G. *et al.*, 2005] were they injected cryogenic-liquid Methane (possible rocket fuel) and liquid oxygen (classical rocket oxidizer) into high pressure combustion chamber (between 4 to 6 MPa). Note that the critical temperature and pressure of oxygen are 154.6 K and 5.043MPa respectively, while for methane are 190.56 K and 4.592 MPa respectively. The results suggested that, *under transcritical condition, the rate of combustion is mainly controlled by turbulent energy transfer to the propellant, which determines the mass fluxes from the dense regions to the lighter gaseous streams governing the rate of conversion into products... transcritical fluids behave like a gas but with highly nonuniform distribution of density*. This shows that, the combustion process in supercritical regime is very much influenced by the process of turbulent mixing.

Furthermore for trans- supercritical fluid mixing, the process of pseudo-vaporization is expected to have influence on the turbulence structures and transport mechanism (of mass, momentum and heat) in the turbulent mixing phenomenon, as pointed out by [75, Tani, H. *et al.*, 2012]. Several other studies carried out by [31, Hosangadi *et al.*, 2012] (LES & RANS of LN-GN coaxial jets under transcritical conditions), [87, Zong *et al.*, 2007] (LES of LN jet under transcritical condition), and [12, Branam *et al.*, 2001] (high pressure injection test with N-O coaxial injector), all drew common conclusion that, the pseudo-vaporization process has in influence on the mixing of trans-supercritical jets. It has been pointed out by [3, Bellan,J., *et al.*, 2000] that, there are lack of models which incorporates necessary informations for supercritical fluid, suggesting to firstly investigate simpler geometric configurations, such as mixing layers, particularly temporal mixing layers as they are considered simple in computation, while such study provide vital informations on density stratification, real gas effects and scalar transport. Such detail informations on thermodynamics and mixing parameters are only acquired with the help of DNS simulation. Such approach can also

be important to verify, correct, and/or reformulate new turbulent LES and RANS models applicable trans- supercritical fluid simulations.

The DNS of temporally evolving transcritical nitrogen planar jet at relatively low Reynolds number has been carried out by Dr. Pasquale E. Lapenna and Prof. Dr. Francesco Creta from La Sapienza University of Rome (Department of Mechanical and Aerospace Engineering) with the support of the Italian Super-Computing Inter-university Consortium CINECA for high-performance computing resources under the Iscra B Grant DNS-LS. Four of such transcritical nitrogen jets characterized by same Re but four different pressures (ranging from near-to-critical upto supercritical) values are simulated, to have a deeper understanding of mixing process and their dependencies on various pressures.

3.2 REFERENCE NITROGEN EOS

The simulation presented in this thesis is of an inert fluid (nitrogen). Nitrogen has been one of the most popular reference fluids both for experimental as well as computational simulations. In order for the simulation to generate correct results, it is vital to have correct and accurate relation for the fundamental equation of state. Since nitrogen is one of the element which is extensively used both in experimental as well as numerical simulation of fluids, it posses largest volume of data sets. The first short description of EoS for nitrogen was published by Span *et al.* in 1998. Lots of new data sets for the same has been reported ever since and therefore, a new EoS for nitrogen was published by [81, Wagner, W., Span, R., *et al.*, 2001], comparing all data including the newest available measurements.

So improvised EoS is considered to have minimized the number of coefficients with reduction in the Helmholtz energy and is considered to represent available data within their uncertainty. The range of validity of EoS for nitrogen if from freezing line to 1000 K at pressures to 2200 MPa. It has been compared with the experimental data upto 1800 K. Some important vapour-liquid and solid-liquid coexistence properties values reported on the nitrogen EoS [81, Wagner, W., Span, R., *et al.*, 2001] are mentioned in the subsections below.

3.2.1 *Solid-liquid and vapour-liquid co-existence properties*

Critical Point

The critical pressure value is usually not measured by is directly extrapolated from the measured vapour pressures to the assumed critical temperature. It has been mentioned (by [81, Wagner, W., Span, R., *et al.*, 2001]) that, the critical density also cannot be determined directly because of infinite compressibility at the critical point but saturated densities can be extrapolated

upto the critical point. The critical temperature is reported to be determined with the critical density from fitting power laws to saturated liquid and vapour densities.

$$\frac{\rho}{\rho_c} = N_1 \left(1 - \frac{T}{T_c}\right) \pm N_2 \left(1 - \frac{T}{T_c}\right)^\beta \quad (57)$$

where, ρ_c , T_c , N_1 , and β were determined from a nonlinear fit to coexisting densities. The reported critical values are:

Critical Temperature	T_c	126.192 ± 0.010 K
Critical Pressure	p_c	3.3958 ± 0.0017 MPa
Critical Density	ρ_c	313.3 ± 0.04 kg/m ²

Table 12: The critical values of nitrogen reported by [47, Nowak,P. *et al.*, 1997] and adopted for EoS by[81, Wagner, W., Span, R., *et al.*, 2001].

Triple Point

The results published by Pavese *et al.*(1984) were considered the most accurate where the triple point temperature measurements range from 63.1502 K to 63.1508 K, which agree well with [47, Nowak,P. *et al.*, 1997] and so was also adopted by [81, Wagner, W., Span, R., *et al.*, 2001], which are reported below;

Triple-point Temperature	T_{tp}	63.151 ± 0.003 K
Triple-point Pressure	p_{tp}	12.523 ± 0.010 kPa

Table 13: The triple-point values of nitrogen reported by [47, Nowak,P. *et al.*, 1997] and adopted for EoS by [81, Wagner, W., Span, R., *et al.*, 2001].

3.2.2 EoS for nitrogen

Helmholtz energy is considered as the fundamental property for the derivation of the equation of state for nitrogen by Wagner *et al.*with independent variables of density and temperature i.e.;

$$a(\rho, T) = a^0(\rho, T) + a^r(\rho, T) \quad (58)$$

where a is the Helmholtz energy, $a^0(\rho, T)$ is the contribution of ideal gas to Helmholtz energy and $a^r(\rho, T)$ is the residual Helmholtz energy due to intermolecular forces. All thermodynamic properties such as pressure can be computed as derivatives of the Helmholtz energy;

$$p = \rho^2 \left(\frac{\partial a}{\partial \rho} \right)_T \quad (59)$$

The new equation of state for nitrogen (by [81, Wagner, W., Span, R., *et al.*, 2001]) is formulated as;

$$\frac{a(\rho, T)}{RT} = \alpha(\delta, T) = \alpha^0(\delta, \tau) + \alpha^r(\delta, \tau) \quad (60)$$

where α is the dimensionless Helmholtz energy, $\delta = \rho / \rho_{cr}$, and $\tau = T / T_{cr}$ are the reduced density, and the reduced temperature respectively. The values of critical density ρ_{cr} and critical temperature T_{cr} are 313.3 kg/m³ and 126.192 K respectively.

3.2.3 Ideal gas behaviour

In order to correctly mimic the ideal behaviour of nitrogen, the ideal gas formulation of the Helmholtz energy is given by;

$$a^0 = h^0 - RT - Ts^0 \quad (61)$$

where the ideal gas enthalpy h^0 is

$$h^0 = h_0^0 + \int_{T_0}^T C_p^0 dT \quad (62)$$

and the ideal gas entropy s^0 is

$$s^0 = s_0^0 + \int_{T_0}^T \frac{C_p^0 dT}{T} - R \ln \left(\frac{\rho T}{\rho_0 T_0} \right) \quad (63)$$

	h_0^0	8670	J/mol
where,	T_0	298.15	K
	s_0^0	191.5	J/(molK)
	p_0	0.101325	MPa

Note that, h_0^0 is the value enthalpy at absolute zero-temperature T_0 , s_0^0 is the value of entropy at T_0 and p_0 [19, Cox,J.D. *et al.*, 1989].

Plugging in Equations 62 and 63 in Equation 61, we get;

$$a^0 = h_0^0 + \int_{T_0}^T C_p^0 dT - RT - T \left[s_0^0 + \int_{T_0}^T \frac{C_p^0 dT}{T} - R \ln \left(\frac{\rho T}{\rho_0 T_0} \right) \right] \quad (64)$$

which can be expressed in terms of reduced variables as;

$$\alpha^0 = \frac{h_0^0 \tau}{RT_{cr}} - \frac{s_0^0}{R} - 1 + \ln \frac{\delta \tau_0}{\delta_0 \tau} - \frac{\tau}{R} \int_{\tau_0}^{\tau} \frac{C_p^0 d\tau}{\tau^2} + \frac{1}{R} \int_{\tau_0}^{\tau} \frac{C_p^0 d\tau}{\tau} \quad (65)$$

where, $\delta_0 = \rho_0 / \rho_{cr}$, $\tau_0 = T_{cr} / T_0$, and ρ_0 is the ideal gas density at $T_0 = 298.15$ K and $p_0 = 0.101325$ MPa.

The ideal heat capacity (C_p^0) must be known to high accuracy because errors in the ideal gas heat capacity directly affect the accuracy of caloric

properties calculated from the equation of state. Specifically, errors in C_p^0 will cause errors in the real fluid values of isochoric and isobaric heat capacity, internal energy, enthalpy, entropy and the speed of sound [81, Wagner, W., Span, R., *et al.*, 2001]. The empirical relation of ideal heat capacity developed and discussed by [81, Wagner, W., Span, R., *et al.*, 2001], based on previous models and experimental data which is predicted compute C_p^0 accurately within about 0.01% in the temperature range between 20 and 5000 K is expressed as;

$$\frac{C_p^0}{R} = a_0 + a_1 T + a_2 T^2 + a_3 T^3 + a_4 \left(\frac{u^2 \exp(u)}{[\exp(u) - 1]^2} \right) \quad (66)$$

where the ideal gas constant $R = 8.314510 \text{ J/(molK)}$, $a_0 = 3.5$, $a_1 = 3.066469 \times 10^{-6}$, $a_2 = 3.701240 \times 10^{-9}$, $a_3 = -3.987984 \times 10^{-13}$, $a_4 = 1.012941$ and $u = 3364.011 \text{ K/T}$.

3.3 SPECTRAL METHOD (SM)

The numerical treatment along the spatial direction in DNS require accurate representations of derivatives, especially at the smallest scales (or large wavenumbers). Spectral methods (introduced by [51, Orszag & Patterson, 1972]) exploits Fourier series in the spatial (periodic) direction and Chebyshev polynomial expansions in direction with solid walls [37, Malasekera W. & Versteeg H. K.], can be used for accurate computation of derivatives. They are class of discretization and solution procedures for PDEs in which the approximate solution to the problem is expanded in a global high order Fourier or polynomial series [78, Timmermans,L.J.P., *et al.*, 1990]. Spectral methods are economical and have high convergence rates, but are difficult to apply in complex geometry with arbitrarily nonuniform grids . On the other hand, finite-difference methods usually underestimate derivatives of a given velocity field, causing inaccuracies in the smallest (dissipating) scales [82, Wilcox,D.C., 2006].

3.3.1 SM versus FEM

Before proceeding to the brief introduction to Spectral Element Method (SEM-used in DNS of supercritical study in the thesis), it is also important to understand some main differences between the Spectral Method (SM) and Finite Element Method (FEM), which ultimately led to SEM. For more detail study on SM, and SEM, the reader is referred to a short descriptive report by[78, Timmermans,L.J.P., *et al.*, 1990].

SM used high order infinitely differentiable basis-functions (mainly Chebyshev or Legendre polynomials) and is global basis, defined over the whole domain of interest while, FEM use low order basisfunctions which are local in nature. As a consequence, convergence of PDEs by SM is obtained by increasing the order of the spectral expansion while, this is achieved by increasing

the number of elements in FEM. The other important consequence is that, the SM has a property of exponential accuracy while, FEM can achieve at most algebraic convergence.

The element division and possibility of local mesh refining in the FEM makes sure that they are perfectly suited to deal with complex geometries with complex physical phenomena such as strong discontinuities of the solution, which is not true in SM.

Therefore, SM are perfect for problems with highly regular data/solutions with simple domain while, in the case of strong discontinuities and/or complex geometries FEM are far more easier to implement.

3.4 SPECTRAL ELEMENT METHOD (SEM)

An improvised version of Spectral Method, a high order weighted residual techniques for PDEs was introduced by [50, Orszag & Patterson, 1984], combining the geometric flexibility of the FEM with the good convergence properties of the Spectral Method, making it suitable for applications of complex problems in complex geometries, called Spectral Element Method (SEM), a highly parallel domain decomposition technique [32, Kerkemeier, S. G., 2010]. In this method, the discretization domain is divided into spectral elements, and the dependent and independent variables are approximated by high order polynomial expansions within the individual domains. Convergence of the approximate solution to the exact solution of the PDE is obtained similar to SM, by increasing the order of the approximation while fixing the number of elements. Such element division with high order interpolation ensures accurate approximations even in the case with complex geometries and rapid function variations. Thus SEM handles both geometric and physical complexity.

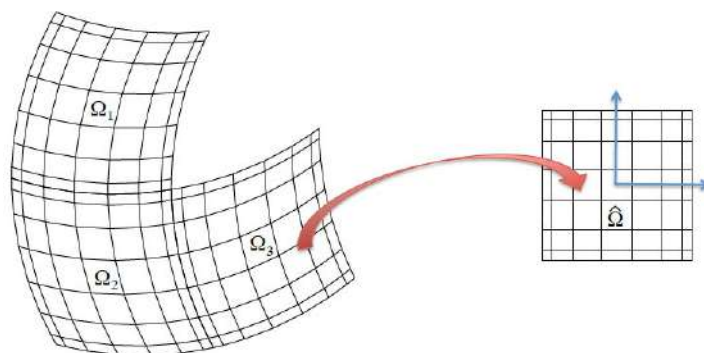


Figure 29: Spectral element mapping from canonical 7th-order quadrilateral domain $\hat{\Omega}$ to physical sub-domain Ω_e [32, Kerkemeier, S. G., 2010].

The [24, nek5000] employs high-order numerical technique based on the SEM together with reference nitrogen EoS, in the present work on DNS of trans-supercritical mixing, allows enough resolution to capture the small-scale eddies interactions in turbulence and non-linearities caused by pseudo-boiling process. In order to have accurate study of the multi-scale problems like turbulent reactive flows require the propagation of small scale features with minimal dissipation over many characteristic length scales [34, Lamioni, R., 2016]. The SEM discretizes the computational domain into rectangular elements in which the numerical solution is approximated on Gauss-Lobatto-Legendre quadrature points by an Nth-order Lagrange polynomial.

3.5 NEED FOR LOW-MACH-NUMBER ASSUMPTION

The other important consideration in the present DNS simulation is the *Low mach number assumption*, which avoids numerical complications by considering constant thermodynamic pressure. Otherwise, the compressible solver encounter issues like pressure oscillations due to transcritical conditions and filter out the acoustic pressure waves. The low mach number consideration, retains the mechanical equilibrium of pressure across the pseudo-boiling region [55, Lapenna,P.E. & Creta,F., 2019] by imposing constant thermodynamic pressure, and thus the real fluid properties can be acquired by tabulating the values from *NIST-Refprop* software [35, (NIST) Lemmon,E.W., *et al.*, 2013] for that one pressure. This is known to increase the accuracy compared to widely used cubic EoS as pointed out by [55, Lapenna,P.E. & Creta,F., 2019], [10, Banauti,D.T., *et al.*, 2016].

The first advantage of low-mach number assumption in compressible code is that, it allows to filter out the acoustic wave propagation from the governing equation, therefore allows effective integration of equations while taking account of the density variation [53, Lapenna,P.E., 2016]. Two important issues encountered while simulating mixing and combustion under transcritical conditions employing compressible CFD codes, pointed out by [56, Lapenna,P.E. *et al.*, 2018] are time step restrictions because of the elevated speed of sound in liquid-like phase with relatively low injection speed and generation of pressure oscillations causing stability issues.

3.6 BOUNDARY CONDITIONS

The primary difficulty with boundary conditions in any Navier-Stokes computation is at open boundaries because of the elliptic nature of the problem where the flow at such boundaries depend on the unknown flow outside computational domain. In LES and DNS, this issue is overcome by imposing periodic boundary conditions for directions in which flow is statistically homogeneous (such as, stream-wise and span-wise direction in our planar jet simulation) [82, Wilcox,D.C., 2006]. In addition to it, such periodic or

homogeneous spatial direction allows to obtain statistics by averaging over the homogeneous direction.

3.7 GOVERNING EQUATION

The Navier-Stokes equation in a dimensional compact form for compressible, multi-species and reactive flow can be written as: Conservation of mass:

$$\frac{\partial \rho}{\partial t} + \nabla \cdot (\rho u) = 0 \quad (67)$$

Conservation of momentum:

$$\frac{\partial \rho u}{\partial t} + \nabla \cdot (\rho uu) = \nabla \cdot \sigma + \rho \mathfrak{F} \quad (68)$$

Conservation of energy:

$$\frac{\partial \rho e}{\partial t} + \nabla \cdot (\rho uh) = \sigma : \nabla u - \nabla \cdot q_e \quad (69)$$

Conservation of species:

$$\frac{\partial \rho Y_k}{\partial t} = \nabla \cdot (\rho u) = \nabla \cdot (\rho J_k) + \dot{\omega}_k \quad (70)$$

where,

ρ	= mixture density
u	= velocity of fluid
λ	= thermal conductivity
e	= specific internal energy
h	= specific enthalpy
Y_k	= mass fraction of k^{th} species
$q_e = q_q + h_k J_k$	= energy flux (vector)
q_q	= heat flux (vector)
$h_k J_k$	= enthalpy flux (vector) of species diffusion
J_k	= diffusive flux (vector)
$\dot{\omega}_k$	= reaction rate
\mathfrak{F}	= body-forces
$\rho \mathfrak{F} = 0$	= if no body-forces
$\sigma = -pI + 2\mu S$	= stress tensor
μ	= dynamic viscosity
S	= viscous stress tensor $(S = [\nabla u + \nabla u^T - 2/3(\nabla \cdot u)I]/2)$

In the above governing relations (67, 68, 69 and 70), further simplifications can be made for our DNS of transcristial flow study. With the following assumptions;

- Low-mach number limit

Introducing asymptotic expansion for a generic variable f in terms of mach number

$$f(x, t) = f_0(x, t) + f_2(x, t)\hat{M}^2 + \mathcal{O}(\hat{M}^4) \quad (71)$$

Such expansion is employed to the above relations (67, 68, 69 and 70), and under low mach limit, the terms with \hat{M}^2 or higher can be dropped because their contributions are considerably as small compared to the leading order terms denoted by \square_0 . Note that $\hat{M} = u_0/a_0$ is the non-dimensional mach number.

- Single-species

Which allows to drop equation 70 in the simulation.

- Non-reacting flow

Eases the energy balance equation by removing the reaction rate term from the equation 69.

- No-body forces, bulk viscosity and thermal radiation

The computation is free from the external forces such as gravitational forces, so that $\rho\mathfrak{F} = 0$.

The governing equation simplifies to;

Continuity equation:

$$\frac{\partial \rho}{\partial t} + \nabla \cdot (\rho u) = 0 \quad (72)$$

Conservation of momentum:

$$\rho \left(\frac{\partial u}{\partial t} + u \cdot \nabla u \right) = -\nabla p_1 + \nabla \cdot (\mu S) \quad (73)$$

where the viscous stress tensor S is expressed as;

$$S = \nabla u + (\nabla u)^T - \frac{2}{3}(\nabla \cdot u)I \quad (74)$$

Here $\nabla p_0 = 0$ i.e. the zeroth order pressure, known as *thermodynamic* or *background pressure*, is temporally and spatially homogeneous. Note that, the thermodynamic pressure is homogeneous as well as constant in time since we are considering an open domain. This simplification (as discussed previously in Section 3.5) allows an efficient tabulation of EoS and thermodynamic and transport properties as a function of T, allowing us to use detailed real fluid models at a reasonable cost [57, Lapenna,P.E., 2018]. While, the second order ($\mathcal{O}(\hat{M}^2)$) pressure term p_1 known as *hydrodynamic pressure* appears in zeroth order momentum equation 73.

And the conservation of energy (in terms of specific enthalpy) is expressed as :

$$\rho \left(\frac{\partial h}{\partial t} + u \cdot \nabla h \right) = \nabla \cdot (\lambda \nabla T) \quad (75)$$

The velocity divergence constraint (Equation 75) and EoS ($\rho(h, p_0)$) can be used to replace the continuity equation (Equation 72), as;

$$\nabla \cdot u = -\frac{1}{\rho} \left(\frac{\partial \rho}{\partial t} + u \cdot \nabla \rho \right) \quad (76)$$

$$= -\frac{1}{\rho} \left(\frac{\partial \rho}{\partial h} \right)_{p_0} \left(\frac{\partial h}{\partial t} + u \cdot \nabla h \right) \quad (77)$$

The thermodynamic derivative of density at constant pressure $\left(\frac{\partial \rho}{\partial h} \right)_{p_0}$ is dependent on the EoS [57, Lapenna,P.E., 2018]. As one can notice in the above governing relations, the thermodynamic and transport properties are function of only enthalpy h (or equivalently on temperature T since, $h = C_p \Delta T$) and the thermodynamic pressure p_0 is only a parameter [55, Lapenna,P.E. & Creta,F., 2019] i.e.

$$\left(\frac{\partial \rho}{\partial h} \right)_{p_0} (h; p_0)$$

$$\rho (h; p_0)$$

$$C_p (h; p_0)$$

$$\lambda (h; p_0)$$

$$\mu (h; p_0)$$

These quantities utilized in the simulation of transcritcal jet are computed and tabulated within the simulation via NIST (National Institute for Standards and Technology) *NIST-Refprop* software [35, (NIST) Lemmon,E.W., *et al.*, 2013], which exploits the reference nitrogen EoS developed by [81, Wagner, W., Span, R., *et al.*, 2001] and accurate transport properties (such as viscosity μ and thermal conductivity λ) developed by [36, Lemmon,E. & Jacobsen,R., 2004].

The governing equations are then numerically integrated with an open-source, massively parallel EoS independent low mach number version code *NEK5000* [24] based on SEM [55, Lapenna,P.E. & Creta,F., 2019], [57, Lapenna,P.E., 2018], as discussed earlier in sections 3.4 and 3.5 .

3.7.1 *Filtered (LES) equation*

With the introduction of Reynolds and Favre averaging techniques in the first chapter (refer: 1.7 - 1.7), the previously discussed governing equations can be averaged to obtain LES or RANS equation where only the mean field are of interest making computation of real world problems possible. However, such averaging procedure encounter closure issue thus require models to close to problem. In the flow with density change (like that in our transcritcal simulation, where the high stratification of density is encountered), Favre averaging of the governing equation can be carried out, and are termed

RANS or LES equation.

After carrying out favre-averaging on Equations 72, 73 and 75, so obtained the favre-averaged mass (continuity), momentum and energy (in terms of specific enthalpy) equation are;

$$\frac{\partial \bar{\rho}}{\partial t} + \nabla \cdot (\bar{\rho} \tilde{u}) = 0 \quad (78)$$

$$\frac{\partial \bar{\rho} \tilde{u}}{\partial t} + \nabla \cdot (\bar{\rho} \tilde{u} \tilde{u}) = -\nabla \bar{p}_1 + \nabla \cdot (\bar{\mu} \tilde{S}) - \nabla \cdot (\widetilde{\bar{\rho} u'' u''}) \quad (79)$$

$$\frac{\partial \bar{\rho} \tilde{h}}{\partial t} + \nabla \cdot (\bar{\rho} \tilde{u} \tilde{h}) = \nabla \cdot (\bar{\lambda} \nabla \tilde{T}) - \nabla \cdot (\widetilde{\bar{\rho} u'' h''}) \quad (80)$$

The unclosed terms in the above equation 78 and 79 i.e. $\nabla \cdot (\widetilde{\bar{\rho} u'' u''})$ and $\nabla \cdot (\widetilde{\bar{\rho} u'' h''})$ have to be modelled by some turbulence modelling or SGS modelling and close the unknown quantities.

The unclosed term in the LES-momentum equation can be written as:

$$\widetilde{\bar{\rho} u'' u''} = \bar{\rho} \bar{u} \bar{u} - \bar{\rho} \tilde{u} \tilde{u} \quad (81)$$

where the convective flux is given by;

$$\bar{u} \bar{u} = \bar{u} \bar{u} + \mathcal{L} + \mathcal{C} + \mathcal{R} \quad (82)$$

where the tensors \mathcal{L} , \mathcal{C} and \mathcal{R} are:

$$\text{Leonard stress} \quad \mathcal{L} = \widetilde{\bar{u} \bar{u}} - \widetilde{\bar{u} \bar{u}}$$

$$\text{Cross-term stress} \quad \mathcal{C} = \widetilde{\bar{u} u''} + \widetilde{\bar{u} u''}$$

$$\text{SGS Reynolds stress} \quad \mathcal{R} = \widetilde{u'' u''}$$

The popular modelling of the Reynolds stress and the turbulent heat flux employed in turbulent modelling employed by most of the RANS and LES CFD codes is based on *Boussinesq Hypothesis*. Where, the Reynolds stress $\widetilde{\bar{\rho} u'' u''}$ is considered proportional to viscous tensor $\bar{\tau}$. While, the turbulent heat flux $\widetilde{\bar{\rho} u'' h''}$ is modelled proportional to the temperature (or enthalpy) gradient.

$$\widetilde{\bar{\rho} u'' u''} \cong \mu_T \bar{\tau} \quad (83)$$

$$\widetilde{\bar{\rho} u'' h''} \cong \rho \nabla \tilde{h} \frac{\mu_T}{Pr_T} \quad (84)$$

where, the turbulent dynamic viscosity μ_T is modelled through popular $K - \epsilon$ or $K - \omega$ as $\mu_T = \bar{\rho} C_\mu \frac{k^2}{\epsilon}$. Where, k is the turbulent kinetic energy and ϵ is it's dissipation rate and Pr_T is the turbulent Prandtl number.

It should be noted that for the simulation presented in this thesis work, the homogeneous directions are X- and Z- directions, i.e., the averaging

process (both Reynolds $\bar{\square}$ and/or Favre $\tilde{\square}$) can be carried out only along X-direction (stream-wise) and Z-direction (span-wise). On the other hand, the non-homegeneous directions are Y-direction and time, thus, the averaged quantities will *only* be function of y or/and time.

3.8 DNS DATABASE

The DNS configuration of temporally evolving transcritical planar jet consists of dense-cold (chilled) nitrogen injected (transcritically) into a light-warm nitrogen which is in supercritical state. The injected cold jet temperature is below the pseudo-boiling temperature T_{pb} i.e. $T_{jet} < T_{pb}$, while the warm nitrogen ambient temperature is above the pseudo-boiling temperature i.e. $T_{env} > T_{pb}$. Therefore, the process of mixing with pseudo-vaporization process takes place in the supercritical environment, while the injection is trans-critical. Note that, the term *transcritical* refers to state of fluid where its temperature is below the pseudo-boiling temperature while, pressure of the fluid is above pseudo-boiling pressure i.e. $T < T_{pb}$ & $p > p_{pb}$. On the other hand, *supercritical* state is when both the temperature and pressure of the fluid is above the pseudo-boiling temperature and pressure i.e. $T > T_{pb}$ & $p > p_{pb}$. Similarly, the *transcritical injection* is when the fluid in transcritical state is injected into the supercritical environment.

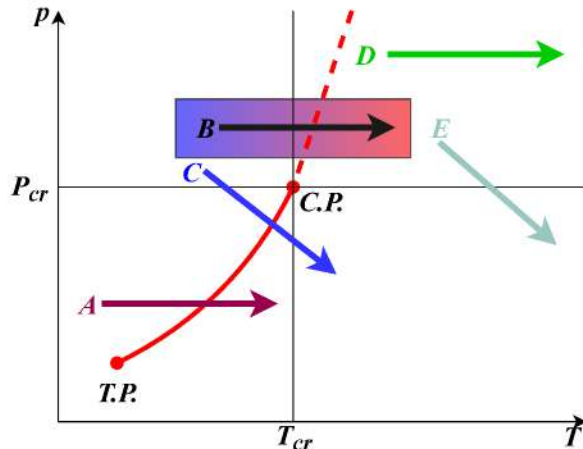


Figure 30: Illustration of different injection processes: A) Sub-critical injection B) Trans-critical injection C) Near-critical injection D) Super-critical injection and E) High-pressure-ratio expansion. B) Trans-critical injection process is studied in the present work. The dashed-line represent the Widom line.

It should be noted that, the simulation the present work is carried out at three different pressures i.e. three (isobar) transcritical injections (unlike only one transcritical injection shown in Figure 30), to study the influence of pressure on the mixing and pseudo-vaporization process. The schematic representation with the configuration of the DNS is shown in Figure ??.

3.8.1 DNS computational domain

The computational domain of the simulation is periodic in X-direction (stream-wise direction) and Z-direction (span-wise direction). These directions are homogeneous i.e. averaging can be carried out along these directions (stream-wise and span-wise). Open boundaries, imposed as zero-Neumann boundary conditions for all variables, are imposed in the cross-wise direction (Y-direction), making sure that p_0 , the thermodynamic pressure remains constant in time [55, Lapenna,P.E. & Creta,F., 2019].

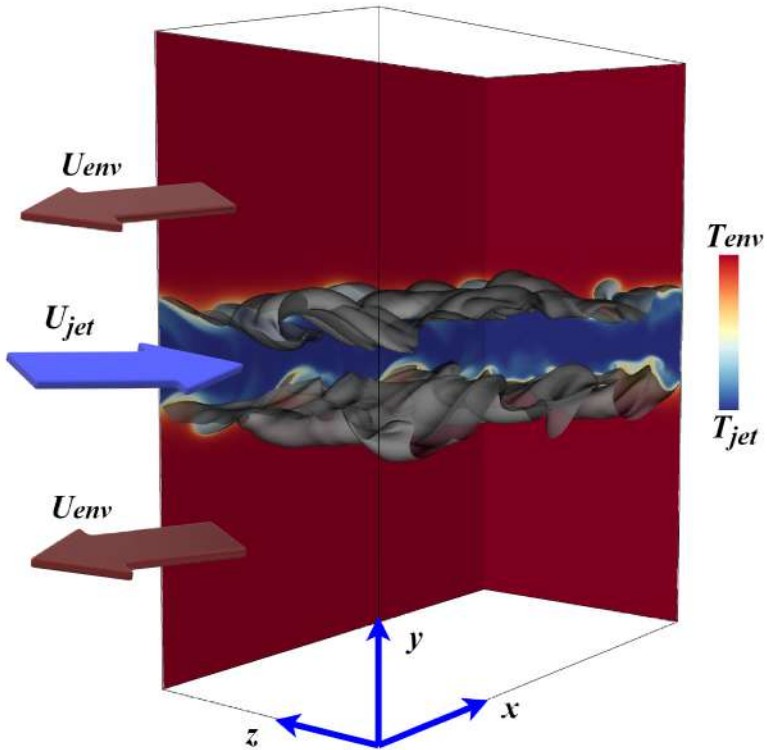


Figure 31: DNS configuration showing the computational domain of the temporal-planar transcritical jet. T_{jet} is the (cold) temperature of the injection jet while, T_{env} is the temperature of the (warm) supercritical nitrogen environment and U_{jet} is the initial mean shear. [55, 57, Lapenna,P.E. & Creta,F., 2019,2018]

The physical dimension of the domain (see Figure 33) is verified to be large enough to obtain the converged statistics along with smoothness of the spectra [55, Lapenna,P.E. & Creta,F., 2019].

3.8.2 Initial conditions

The initial velocity conditions such as the initial Reynolds number of the jet $Re_{jet} = \frac{\Delta U H}{\nu_{ref}} = 3000$, where $\Delta U = U_{jet} - U_{env}$ is the initial mean shear, ν_{ref} is the reference kinematic viscosity which is selected as the minimum

value encountered in the initial condition, which is located in the proximity of the pseudo-boiling region (see Table). The 3D velocity field is initialized with a mean field with a superimposed homogeneous and isotropic synthetic turbulence disturbance, generated using random Fourier modes with prescribed probability distributions of the components following [21, Davidson,L. & Billson,M., 2006]. The perturbations so generated are added to the main velocity field to trigger the shear instabilities between the cold and warm streams.

$$u(x,y,z) = U(y) + u'(x,y,z)\mathcal{F}_{\mathcal{N}}(y) \quad (85)$$

$\mathcal{F}_{\mathcal{N}}(y)$ is a filter isolating disturbances only to the jet core and mixing layers. The chosen values of u_{RMS} and the integral length scale of the disturbance are;

Velocity fluctuation: $u_{RMS} = 0.005\Delta U$

Integral length scale: $l_0 = H/3$

The input parameters, which are used to characterize the modified von Karman spectrum and for the synthetic turbulence generation are root mean squared (RMS) velocity u_{RMS} and an integral length l_0 .

The kinetic energy spectrum $E(k)$ is given as;

$$E(k) = \alpha \frac{u_{RMS}^2}{k_e} \frac{(k/k_e)^4}{[1 + (k/k_e)^2]^{17/6}} \exp(-2(k/k_\eta)^2) \quad (86)$$

k	=	wave number
k_η	=	$\epsilon^{(1/4)} v_{ref}^{-3/4}$ highest wave number
ϵ	=	dissipation rate (per unit mass)
where, k_e	=	$\frac{9\alpha\pi}{55l_0}$ most energetic wave number
α	=	1.453 a constant
k_1	=	k_e/p smallest wave number
p	=	H/l_0 a constant

The initial profiles of the mean velocity field U , non-dimensional enthalpy ξ and the disturbance filter $\mathcal{F}_{\mathcal{N}}(y)$ in Y-direction is chosen as ;

$$\mathcal{F}_{\mathcal{N}}(y) = \frac{1}{2} - \frac{1}{2} \tanh\left(\frac{H_N - 2|y|}{\delta_N}\right) \quad (87)$$

$$U(y) = \mathcal{F}_U + \frac{\Delta U}{2} \left(\frac{2}{1 + \sqrt{\rho_{jet}/\rho_{env}}} - 1 \right) \quad (88)$$

$$\mathcal{F}_U = \frac{\Delta U}{2} \left(\tanh\left(\frac{H_U - 2|y|}{\delta_U}\right) \right) \quad (89)$$

$$T(y) = T_{jet} + \frac{(T_{env} - T_{jet})}{2} + \left[1 + \tanh\left(\frac{H_\xi - 2|y|}{\delta_\xi}\right) \right] \quad (90)$$

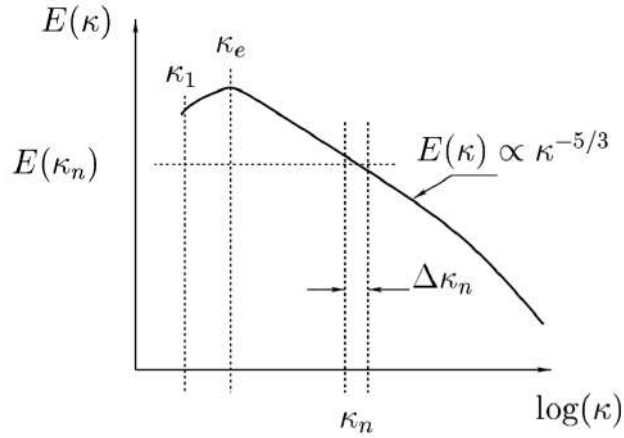


Figure 32: Modified von Karman spectrum (wave number k versus kinetic energy E) used to trigger initial turbulence disturbance of velocity component [53, Lapenna,P.E., 2016].

H_U	=	$H_N = H$	initial jet width
H_ξ	=	$H_U + \delta_\xi - \delta_U$	
	=	$1.1H$	initial cross-wise cold core thickness
where,	δ_u	= $0.2H$	thickness of velocity profile
	δ_N	= $0.25H$	thickness of disturbance profile
	δ_ξ	= $0.3H$	thickness of non-dimensional enthalpy profile

3.8.3 Simulation regimes

The transcritical DNS simulation of nitrogen are carried out at four different pressures, featuring same Reynolds number of jet $Re_{jet} = 3000$ at initial temperature $T_{jet} = 100$ K injected into the warm nitrogen supercritical environment at $T_{env} = 300$ K. The four pressure values are named as $P1$, $P2$, $P3$ and $P4$, while the Reynolds number as $R2$ (which is constant), therefore, the four simulation cases with above pressures and reynolds number, are termed as $R2P1$, $R2P2$, $R2P3$ and $R2P4$ respectively. The size of the computational domain can be seen in Figure 33. And, the thermophysical quantities and definitions used in the simulation are tabulated in the Table ch3-table-computational domain.

The study of the injection process at three different pressure levels allows us to understand the influence of pressure on the mixing of fluid along with the pseudo-vaporization process. The stratification of thermodynamic properties like density and the near critical enhancement of properties are very significant near to the critical point (i.e. R2P1 case in our simulation), which such issue is less pronounced as the reduced pressure increases and eventually vanishes for larger reduced pressure values (≥ 3) [7, Banauti,D.T.,

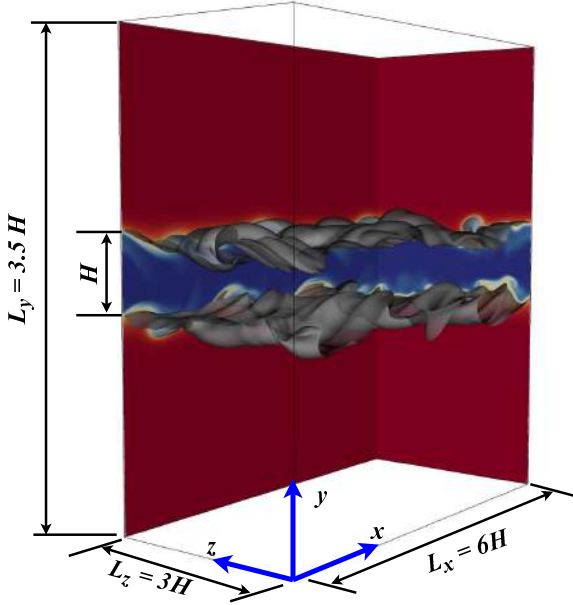


Figure 33: The computational domain with dimensions where, $H = 2$ mm is the initial jet width, L_x , L_z and L_y are the length, width and height of the domain stretching in stream-wise, span-wise and cross-wise directions respectively.

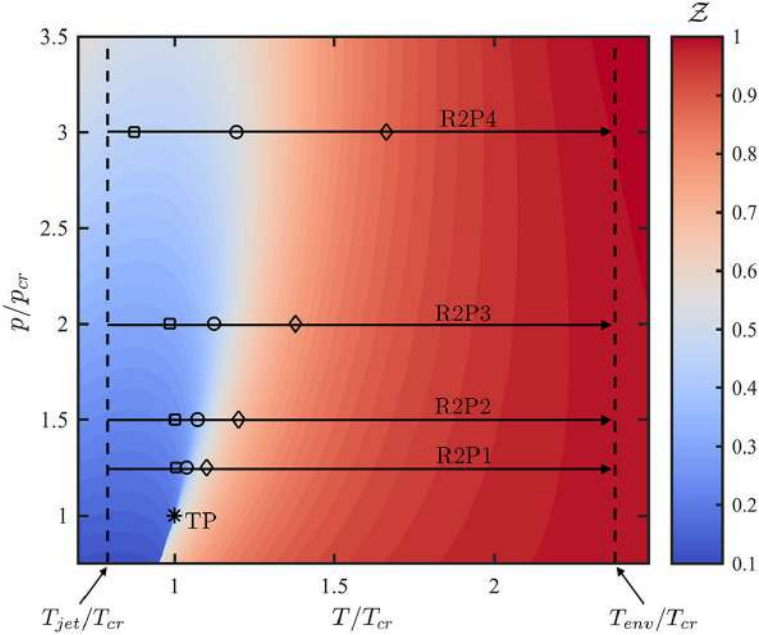


Figure 34: Non-dimensionalized pressure-temperature plot with superimposed compressibility factor Z , showing four isobaric simulations carried out in the present work. The symbols \square , \circ and \diamond on each isobaric transcrittical injection line represent T^- , T_{pb} and T^+ temperatures while * shows critical-point. [55, Lapenna,P.E. & Creta,F., 2019]

et al.2015]. Moreover, due to high stratification of thermodynamic properties near to the critical point, special attention during the simulation is require,

	Notation[Unit]	R2P1	R2P2	R2P3	R2P4
Reduced pressure	p_0/p_{cr}	1.25	1.5	2.0	3.0
Density ratio	ρ_{jet}/ρ_{env}	14.82	12.42	9.43	6.45
Initial mean shear	$\Delta U_{jet} [m/s]$	0.089	0.091	0.093	0.098
Ref. viscosity [m/s^2]	$\nu_{ref} (\times 10^{-8})$	5.95	6.05	6.22	6.50
Max. Prandtl No.	Pr_{max}	5.74	3.47	2.28	1.67
SEM grid	$EN^3 (\times 10^6)$	291	139	72	46
Reynolds number	Re_{jet}	3000	3000	3000	3000
Jet temperature	$T_{jet} [K]$	100	100	100	100
Env. temperature	$T_{env} [K]$	300	300	300	300
Grid dimension	Δ_E	0.060H	0.077H	0.097H	0.111H

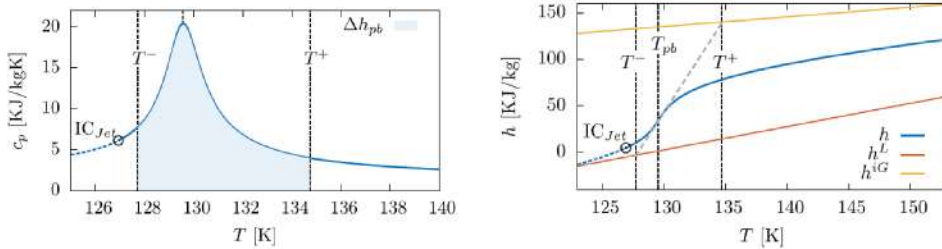
Table 14: Primary computational parameters of transcritical temporal jets at four different pressure levels. $H = 2$ mm is the jet width [55, Lapenna,P.E. & Creta,F., 2019].

also the need for very fine grid size is needed to capture the finest details in such regime, as can be seen in the Table 14.

Similarly, four cases for each reduced pressure ratio are studies which represents four time instances reported in the present work as non-dimensional time instances $t^* = t/t_{jet}$, where the reference time t_{jet} is the jet time unit given as $t_{jet} = t/(H\Delta U)$. Such study of the mixing with various time instances help us understand the temporal evolution of the jet in particular the turbulence mixing which incur at the later time instances. It would have been the best case scenario if data at all simulate time instances were stored for the analysis, but this was not possible due to restriction in data storage. However, some parameters and important studies like DNS resolution assessment and variance study (which are discussed in later chapters) was carried out during *on-the-fly*, i.e. computation carried out in parallel to the simulation without interrupting the run.

Figure: 34 shows the reduced pressure and the reduced temperature boundaries within which the simulation is carried out. As mentioned previously, the transcritical injection simulation are carried out at four different pressure levels shown by the four isobaric lines in the figure, where the temperature of the jet and warm environment are shown by the vertical lines to the left and right of the figure, respectively. Note, that the jet and environment temperature for all four simulation are same.

Thermophysically speaking, the isobaric transition from the liquid-like phase of transcritical jet to the supercritical phase takes place in non-isothermal way. The energy input is used to overcome the intermolecular



(a) The specific enthalpy variation with temperature for nitrogen h^L and h^{iG} are the variations for liquid and ideal gas states, which acts as an asymptotes. The shaded area represents the Δh_{pb} .

(b) The isobaric heat capacity profile with temperature as it undergoes the pseudo-boiling process.

Figure 35: (a) and (b) profiles are for N at $p_0/p_{cr} = 1.17$ which is close to R2P1 case (1.25) with $T^+ = 134.74$ K and $T^- = 127.73$ K. \circ represents the jet initial condition for the DNS reported by [55, 57, Lapenna,P.E. & Creta,F., 2019,2018].

force of attraction along with heating the fluid. These two contributions are referred to as structural and thermal respectively. This has been discussed in detail in Chapter 2 Section 2.1.2. Therefore, the total amount of specific enthalpy during the pseudo-boiling process is given as

$$\Delta h_{pb} = \int_{T^-}^{T^+} C_p(T) dT = \Delta h_{structural} + \Delta h_{thermal} = h(T^+) - h(T^-) \quad (91)$$

Where, T^+ and T^- corresponds to the temperature of a gas-like state and liquid-like state respectively. If the $h^{iG}(T)$, $h^L(T)$ and $h^{pb}(T)$ are defined in the following ways ([7, Banauti,D.T, et al.2015]);

$$h^{iG}(T) = C_{p,ideal} T$$

$$h^L(T) = C_{p,Liquid} T + h_{0,Liquid}$$

$$h^{pb}(T) = C_{p,pb}(T - T_{pb}) + h_{0,pb}$$

Then, one can define the gas-like state temperature T^+ and the liquid-like state temperature T^- [57, Lapenna,P.E. & Creta,F., 2018] as;

$$T^- = \frac{h_{0,Liquid} - h_{0,pb} + C_{p,pb}T_{pb}}{C_{p,pb} - C_{p,Liquid}} \quad (92)$$

$$T^+ = \frac{h_{0,pb} - C_{p,pb}T_{pb}}{C_{p,iGas} - C_{p,pb}} \quad (93)$$

3.9 SUMMARY

Summary

- Spectral methods exploits Fourier series in the spatial (periodic) direction and Chebyshev polynomial expansions in direction with solid walls, can be used for accurate computation of derivatives. Spectral methods are economical and have high convergence rates, but are difficult to apply in complex geometry with arbitrarily non-uniform grids.
- Spectral Element Method (SEM) technique, used in the present work, combines the geometric flexibility of the FEM with the good convergence properties of the Spectral Method, making it suitable for applications of complex problems in complex geometries. In this method, the discretization domain is divided into spectral elements, and the dependent and independent variables are approximated by high order polynomial expansions within the individual domains.
- The employed high-order numerical technique based on the SEM together with reference nitrogen EoS and accurate thermodynamic-transport properties, in the present work on DNS of trans-supercritical mixing, allows enough resolution to capture the small-scale eddies interactions in turbulence and non-linearities caused by pseudo-boiling process.
- Low mach number assumption, avoids numerical complications by considering constant thermodynamic pressure. Otherwise, the compressible solver encounter issues like pressure oscillations due to transcritical conditions and filter out the acoustic pressure waves. The low mach number consideration, retains the mechanical equilibrium of pressure across the pseudo-boiling region, by imposing constant thermodynamic pressure, and thus the real fluid properties can be acquired by tabulating the values from NIST-Refprop software for that one pressure. This is known to increase the accuracy compared to widely used cubic EoS.
- The important assumptions made in the simulation are low-mach number limit, single species, non-reacting flow, no-body forces, bulk viscosity and thermal radiation.
- The governing equations are then numerically integrated with an open source, massively parallel EoS independent low mach number version code NEK5000 based on SEM.

- The popular modelling of the Reynolds stress and the turbulent heat flux employed in turbulent modelling employed by most of the RANS and LES CFD codes is based on Boussinesq Hypothesis. Where, the Reynolds stress is considered proportional to viscous tensor. While, the turbulent heat flux is modelled proportional to the temperature (or enthalpy) gradient.
- The computational domain of the simulation is periodic in X-direction (streamwise direction) and Z-direction (span-wise direction). These directions are homogeneous i.e. averaging can be carried out along these directions (streamwise and span-wise).
- The transcritical DNS simulation of nitrogen are carried out at four different pressures, featuring same Reynolds number of jet $Re_{jet} = 3000$ at initial temperature $T_{jet} = 100$ K injected into the warm nitrogen supercritical environment at $T_{env} = 300$ K.
- The study of the injection process at three different pressure levels allows us to understand the influence of pressure on the mixing of fluid along with the pseudo-vaporization process. The stratification of thermodynamic properties like density and the near critical enhancement of properties are very significant near to the critical point (i.e. R2P1 case in our simulation), which such issue is less pronounced as the reduced pressure increases and eventually vanishes for larger reduced pressure values (≥ 3).
- Due to high stratification of thermodynamic properties near to the critical point, special attention during the simulation is require, also the need for very fine grid size is needed to capture the finest details.

Part III

RESULTS AND DISCUSSIONS

4 Results and discussion

Outline

This chapter begins with the laminar properties of the fluid at supercritical pressure, the ones carried out to study the mixing phenomenon, moving on to the DNS database and simulation domain description it is followed by the results on the average flow field, statistics and finally to modelling considerations.

- Section 4.1 illustrates the thermodynamic behaviour of the fluid at trans-supercritical environment. *How does C_p , ρ , μ , λ , Pr etc. behave with temperature and pressure ? How is near-to-the critical injection different from the far-from-the critical injection, quantitatively?*
- Section 4.2 gives a broader picture on the dimension and parameters of the simulation, discussed in the present work. *How does the simulation field look like ?, What temperature and pressure regions are being exploited ? What does the first and second moment (on-the-flow) statistics tell about the flow ? How does the wall-effect affect the near-to-the critical injection process?*
- Section 4.3 is dedicated to deeper study on the second moment statistics (variance) along the cross-wise direction of velocity components and thermodynamic variables. *How does the pressure and mixing process affect the flow, in particular the turbulent heat flux and momentum fluxes?*
- Section 4.4 discusses on the modelling consideration widely employed in LES/RANS simulations, and its accuracy in trans-supercritical simulation. *What are the widely used approaches for modelling thermodynamic and transport properties in LES/RANS? How well the β -distribution capture the DNS/exact pdf at various pressure and mixing dominated regimes? Can no-model and β -approximation mimic the real behaviour, especially C_p and ρ , if not how inaccurate can it be? How are the behaviours of Reynolds stress, turbulent heat flux and turbulent prandtl number in such conditions?*
- Section 4.6 discusses on the anisotropy of turbulent heat flux. *Can linear eddy diffusivity model precisely model the turbulent heat flux, especially near-to-the critical point, characterized by large property variations ? Do we need a better model ?*

4.1 STUDY OF LAMINAR PROPERTIES

First, it is important to understand the properties (like isobaric specific heat capacity C_p , density ρ , thermal conductivity λ or k , dynamic viscosity μ , etc.) of fluid as a function of temperature, without the influence of turbulence or mixing phenomenon taking place. Since the simulation so discussed in the present work is accomplished for four different background pressure conditions, it is equally important to understand the dependencies of such thermodynamic properties with pressure. Therefore, such dependencies are shown in the Figure 36.

In the Figure 36, most particularly in C_p and ρ profiles (see Figures 36a and 36b), it is quite impressive to see the sharp peak of isobaric heat capacity and steep stratification of density profile at the reduced pressure 1.25 (i.e. near-to-the-critical point). This effect is explained in previous chapters in detail (see Chapter 2- Section 2.1). Such stratification reduces as we move away from the critical point towards more supercritical condition. The transition from Liquid-like state to the gas-like state is marked by Widom-line which has a signature of peak in C_p . Some important characteristics during such transition from liquid-like to gas-like can be listed below. These characteristics are even more evident and strong near-to-the critical point (as one can observe in Figure 36).

- Peak in isobaric specific heat C_p (see Figure: 36a).
- Strongest density gradient with respect to temperature (see Figure 36b)
- Highest iso-thermal compressibility $c = -\frac{1}{V} \left(\frac{\partial V}{\partial p} \right)_T$ [66, Ries,F., et al., 2017].
- Poor thermal diffusivity $\alpha = \frac{\lambda}{\rho C_p}$.
- Highest molecular Prandtl number $Pr = \frac{\mu C_p}{\lambda}$ (See Figure 37).

The molecular prandtl number which is the ratio of momentum diffusivity to thermal diffusivity ν/α , is usually about unity for gases indicating both momentum and heat dissipate through the fluid at about the same rate. However, this is not seen to be true in the transcritical nitrogen jet, where its value in the vicinity of pseudo-boiling line or Widom line exceeds unity reaching the highest near-to-critical point close to 6. Such condition characterized with comparatively a large value of Pr occurs in shear layer or at an interface between the cold liquid-like jet and warm gas-like ambient nitrogen, this thermodynamic effect acts as a shield and inhibits the heat transport from the warm nitrogen environment to cold nitrogen jet [66, Ries,F., et al., 2017]. Ries et al.(2017) also mentions that, such thermodynamic shielding effect delays and/or obstructs jet disintegration process. This causes the jet

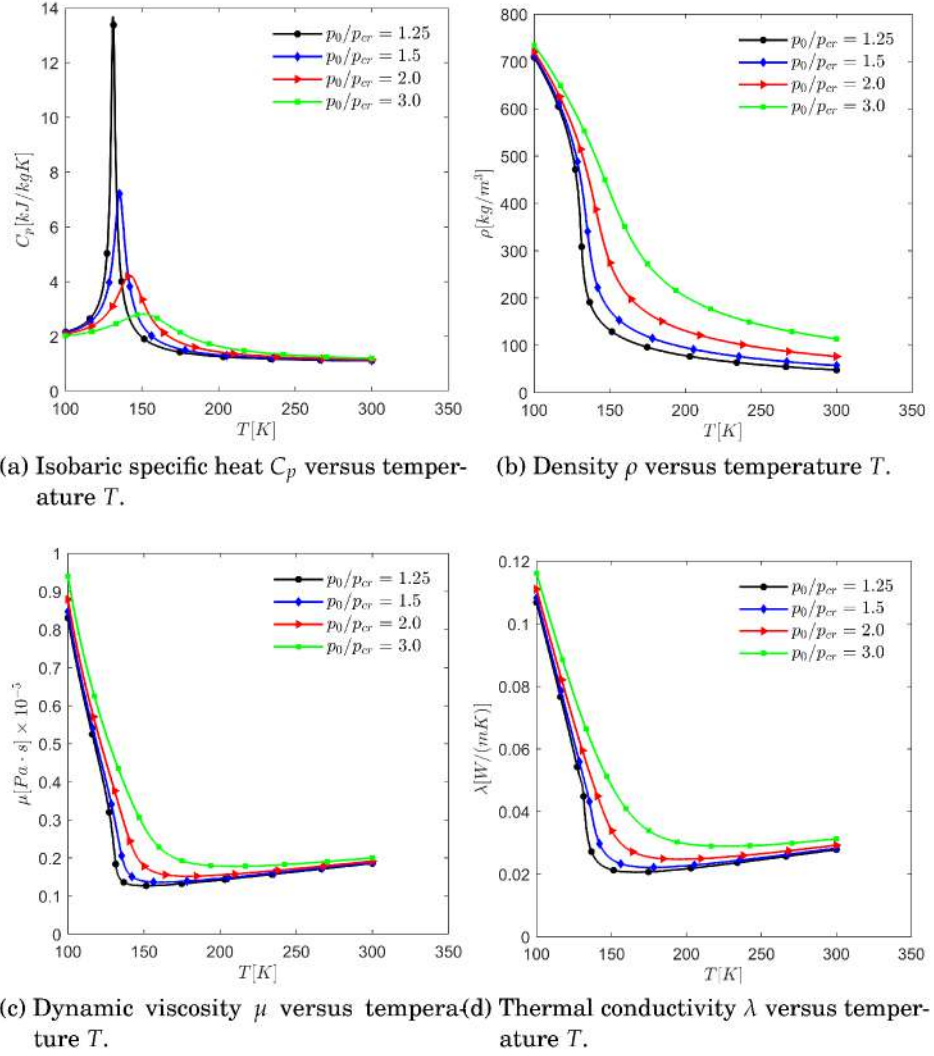


Figure 36: Laminar thermodynamic properties against the temperature for different reduced pressure values ranging from near-to-critical-point to far-from-critical-point.

at near-to-the critical point (R2P1 in our case) comparatively longer than the far-from-critical point jets (R2P4 in our case). This effect has also been termed in the literature as *Solid-Wall Effect* [55, Lapenna,P.E. & Creta,F., 2019], which is claimed to be caused by elevated density stratification in transcritical flows near-to-critical point. It will be discussed more in later sections.

The molecular Prandtl number $Pr = \frac{\mu C_p}{\lambda}$ can be therefore computed for the laminar nitrogen at the simulation pressures, which is shown in Figure 37. The profiles are similar to that of isobaric specific heat however, the magnitude differ. It can be seen that the value of molecular Prandtl number in the vicinity of critical point is about 7 times that of warm gas-like nitrogen, meaning that the Pr is about 7 folds larger at cold jet and warm ambient

interface.

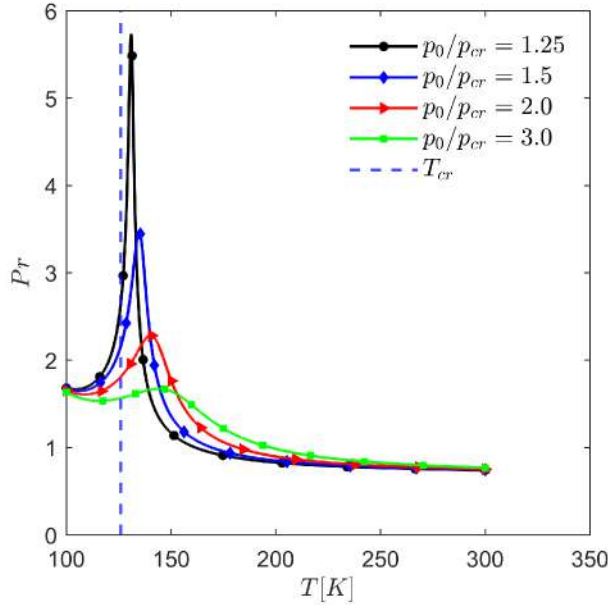
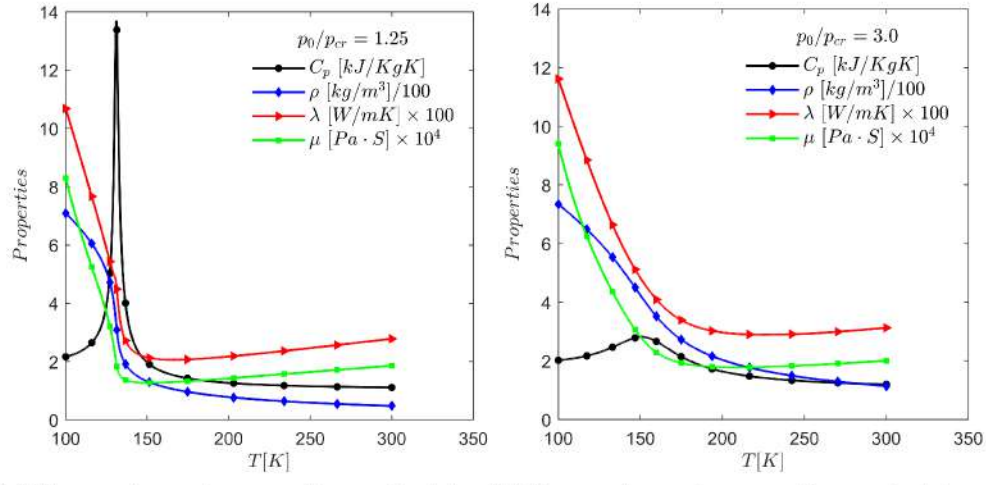


Figure 37: Molecular Prandtl number Pr against temperature at different reduced pressure values. The ' - ' vertical line represents the critical temperature of nitrogen at critical pressure i.e. reduced pressure $p_0/p_{cr} = 1$.

It should be remembered that, as the dynamic viscosity ($\mu = \nu\rho$) comes to its minimum value at Psedudo-critical temperature, the *Kolmogorov scale* $\eta_k \approx \left(\frac{\nu^3}{\epsilon}\right)^{1/4}$, under the transcritical condition is at a minimum at that temperature. Moreover, other important consideration to be made for larger Prandtl number (exceeding unity) condition is that, when the $Pr > 1$ the smallest scale of turbulence is *Batchelor Scale* and not the classical *Kolmogorov Scale* [55, Lapenna,P.E. & Creta,F., 2019], [66, Ries,F., et al., 2017], [75, Tani,H., et al., 2013]. Note that, the vice versa is true for otherwise cases. In the ideal gas condition, the Kolmogorov scale is always smaller than the Batchelor scale, $\eta_k < \eta_B$ [75, Tani,H., et al., 2013]. Therefore, the demand for smaller grid size to resolve the smallest scale, leading to consumption of more computational resources increases as simulation is carried out at near-to-critical point conditions. Such DNS resolution assessment for the present transcritical jet simulation has been studied by [55, Lapenna,P.E. & Creta,F., 2019], and will be briefly discussed in later sections.

From the above discussion, it's quiet evident that the the role of pressure is very significant in injection and mixing process of trans- supercritical fluid. The cumulative effect of pressure on different thermodynamic properties in case of near-to-critical (R2P1) and farthest-from-critical (R2P4) cases, is shown in Figure 38. The sharp diminish with peak of C_p is very much noticeable in the near-to-critical case (Figure 38a), on the other hand, the

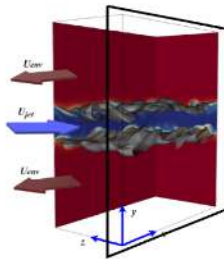


(a) Thermodynamic properties against temperature T at reduced pressure 1.25 (near-to-critical point). (b) Thermodynamic properties against temperature T at reduced pressure 3.0 (far-from-critical point).

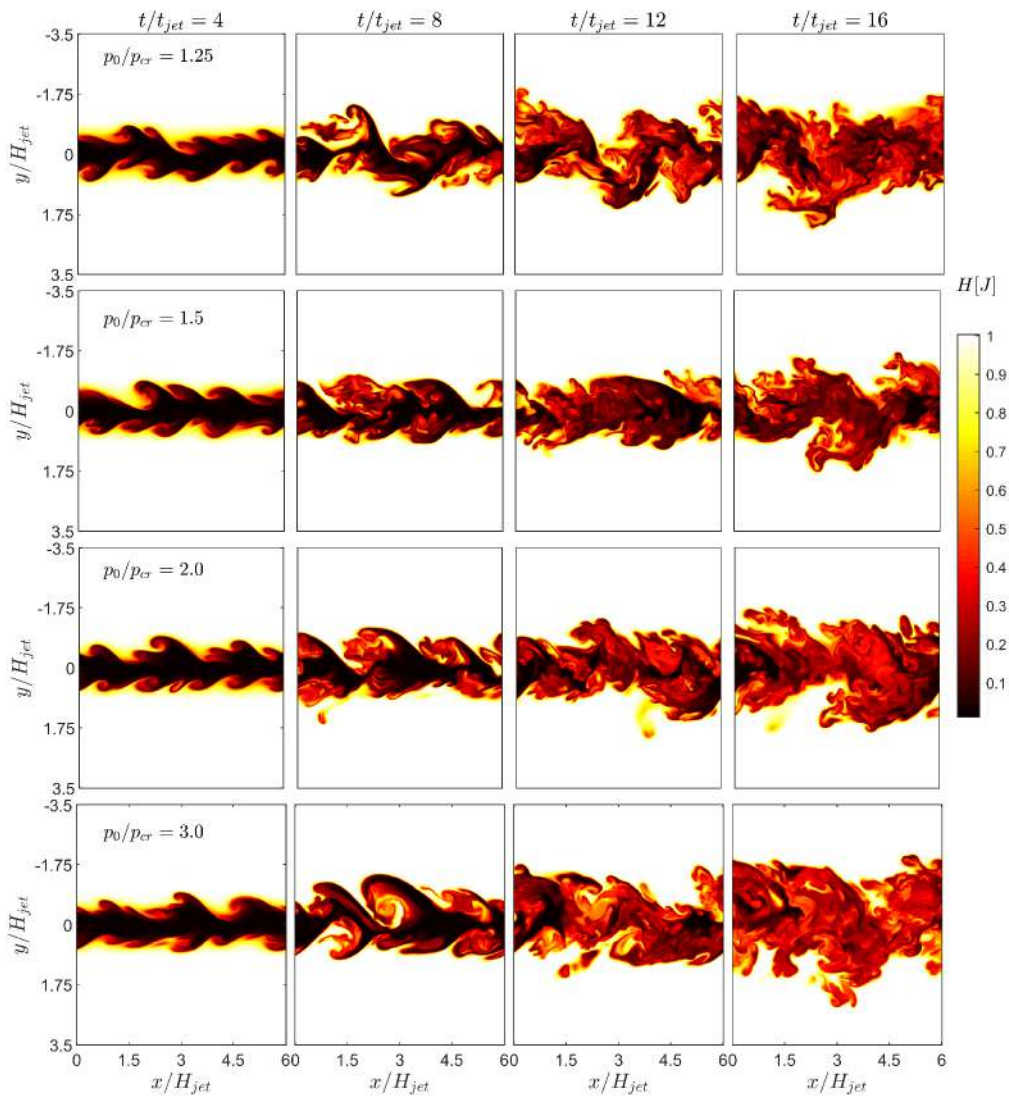
Figure 38: Isobaric specific heat capacity C_p , density ρ , thermal conductivity λ or k and dynamic viscosity μ plotted against temperature at near-to-critical point and far-from-critical point.

profiles are quite shallow and distributed in far-from-critical point case (Figure 38b). Such study leads us to the conclusion that, the temperature sensitivity of C_p strongly depends on pressure, and becomes even more rapid as temperature approaches to the critical point, implying that much more energy is needed to heat up the fluid across Widom line as such isobaric process is nearer to the critical point. At the critical point, the C_p theoretically stretches to infinity.

4.2 OVERVIEW OF THE FLOW FIELD



(a) The DNS configuration showing the cut-plane (X-Y) along which the flow is shown in Figure 39b.



(b) The enthalpy contour of the DNS at four different pressures and four different times.

Figure 39: Enthalpy H contour field of the flow, where $H = 0$ for cold transcritical injected jet at $T = 100\text{K}$ and $H = 1$ for warm supercritical N environment at $T = 300\text{K}$.

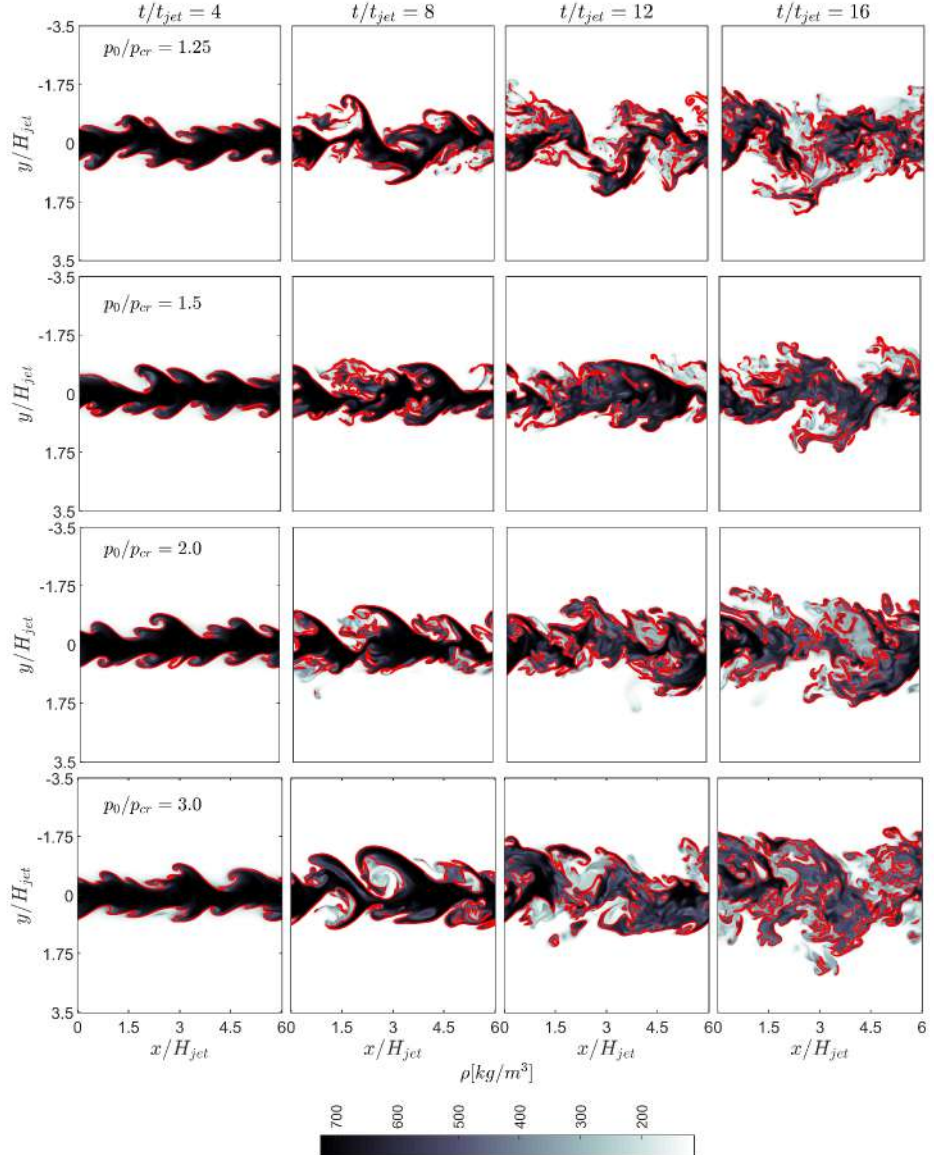


Figure 40: Density ρ contour field of the flow along streeewise direction, where $\rho \approx 700$ for cold transcritcal injected jet at $T = 100\text{K}$ and $\rho \approx 100$ for warm supercritical N environment at $T = 300\text{K}$. The iso-line is mean density between inlet and ambient N.

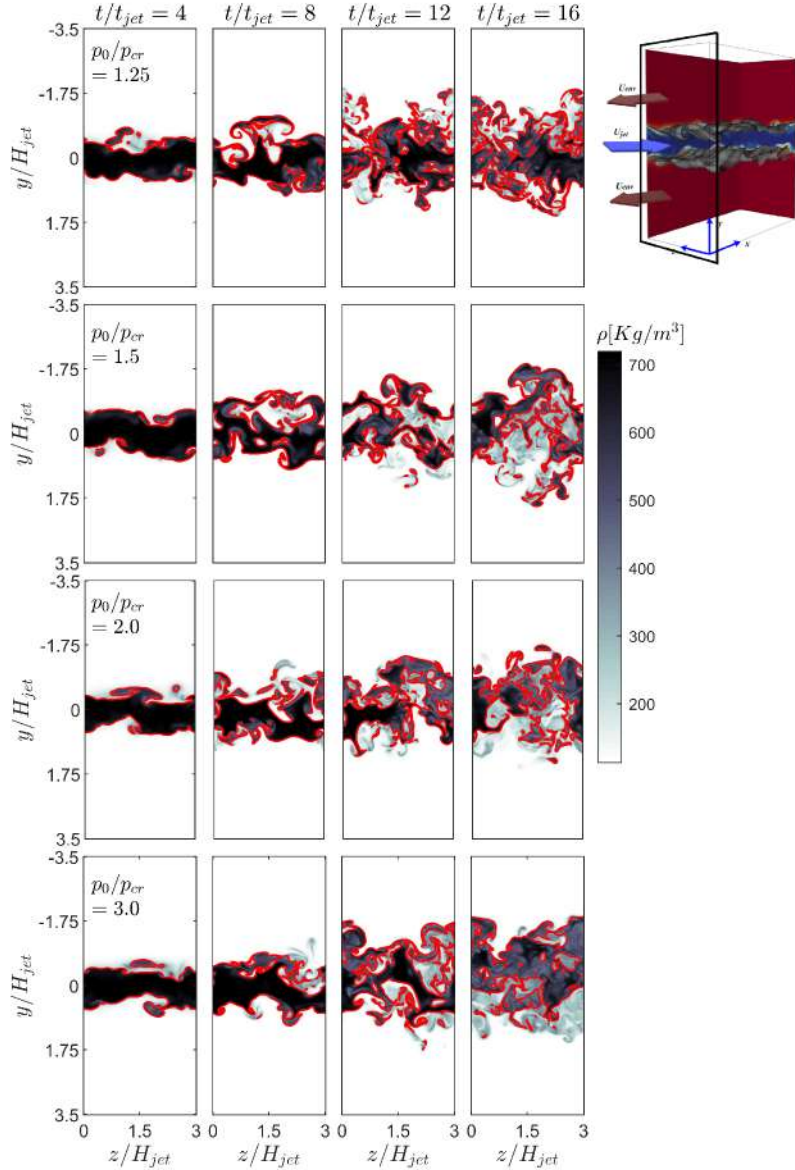


Figure 41: Density ρ contour field of the flow along spanwise direction, where $\rho \sim 700$ for cold transcritical injected jet at $T = 100\text{K}$ and $\rho \approx 100$ for warm supercritical N environment at $T = 300\text{K}$. The iso-line is mean density between inlet and ambient N.

The enthalpy flow field at selected four different time instances ($t/t_{jet} = 4, 8, 12$ and 16) for four reduced pressure values are shown in the Figure 39. All the flow and thermodynamic variables for the same time and reduced pressure values are readily available for the statistics to understand the mixing process. However, during *on-the-fly*, it was possible to carry out some fundamental statistics like averages, and variances along the cross-wise directions which are discuss in upcoming sections and subsections. However, the detail explanations on the same can be found in [53] - [58][Lapenna,P.E., Creta, F., *et al.*, 2016-2019]. Some of the important findings in terms of mixing evolution and its dependencies on pressure can be studied with the help of such statistics.

It is important to understand the flow behaviour prior to thermodynamics and statistical study of the flow. The initial disturbance in the flow field by the injection triggers a shear layer instabilities while it grows giving raise to a large scale structures popularly known as *Kelvin-Helmoltz (KH)*¹ structures (very evident in $t/t_{jet} = 4$). This large scale KH instabilities are due to shearing induced by large velocity and density gradients. The discontinuity of density and velocity in each fluid layer/plane at the interface (i.e. liquid and gas interface), give raise to a tangential velocity component and thus to the formation of vorticity at the interface. This causes unstable vortex sheet that rolls up into a spiral. This roll up causes the heavier fluid parcels to raise up from the lower denser fluid while the lighter fluid parcels are pushed down. Meanwhile, the energy for the same is extracted from the mean flow. Such KH instabilities occurs not just in fluid injection but also in the atmosphere, oceans, interstellar clouds, supernovae explosions, high energy density plasmas and quantum fluids [1, Vujinović, A., 2015] [28, Hanasz, A., *et al.*, 1996]. It is a very important phenomenon in the injection process of transcritical jet, where the growth of KH instability leads to vortex formation and finally to jet break up. It has been shown that mechanism of jet break up and mixing is mainly driven by the formation of large scale KH vortices [45, Müller,H., *et al.*, 2016].

	R2P1	R2P3	R2P3	R2P4
p_0/p_{cr}	1.25	1.5	2.0	3.0

Table 15: The simulation cases, each reduced pressures consists four time instances.

Recall that the configuration of the study are tabulate in Table ???. The Reynolds averaged stream-wise velocity (Figure 42a), density (Figure 42b) and enthalpy field (Figure 42c) computed *on-the-fly* is reported in Figure 42. The effect of pressure on the jet spreading is quiet evident in those figures. The jet is very much flat after $t/t_{jet} \sim 8$ in near-to-critical point (case R2P2),

¹ KH instability was first studied by Hermann von Helmholtz in 1868 and Willam Thomson (Lord Kelvin) in 1871, and is named after them.

while the jet spreads significantly for the far-from-critical point pressures, in the same time interval. Most importantly, if we study the time evolution of the temperature range between T^- and T^+ denoted by dash-dotted and solid line in the Figures 42, such spacing keeps increasing significantly for higher pressures while, range is very much limited R2P1 case.

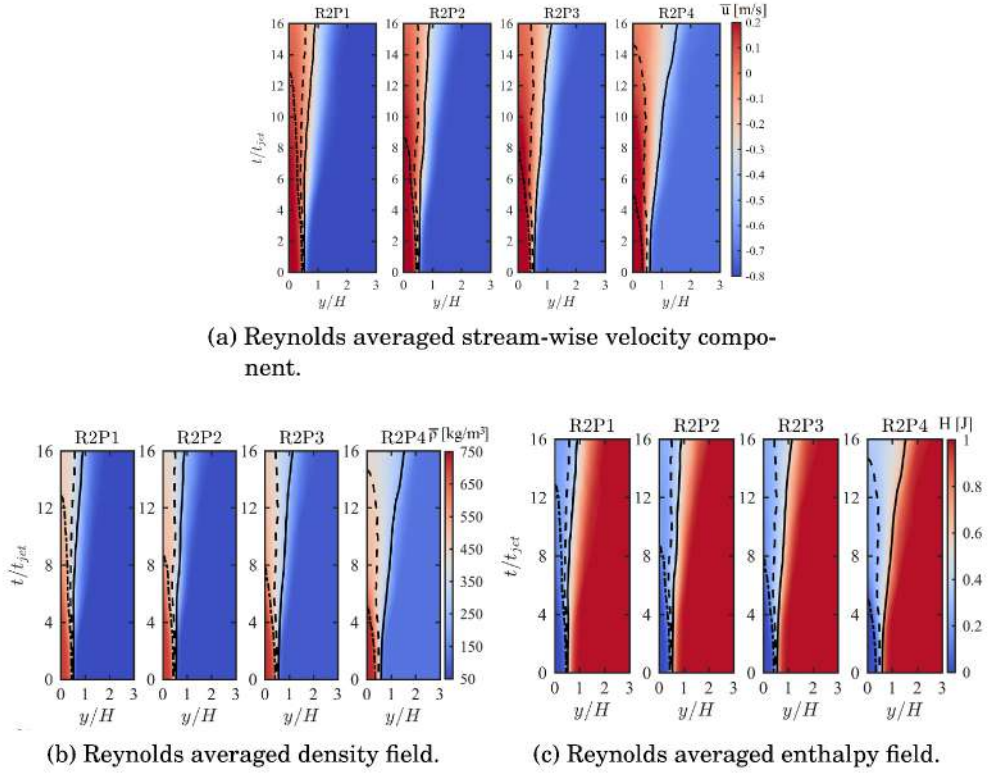


Figure 42: The contours showing the Reynolds averaged fields with superimposed isolines of temperatures corresponding to T^+ (continuous line), T_{pb} (dashed line) and T^- (dashed dotted line) i.e. gas-like state, pseudo-boiling and liquid-like state respectively, as discussed previously in enthalpy budget (see 2.1.2 and Figure 22) [58, 55, Lapenna,P.E. et al., 2018-19].

The other important observation is in terms of liquid-like state temperature boundary denoted by the dash-dotted line alone. For the case of R2P1, it extends upto $\sim t/t_{jet} = 12$, while on the contrary it terminates at $\sim t/t_{jet} = 4$ for R2P4. This proves that, the liquid-like jet core remains in its liquid-like state until significant amount of time for near-to-the critical transcritical injection (such as R2P1), which is not true for the far-from-the critical point injection (such as R2P4).

The transition from the liquid-like jet state to the gas-like state, as discussed multiple times in previous sections, is characterized by steep gradient in thermodynamic properties, corresponding to the pseudo-boiling temperature T_{pb} (dashed) isoline. The other important conclusion from the Figure 42, in terms of pseudo-boiling/ pseudo-vaporization is that, the liquid jet core

undergoes complete pseudo-vaporization by the end of simulation (i.e. t / t_{jet}) and therefore leaving with only gas-like phase in the case of R2P4, while in the case of R2P1, the liquid jet core is still intact with liquid-like state which is yet to undergo the process of pseudo-boiling, this is because of the fact that temperature range within which such process of pseudo-boiling occurs is very much confined in the case of R2P1 while it is within a wide range in R2P4, as discussed in section 4.1 (see Figures 36a and 36b).

This mechanism has also been explained in terms of *heat-shield* in the literature by [55, Lapenna,P.E. & Creta,F., 2019]. The sharp peak of isobaric specific heat in the R2P1 case (see Figure 36a) refers to significantly large contribution of the structural energy, which is required to overcome for the transition, acting as a *heat-shield* in the near-to-the critical point injection. Such effect reduces, for higher pressure regime (such as R2P4), so that the process of pseudo-vaporization is fast with faster vanishing liquid jet core. Furthermore, since the DNS dataset has been stored only for the limited time instances, more insight on the dynamics of the flow can be closely studied through statistical study of so acquired dataset, and are described in the upcoming sections and subsections.

4.2.1 Density profiles

The non-dimensionalized density evolution along the cross-wise direction (Y-direction) is shown in Figure 43. Since the simulation is symmetric about X-axis (stream-wise direction), only the half of the profile is reported in the figures, most of them are mirrored informations. Each sub-plot in Figure 43 corresponds to the different pressure values, containing four-time instances information, and the averages are carried out along stream-wise and cross-wise directions (i.e. homogeneous directions). One can clearly notice that,

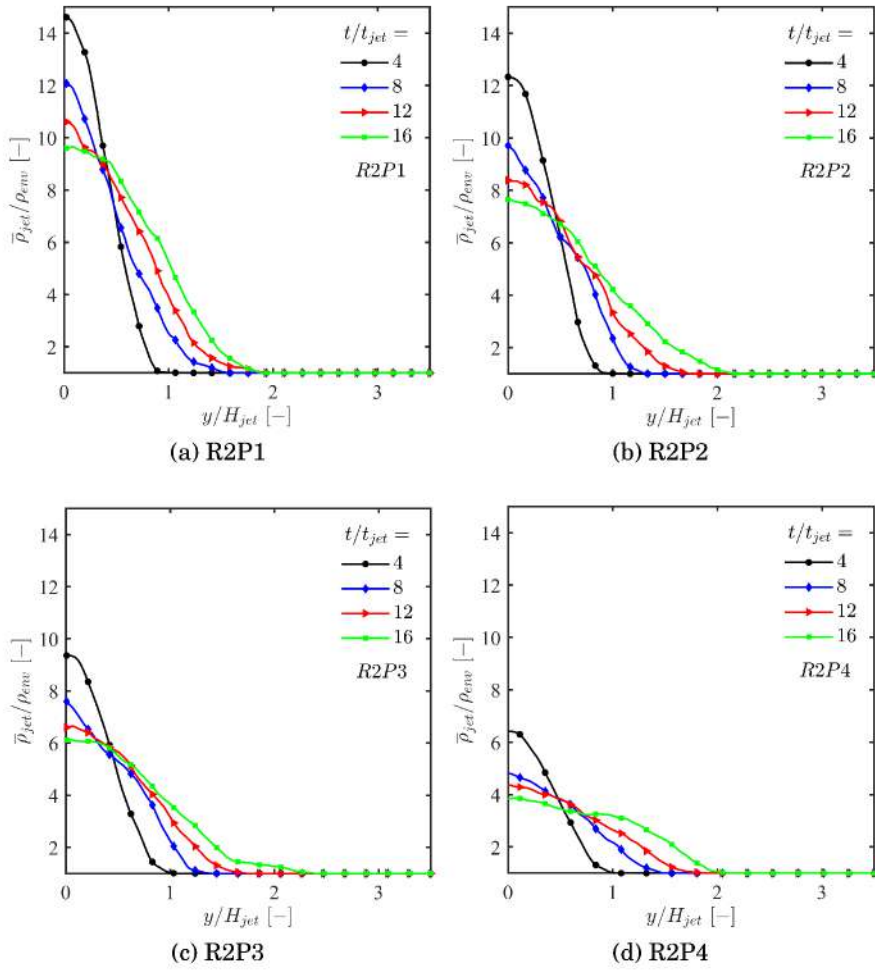


Figure 43: Reynolds averaged Non-dimensional density profiles at 4 different pressure levels each at 4 different time instances. The averaging has been carried out along the stream-wise and span-wise direction.

the pressure has considerable effect on the averaged density profiles. As, discussed previously, strong density gradient is observed in the case of R2P1. In time, the steep gradient reduce and spread out reaching upto 50% of the half-width at last time instance, due to the fact that the turbulence and mixing take place at those instances. More importantly, the jet undergoes the process of pseudo-vaporization considerably soon for higher pressures,

resulting gas-like densities rather than liquid-like in those pressures (such as R2P4). This is in contrary to the R2P1 where the averaged density is considerably high even in the last time instance.

4.2.2 Isobaric specific heat profiles

The heat capacity peaking in the R2P1 case is obvious as per our previous explanations (refer Section 4.1). One of an important observation in Figures 44 is that the peaks in $\overline{C_p}$ especially evident at $t/t_{jet} = 4$ are located little away from the core i.e. $y/H_{jet} \approx 0.5$, this location corresponds to the shear or mixing layer, where the cold jet undergoes shear with the warm environment, the cold region heat up and crosses the pseudo-boiling line (at corresponding pseudo-boiling temperature T_{pb}) as it gets heated. Such crossing through Widom-line is reflected as $\overline{C_p}$ peak, which is very much distinct in near-to-the critical point (case R2P1). As the process of mixing favoured by turbulence

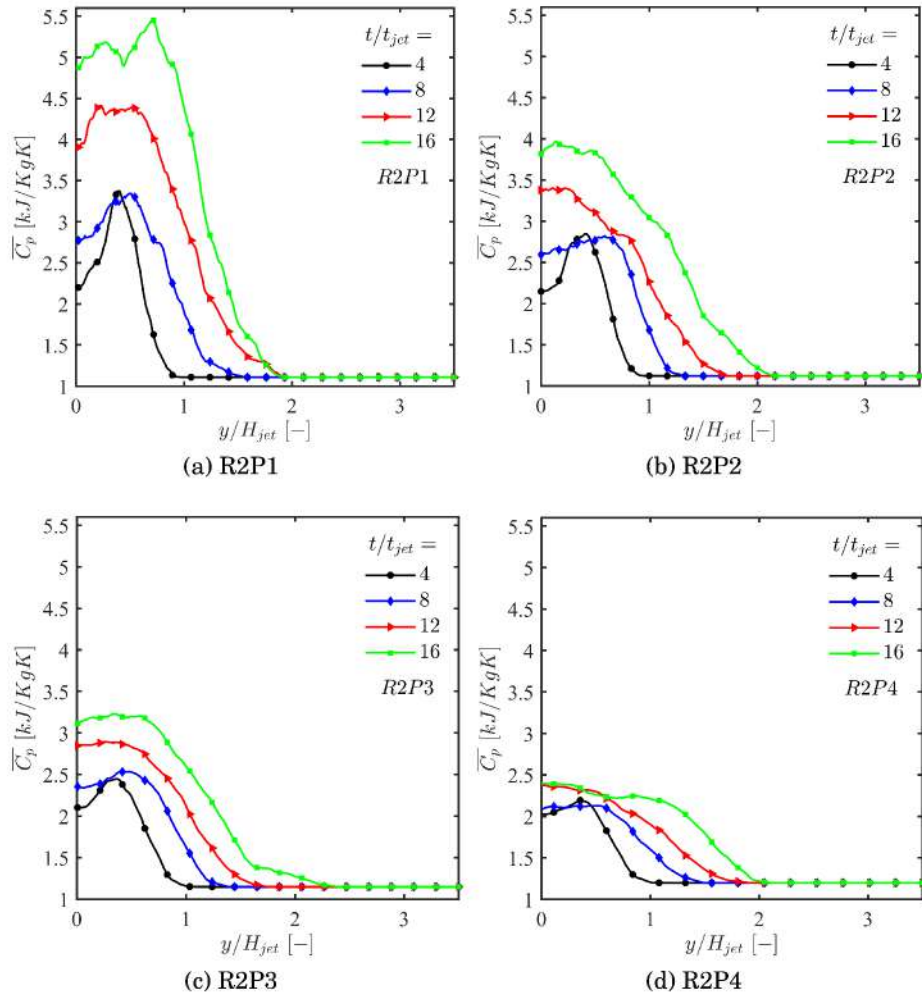


Figure 44: Reynolds averaged isobaric specific heat $\overline{C_p}$ evolution along cross-wise direction, at four-different pressures each at four-different time instances.

becomes dominant part in later time instances, the $\overline{C_p}$ value even raises (increase is around 20 %) while the peaks spread out. However, such increase in the $\overline{C_p}$ value is not so evident in far-from-the critical point cases (R2P4). The increase in $\overline{C_p}$ is around 5%. This shows that the mixing and heat transfer process in these cases are not identical and require further detail study.

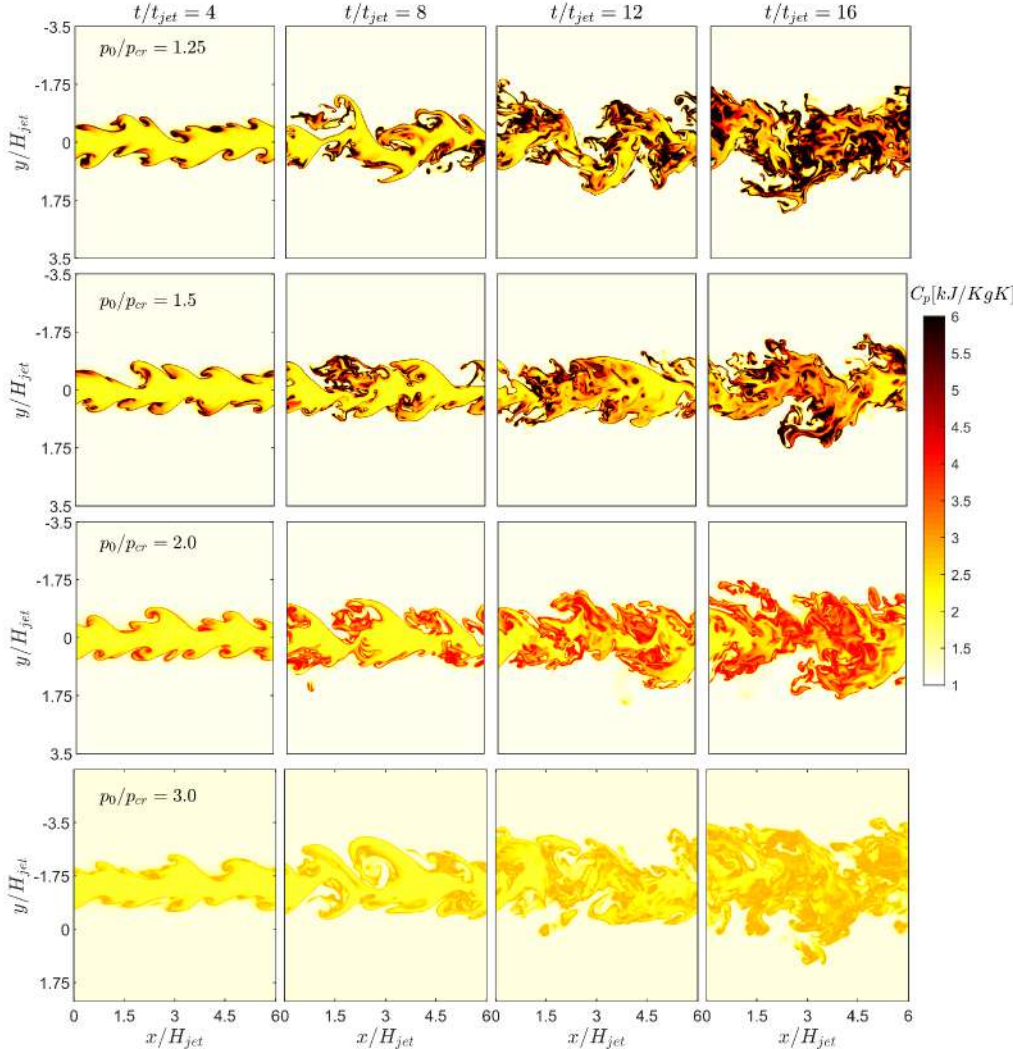


Figure 45: 2D contour plot of isobaric specific heat C_p at four different pressure levels (rows) each for four time instances (columns).

4.2.3 Enthalpy profiles

In conjunction with the temperature, the enthalpy evolution can also be considered as reported in Figure 46. The enthalpy variation is pretty much identical in all four cases however, the magnitude of \overline{H} reduces for larger time instances and moving far-from-critical point by about 15%. Plus the

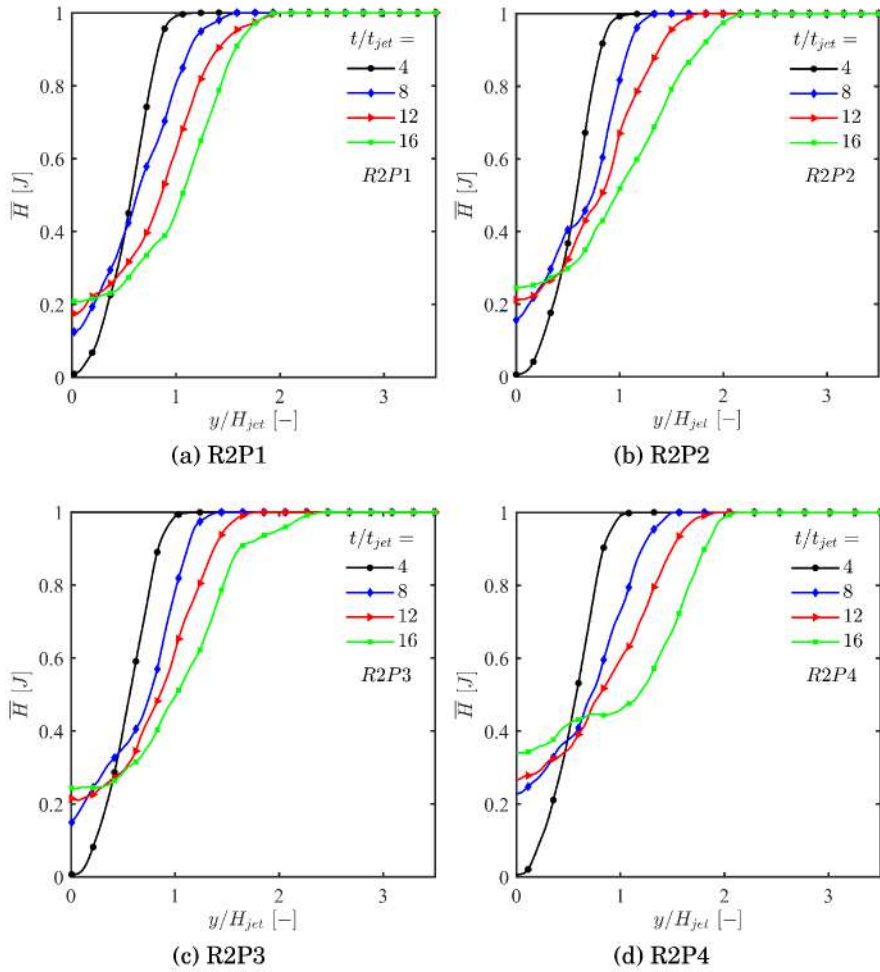


Figure 46: Reynolds averaged enthalpy \bar{H} evolution along the cross-wise direction. $\bar{H} = 1$ corresponds to the warm environment ($T = 300$ K), while $\bar{H} = 0$ corresponds to the cold jet ($T = 100$ K).

jet spreading i.e. the mixing layer thickness growth, can be observed for the case R2P4.

4.2.4 *Reynolds versus Favre averages*

Reynolds and Favre averaging procedures (as discussed in Chapter ?? Sub-sections: 1.7 and 1.7), are not identical. The Reynolds average $\bar{\square}$ neglects the density fluctuations, therefore, is suitable for density-constant flows (such as non-reacting flows). On the other hand, the Favre average $\tilde{\square}$ is density-weighted averaging procedure. These two techniques don't agree in the region where the density varies significantly, which can be observed in our simulation in Figure 47.

In the Figure 47, the solid line – represents the Reynolds average $\bar{\square}$ while the dashed-line — represents the Favre averages $\tilde{\square}$. These two profiles,

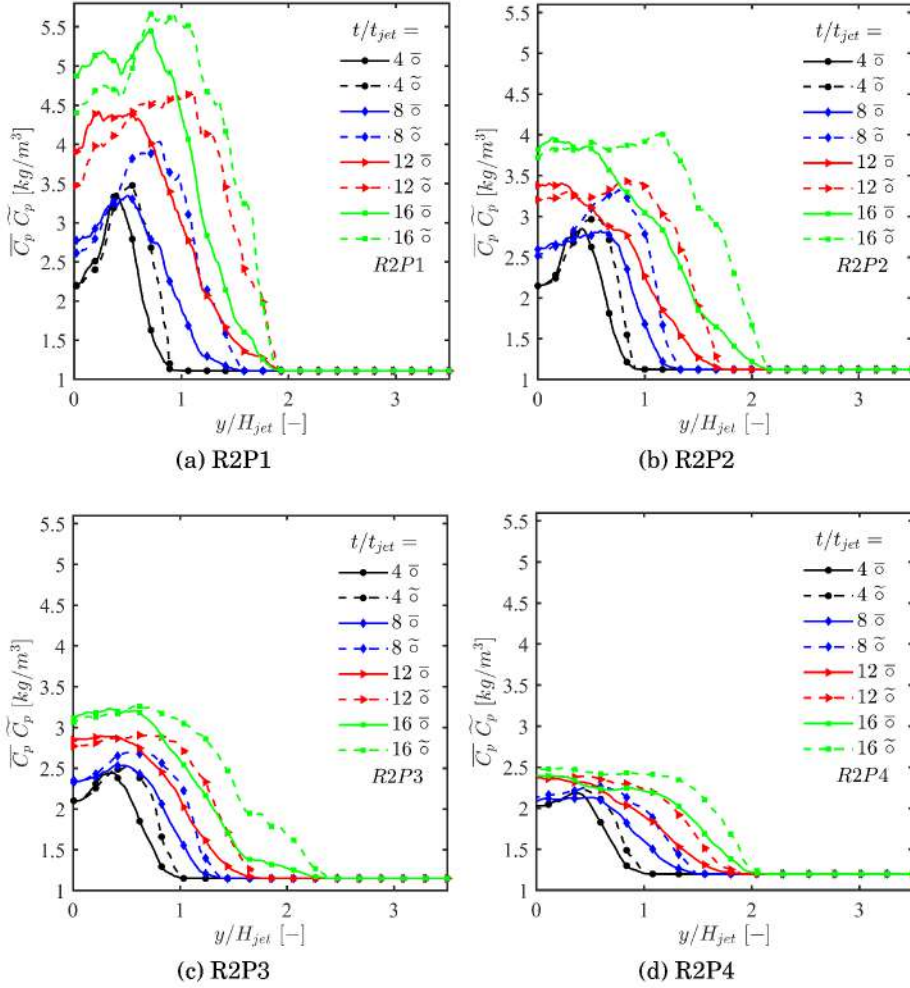


Figure 47: Reynolds (solid –) and Favre (dashed ––) averaging compared with the isobaric density profiles.

agree very well to the right (i.e. warm environment), where the flow field is unaffected by turbulence and/or pseudo-vaporization, thus, the density is constant. This is also true in the case of cold jet (to the left of the plot), where the flow and hence the density is undisturbed especially at the first time instances *black profiles*, making both profiles overlap in the core region. Most of the disagreement is at the diminishing (stratification) part where pseudo-vaporization occurs, and last time instance where mixing and turbulence is dominant. The effect of pressure can also be noticed in the same, the larger disagreement between two averaging processes is more in R2P1 than in R2P4.

4.3 VARIANCE STUDY

This section is intended to study the variance of the flow and thermodynamic variable along the crosswise direction. In addition to which, so obtained profiles are compared with the variance field (2D contour) obtained for every time instances during *on-the-fly* of the simulation, as reported for by [55, Lapenna,P.E. & Creta,F., 2019]. The flow variable variance includes $\overline{u'u'}/\Delta u^2$, $\overline{v'v'}/\Delta v^2$ and $\overline{w'w'}/\Delta w^2$, where u , v and w are the velocity components along X- (stream-wise), Y- (cross-wise) and Z- (span-wise) directions respectively. The normalizing factor is the squared of the initial mean shear ($\Delta u = u_{jet} - u_{env}$). And the thermodynamic (mixing) variable variance includes $\overline{\rho'\rho'}/\Delta \rho^2$, $\overline{\xi'\xi'}/\Delta \xi^2$ and $\overline{C_p'C_p'}/\Delta C_p^2$, where ρ , $\xi = h - h_{jet}/(h_{env} - h_{jet})$ and C_p are density, non-dimensionalized enthalpy and isobaric specific heat capacity respectively. The study has been carried out for all four pressures (viz. R2P1, R2P2 R2P3 and R2P4) each for four time instances (viz. $t^* = 4$, $t^* = 8$, $t^* = 12$, and $t^* = 16$), where $t^* = t/t_{jet}$ is the reference time.

The spread of fluctuations ϕ' (of a variable say, ϕ) about the mean value $\bar{\phi}$, can be studied with Root Mean Square (RMS) and variance. Consider a random variable vector A made up of N scalar observations of a discrete data set, the variance Var , mean μ and root mean square RMS is defined as;

$$Var = \overline{(\phi')^2} = \frac{1}{N-1} \sum_{i=1}^N |A_i - \mu|^2 \quad (94)$$

$$Mean = \mu = \frac{1}{N} \sum_{i=1}^N A_i \quad (95)$$

$$RMS = \phi_{RMS} = \sqrt{\overline{(\phi)^2}} \quad (96)$$

The variance is the second order moment while mean is the first order moment. The square root of the variance is the standard deviation or RMS of the variable. The variance of the thermodynamic and flow variable for all the cases have been studied in this section. The variance is computed along the cross-wise direction while statistics have been acquired along the span-wise and stream-wise direction. All the variance profiles are superimposed with the Reynolds averaged profiles to have an idea to quantities variations and its relation with variance.

4.3.1 Variance of isobaric specific heat

The pressure dependency in C_p variance is very significant from the above reported Figure 48. The elevated variance along with the average profile in R2P1 is very evident. Variance is reported to be minimum in the undisturbed regions of the flow field while it increases in the mixing layer. The maximum is attained approximately at a location of maximum shear. The jet centreline however, has considerably less variance. It has been pointed out (by [54, Lapenna,P.E. & Creta,F., 2017]) that this behaviour is due to the fact that

the, initial jet Reynolds number is considerably low and the jet doesn't reach *self-similar state*². The very possible explanation for the large variance in R2P1, even though the Reynolds number is considered to be the same in all four cases, is due to the thermodynamics, i.e. very sharp rise in the C_p at near-to- the critical point. Further, study on the variance of the flow velocities are discussed in next subsections.

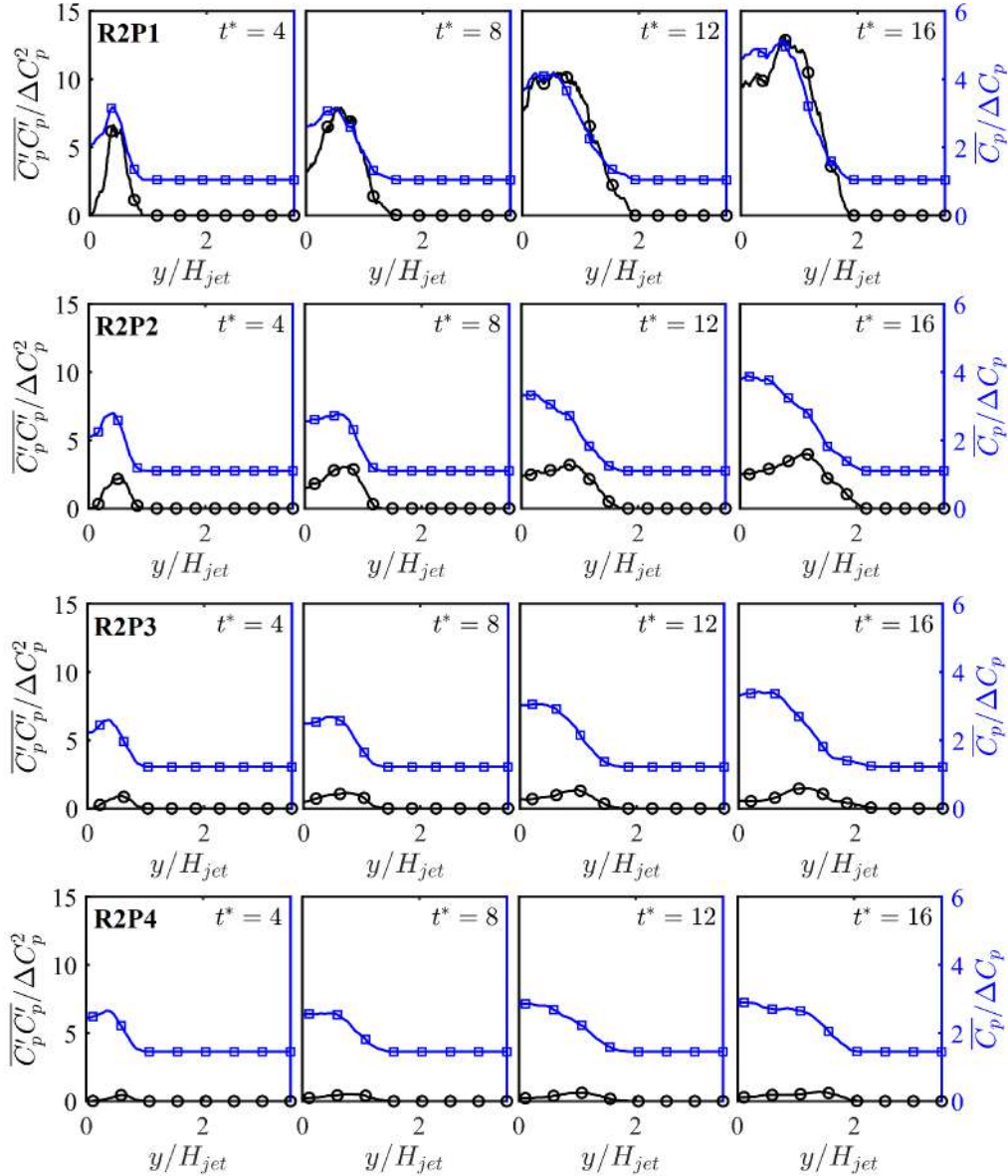


Figure 48: The variance of isobaric specific heat capacity $\overline{C'_p C'_p} / \Delta C_p^2$, denoted by \circ and its average $\overline{C_p}$, denoted by \square along the cross-wise direction, at four different reduced pressures and corresponding four time instances.

2 Self similarity: The state in which the solution is similar to itself. This is an important class of phenomenon in which scale symmetry allows to reduce the number of independent variables of the problem. Details can be found in [25, Gratoon, J., 1991]

4.3.2 Variance of velocity component

A broad view of the flow field and important regimes in the flow field where most of the dynamics both in terms of thermo- and physical sense can be observed in the velocity flow field contours reported in Figure 49. All these field values are normalized by a common denominator i.e. the square of initial mean shear Δu^2 , the superimposed isolines of the temperatures defining the boundaries of the pseudo-vaporization region give even more insight into the physics of the phenomenon.

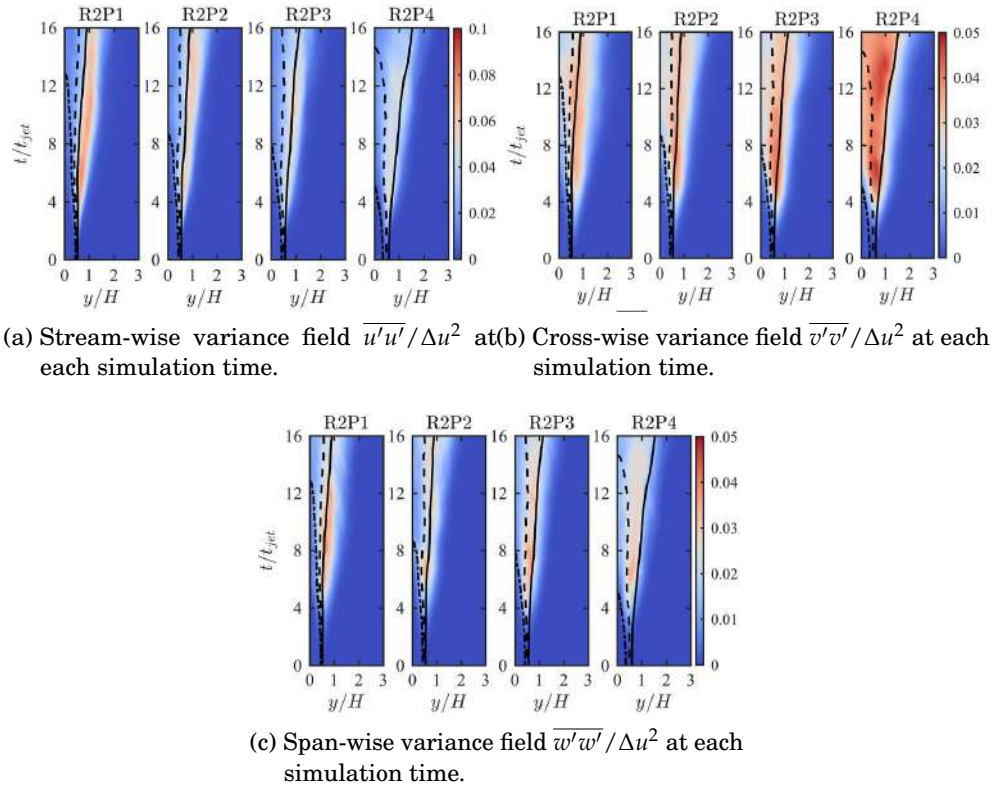


Figure 49: Velocity variance field computed *on-the-flow* at each simulation time reported by [55, Lapenna,P.E. & Creta,F., 2019]. The superimposed isolines represents temperatures corresponding to T^+ (continuous line), T_{pb} (dashed line) and T^- (dashed dotted line) i.e. gas-like state, pseudo-boiling and liquid-like state respectively, as discussed previously in enthalpy budget (see 2.1.2 and Figure 22).

All the velocity components (stream-wise, cross-wise and span-wise), for all cases have a commonality i.e. near-to-the critical point R2P1, has considerably narrow region of variance peaks located close to T^+ (continuous line) (see Figures 49a, 49b and 49c). While, it's spread over in a wide range from T^- to T^+ and the fluctuation intensity reduces as pressure increases, this is very much evident in R2P4 especially the cross-wise component [see Figure

49b].

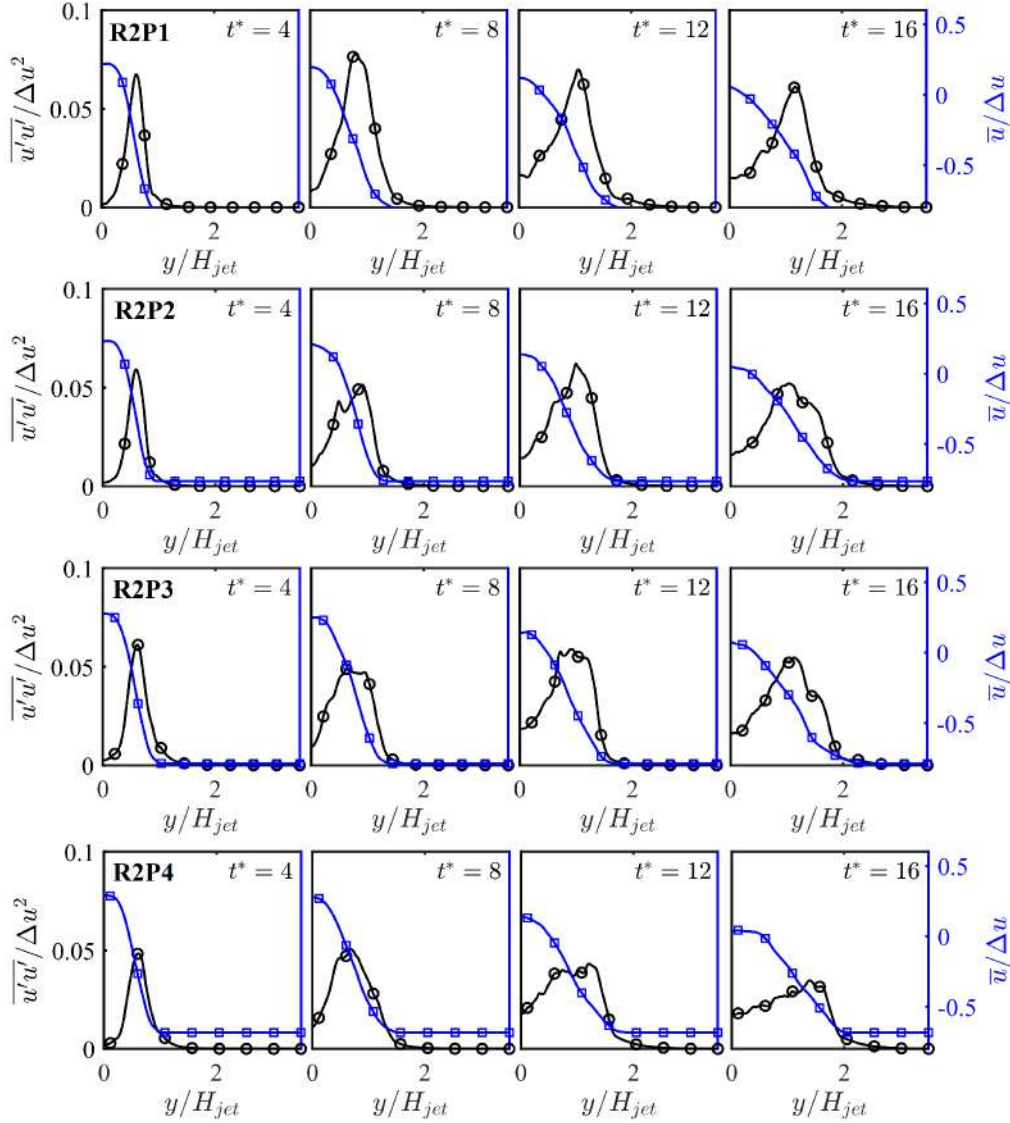


Figure 50: Normalized variance of stream-wise velocity component $\bar{u}'\bar{u}'/\Delta u^2$ marked by (\circ) and normalized \bar{u} marked by (\square) , against cross-wise direction, at four different reduced pressure levels.

It is very important to introduce of a concept of *Solid-Wall Effect*. The strong density gradient or stratification (like the in the case of R2P1) strongly contributes to the modification in the dynamics of the fluid motion like in the development of large-scale KH structures, thus changing the dynamics of mixing. Thus the surface layer acts as a *solid-wall* in the flow that reduces the velocity fluctuations in the cross-wise direction and amplifies in the stream-wise direction. This behaviour allows the transfer of the turbulent kinetic energy from its cross-wise component to the stream-wise component. This process of energy redistribution among spatial components due to solid-wall effect as a consequence of density stratification, significantly modifies

the amount of available energy for fluid mixing at the density interface. This has been discussed by [88, Zong,N., Yang,V. *et al.*, 2004] and [58, 55, Lapenna, P.E. & Creta,F., 2019].

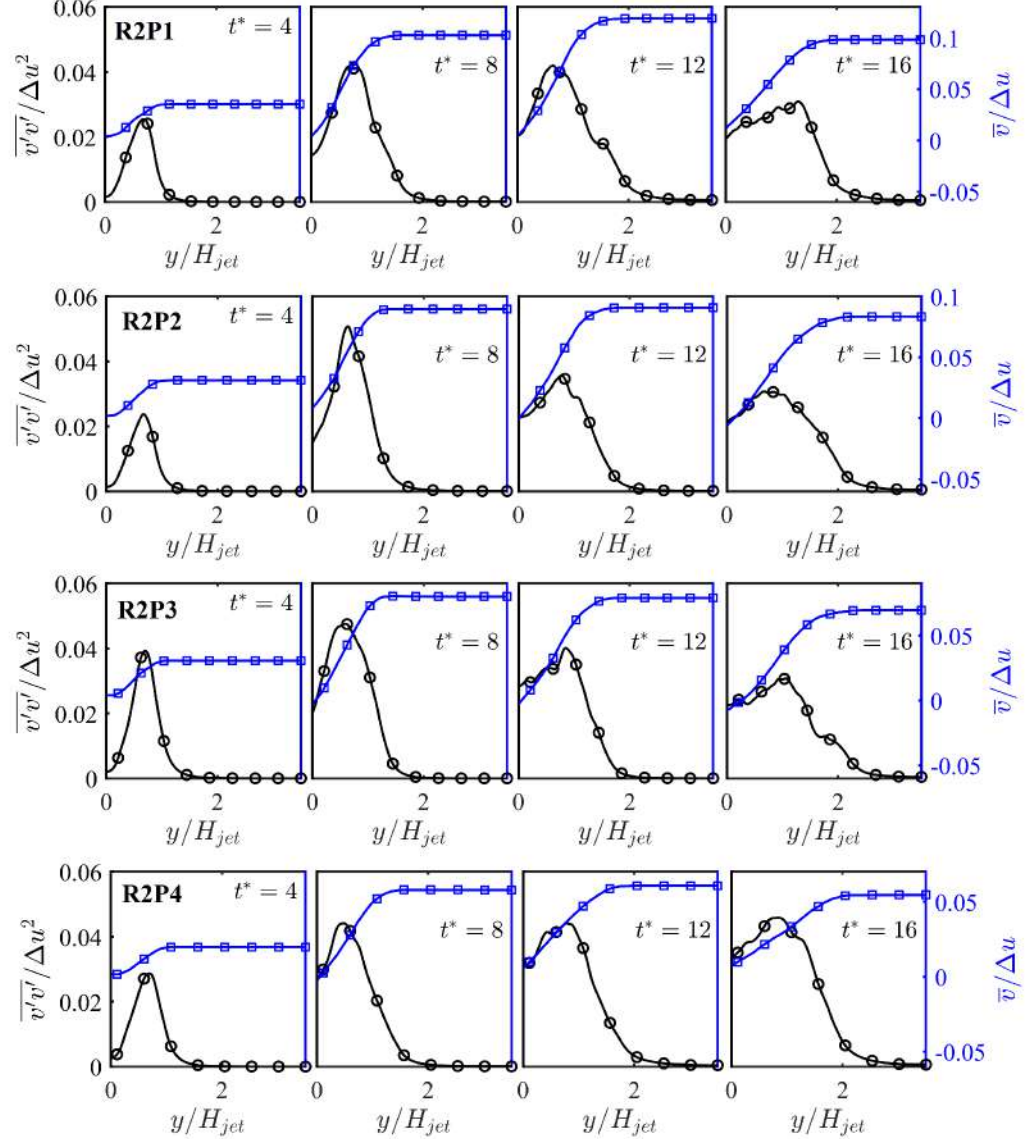


Figure 51: Normalized variance of cross-wise velocity component $\bar{v}'\bar{v}'/\Delta u^2$ marked by (\circ) and normalized \bar{v} marked by (\square), against cross-wise direction, at four different reduced pressure levels.

In our simulation result (see Figure 49, all four cases), the solid wall effect can be distinctly observed. In a condition with high density gradient, R2P1, The velocity fluctuation in the cross-wise direction (Figure 49b, R2P1) is reduced, and amplifies the fluctuations in the stream-wise direction (Figure 49a, R2P1). This, effect significantly decreases for higher reduced pressures. Moreover, since the jet core in R2P1 remains liquid-like for a long time, the higher liquid-like density causes damping effect of the fluctuations [55,

Lapenna, P.E. & Creta,F., 2019]. The behaviour of the span-wise fluctuation (Figure 49c) is very similar to stream-wise velocity fluctuations because of the fact that the configuration of the planar jet is such that, the mean stratification along cross-wise direction and not along span- or stream-wise directions.

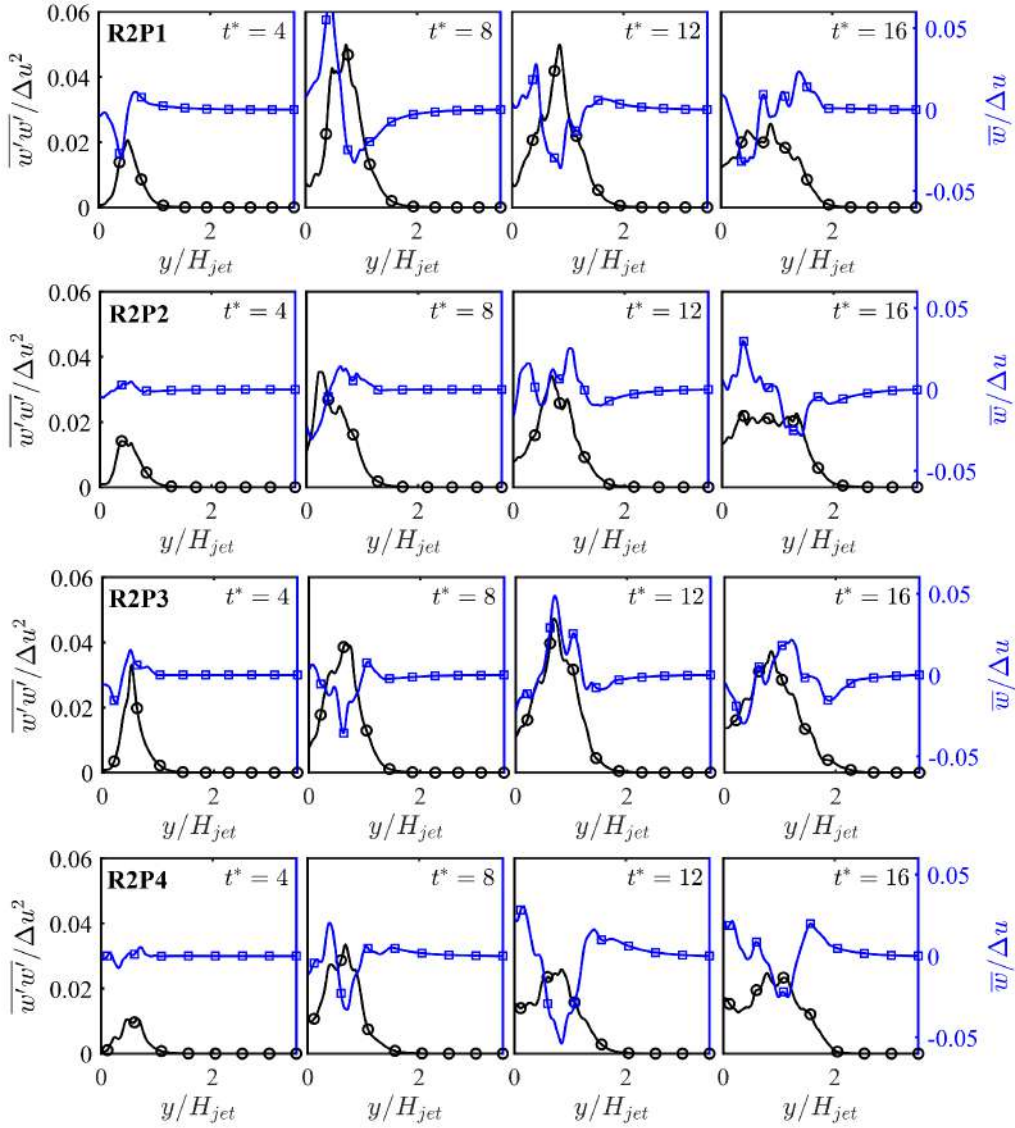


Figure 52: Normalized variance of span-wise velocity component $\overline{w'w'}/\Delta u^2$ marked by (\circ) and normalized \bar{w} marked by (\square) , against cross-wise direction, at four different reduced pressure levels.

Moving forward to the stored dataset, 1D (along the cross-wise direction) variance can be studies for each velocity components giving more ideas on the maximum variance and its pressure dependencies. Meanwhile, the variance field contours (discussed above Figure 49), give an idea about the time instances, where pressure dependencies on the variance are comparable.

The normalized variance of the stream-wise velocity component is considerably large as compared to that of the other components, reason being the solid wall effect. The variance level reduces close to zero in the jet core region while peaking close to the shear layer, with this logic one can also observe that the shear layer thickness increases along with time. The case with the most density stratification i.e. R2P1 has the highest level of variance, especially of the stream-wise velocity component.

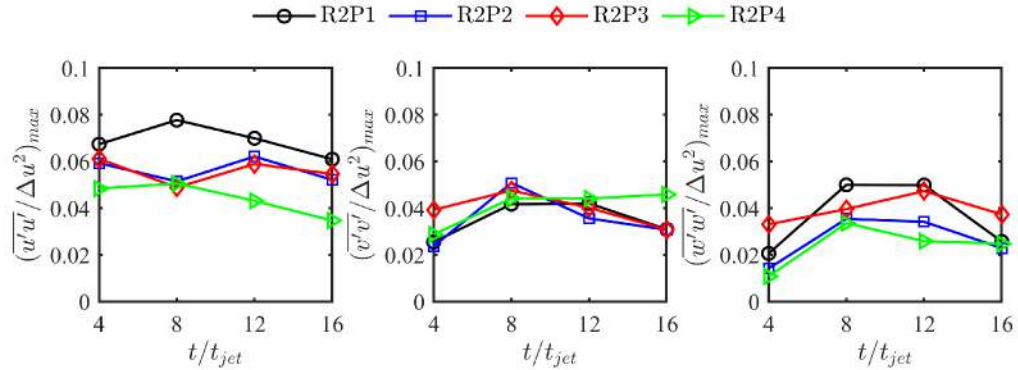


Figure 53: The peaks of the normalized variance of span-wise, cross-wise and stream-wise velocity components at four different reduced pressure levels.

4.3.3 Variance of scalars

It has been pointed out (by [55, Lapenna, P.E. & Creta,F., 2019]) and have been previously shown that, the non-linearities of thermodynamic and transport properties strongly impact on gradients and fluctuations in space and time, during jet development.

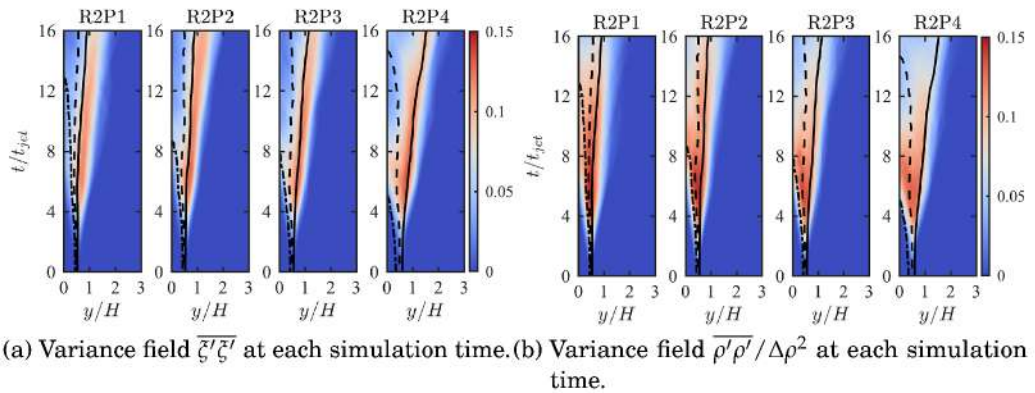


Figure 54: Density and enthalpy variance field computed *on-the-flow* at each simulation time reported by [55, Lapenna,P.E. & Creta,F., 2019].

One of the common observation in the non-dimensional temperature field contour for all cases is that, the peaks in the variance lie close to the gas-like temperature region i.e. T^+ isoline. The pressure dependency can be

better studied with the help of Figure 57, where the peaks of the average variance at reach time instances for all four cases are shown. It shows that, the peak values of the density variance ($\overline{\rho' \rho'}/\Delta \rho^2$)_{max} decreases as pressure increases due to large non-linearities of thermodynamic properties at near-to-the critical region (case R2P1).

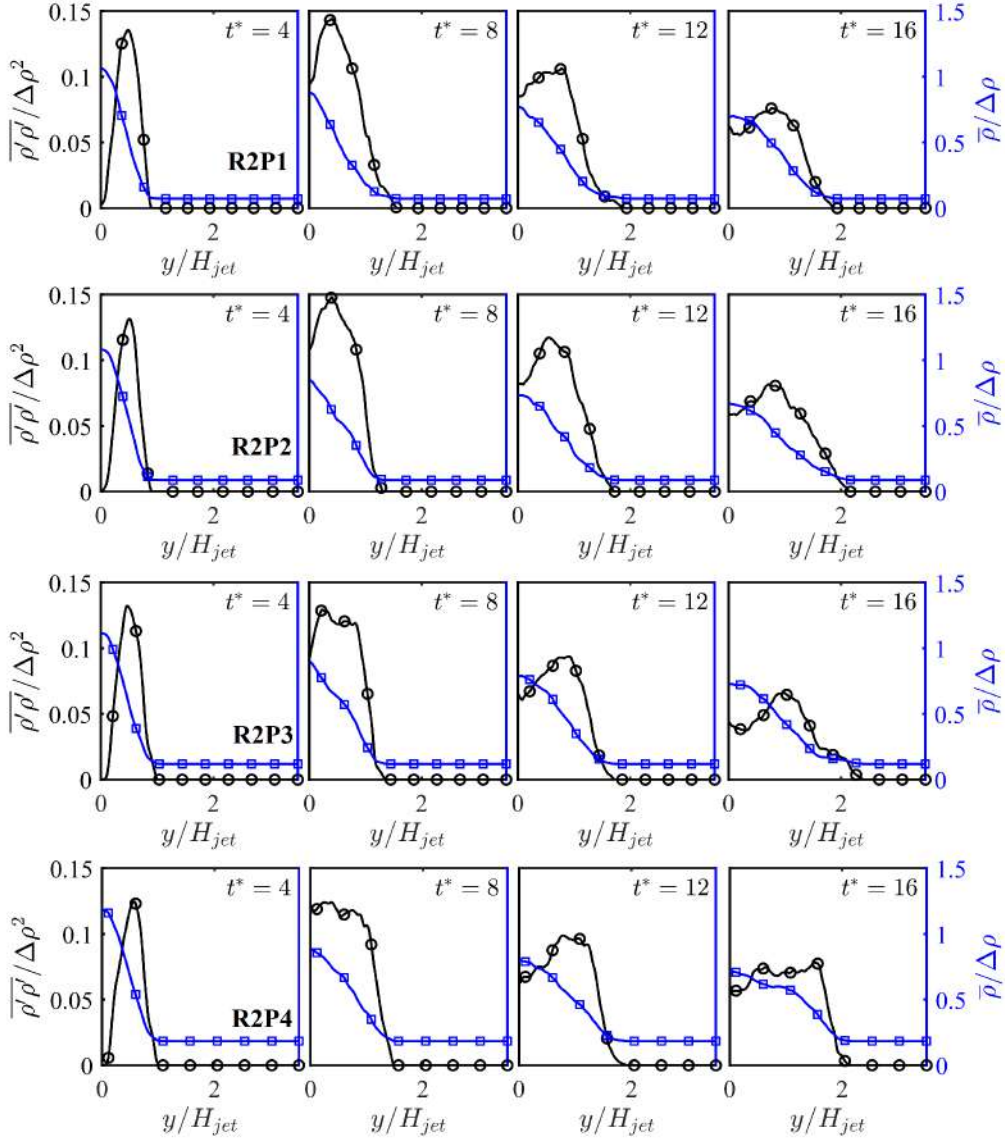


Figure 55: Normalized variance of density $\overline{\rho' \rho'}/\Delta \rho^2$ marked by (○) and normalized $\bar{\rho}$ marked by (□), against cross-wise direction, at four different reduced pressure levels.

While on the other hand, the opposite is true for the non-dimensional enthalpy variance peaks ($\overline{\xi' \xi'}/\Delta \xi^2$)_{max}, the peak value is maximum for the highest reduced pressure R2P4, suggesting comparatively more intense mixing at elevated pressures.

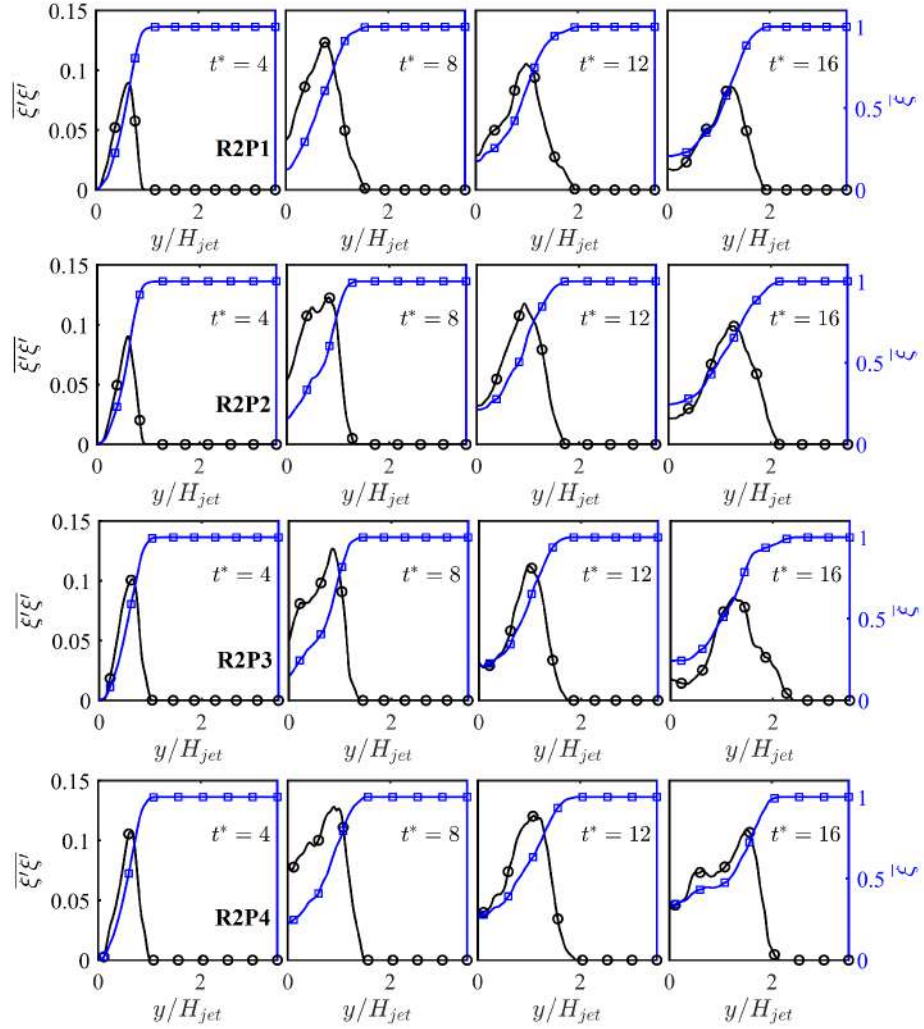


Figure 56: Variance of non-dimensional enthalpy $\overline{\xi' \xi'}$ marked by (\circ) and average enthalpy $\bar{\xi}$ marked by (\square) , against cross-wise direction, at four different reduced pressure levels.

4.4 MODELLING

The processes such as turbulent non-premixed combustion is not as straight forward as the laminar case, demanding more careful averaging and modelling, due to the fact that, the density gradient and heat generation in reacting flow causes varying density in the flow and fluctuating density due to turbulence. For instance, the linear relationship between the species mass fractions and mixture fraction relate to instantaneous mixture fraction ξ and not to $\bar{\xi}$, this is also true for temperature-enthalpy relationship. To compute mean values of \bar{Y}_i and \bar{T} , we need to know the statistics of the variables (T, Y_i, ρ) as a function of mixture fraction ξ , which for now is the fluctuating scalar. Thus, in such context, probability density function (p.d.f.) method is employed.

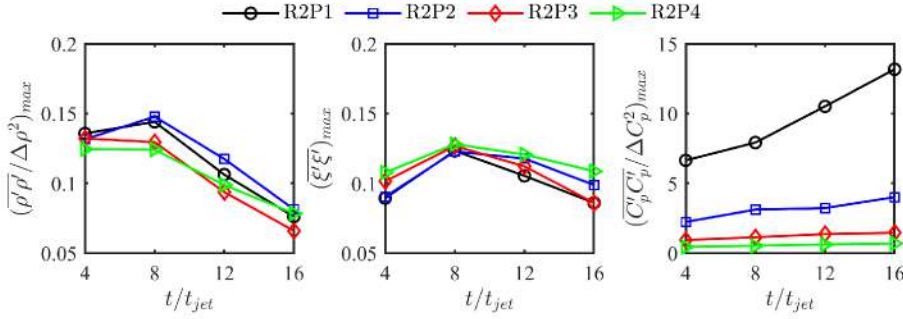


Figure 57: The peaks of the normalized variance of ρ , ξ and C_p at four different reduced pressure levels.

4.4.1 Probability density function (pdf) approach

Due to considerably large thermodynamic variations occurring in the trans-critical injection, even being non-reactive flow, the modelling has to carefully dealt. Typically, the RANS and LES formulation employ averaged and filtered thermodynamic and transport values respectively. If their exists linear dependencies between the thermodynamic/transport properties (say θ) and the integrated variables (say ϕ), one can approximated and simplify the dependencies with so called *No-Model Approximation* as;

$$\bar{\theta}(\phi) \approx \theta(\bar{\phi}) \quad (97)$$

However, in the presence of high non-linearity such as in transcritical injection, such approximation can result to large error, which depends on the grid or filter dimension Δ_{filter} [53, Lapenna,P.E., 2016]. Therefore, the p.d.f approach is classically used in determination of the statistical averages or mean of the state variables in a more accurate fashion, and is popularly used in turbulent combustion modelling. If we consider a random variable ϕ , the probability function $\mathcal{F}_\phi(\psi)$ is defined as

$$\mathcal{F}_\phi(\psi) = Prob\{\phi < \psi\} \quad (98)$$

where $Prob\{\phi < \psi\}$ is the probability that ϕ is less than given value of ψ . The probability function $\mathcal{P}_\phi(\psi)$ is defined as the derivative of the distribution function $\mathcal{F}_\phi(\psi)$ as

$$\mathcal{P}_\phi(\psi) = \frac{d\mathcal{F}_\phi(\psi)}{d\psi} \quad (99)$$

The p.d.f. $\mathcal{P}_\phi(\psi) \geq 0$ and $\int_{-\infty}^{\infty} \mathcal{P}_\phi(\psi) d\psi = 1$. Such p.d.f can then be used to calculate the mean of any property, say the density-weighted (Favre average) of a scalar quantity, mass fraction of species i Y_i which is function of mixture fraction ξ ;

$$\tilde{Y}_k = \int_0^1 Y_k(\xi) \tilde{\mathcal{P}}(\xi) d(\xi) \quad (100)$$

In a generic notation with ϕ^* as the sample space of the generic variable ϕ ;

$$\bar{\theta}(\phi(x, t), x, t) = \int_0^1 \theta(\phi|_{\phi^*}) \mathcal{P}(\phi^*; x, t) d\phi^* \quad (101)$$

Therefore, the integration Equation 100 is enough to obtain the favre averaged mass fraction of the species, for that we need to know the p.d.f. $\tilde{P}(\xi)$, which varies along the location and type of flows.

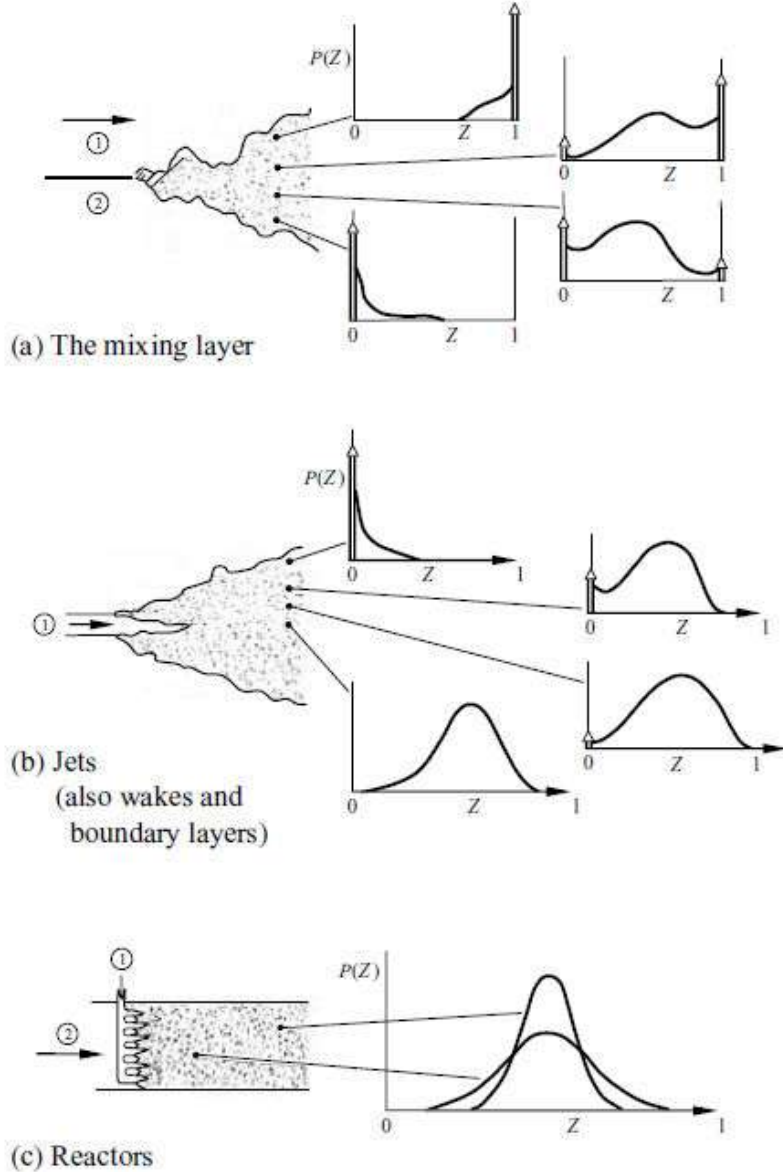


Figure 58: Probability density function forms for a conserved scalar in various types of flow [17, Law,C.K., 2012].

4.4.2 Statistics and SGS Modelling

Various analytical pdfs have been used to approximate the measured distributions, but the clipped Gaussian and beta-functions have been most successful [37, Malasekera,H.K. et al., 2005]. The betas pdf is currently the

most popular among combustion community in CFD codes. The beta pdf (β -pdf) is defined as;

$$\tilde{P}(\phi) = \frac{\phi^{\alpha-1}(1-\phi)^{\beta-1}\Gamma(\alpha+\beta)}{\Gamma(\alpha)\Gamma(\beta)} \quad (102)$$

Where Γ denotes the gamma function, the shape of the β -pdf depends on the values of parameters $\alpha > 0$ and $\beta > 0$, varying these values, one can vary the pdf. The value of α and β can be determined from the mean and variance of variable ϕ as;

$$\alpha = \tilde{\phi} \left[\frac{\tilde{\phi}(1-\tilde{\phi})}{\tilde{\phi}''^2} - 1 \right] \quad (103)$$

$$\beta = (1-\tilde{\phi}) \frac{\alpha}{\tilde{\phi}} \quad (104)$$

Where $\tilde{\phi}$ and $\tilde{\phi}''^2$ are the favre mean and favre-averaged variance of ϕ . It is

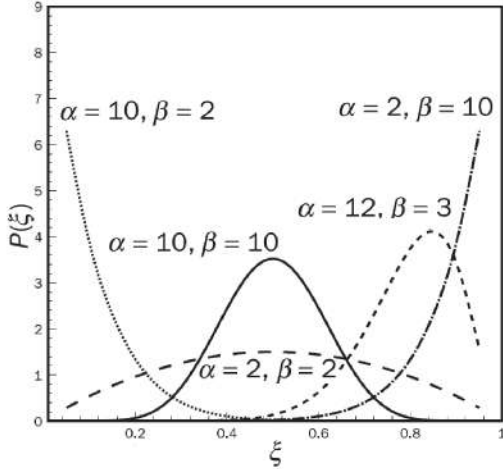


Figure 59: The behaviour of β -pdf function (as a function of a variable ξ) for different values of α and β [37, Malasekara,H.K., et al., 2012].

noticeable in Figure 59 that, the distribution function approaches that of a Gaussian for large values of α and β together, and hence small values of mean $\tilde{\phi}$ and variance $\tilde{\phi}''^2$. Similarly, singularity is hit at very large values of either α or β . The exact pdf profile $\mathcal{P}(\phi^*; x, t)$ is not available in case of RANS or LES, but can be computed from DNS dataset. For LES or RANS, it requires pre-assumption based on available statistical parameters of the variable ϕ i.e. its mean and the variance [53, Lapenna,P.E., 2016]. Thus, this type of computation is sometimes called *presumed pdf approach*.

$$\mathcal{P}(\phi^*; x, t) \approx \mathcal{P}(\phi^*; \bar{\phi}(x, t), \overline{\phi''\phi''}(x, t)) \quad (105)$$

A numerical difficulty is encountered when the values of α and β in Equation 104 approaches magnitudes of several hundred thousand in the iteration process [15, Chen,C.- S, et al., 1994], which leads to overflow in the calculation of $\tilde{P}(\phi)$. To avoid such overflow when the values of either α or β (say above

500), we approximate $\tilde{\mathcal{P}}(\phi)$ by a *Delta-function*: $\tilde{\mathcal{P}}(\phi) = \delta(\phi - \tilde{\phi})$. The density weighted mean $\tilde{\theta}$ of a scalar flow variable θ is now given as:

$$\tilde{\theta}(\phi) = \int_0^1 \theta(\phi) \tilde{\mathcal{P}}(\phi) d\phi \quad (106)$$

$$= \int_0^1 \theta(\phi) \delta(\phi - \tilde{\phi}) d\phi \quad (107)$$

$$= \theta(\tilde{\phi}) \quad (108)$$

which is nothing but the same as *no-model assumption* in favre sense, i.e.

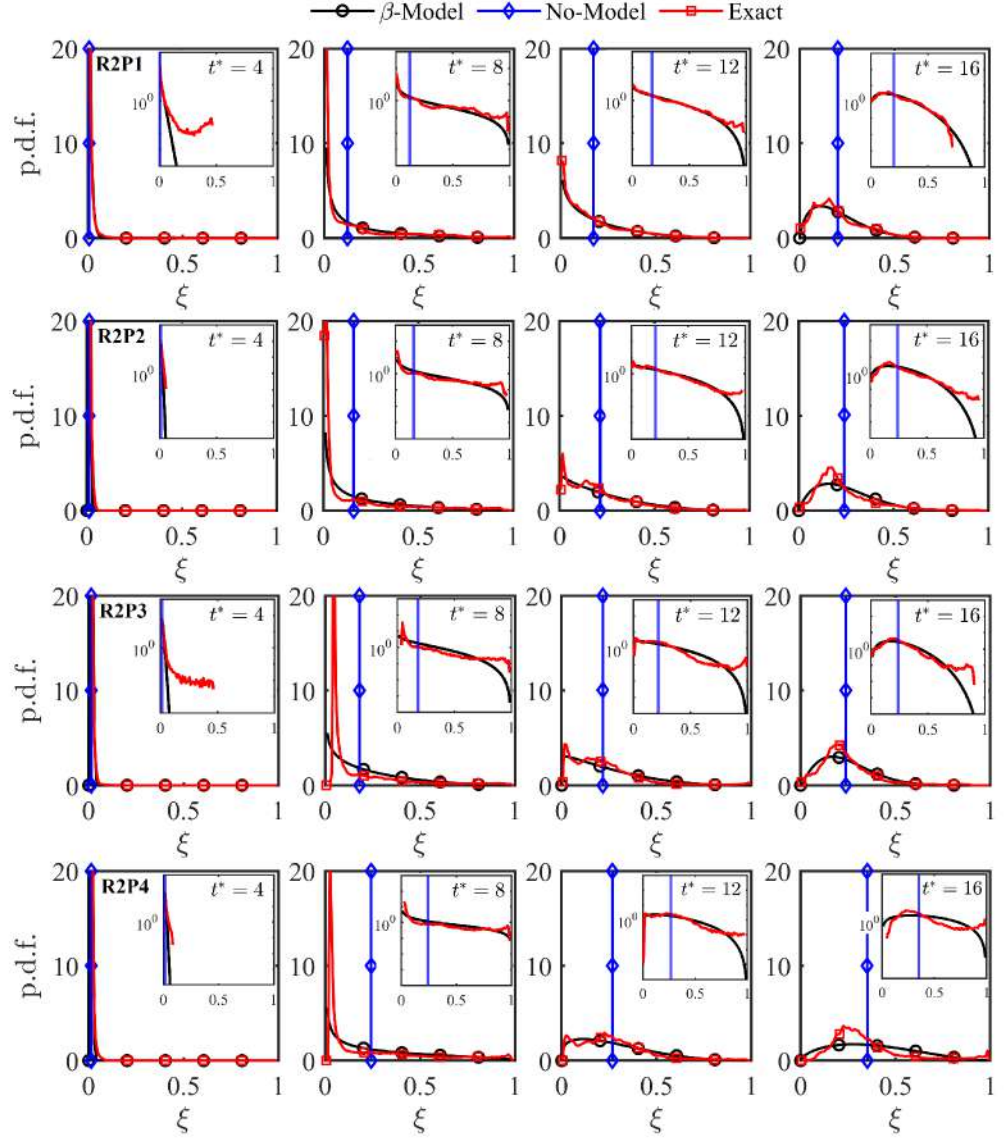


Figure 60: Non-dimensional enthalpy ξ pdf at 4-different reduced pressure levels and respective 4-time instances, with additional subplot in semi-logarithmic scale, computed at $y/H_{jet} = 0$.

equation 97, completely neglects the sub-grid scalar fluctuations. Such an assumption has a serious limitation for transcritical injection and supercritical

mixing process explored in the present work due to strong non-linearities of thermodynamic and transport properties. The statistical analysis of temporal jet along its central axis along evolving time simulation is analogues to spatially evolving jet performed along the jet axis [54, Lapenna,P.E. & Creta,F., 2017].

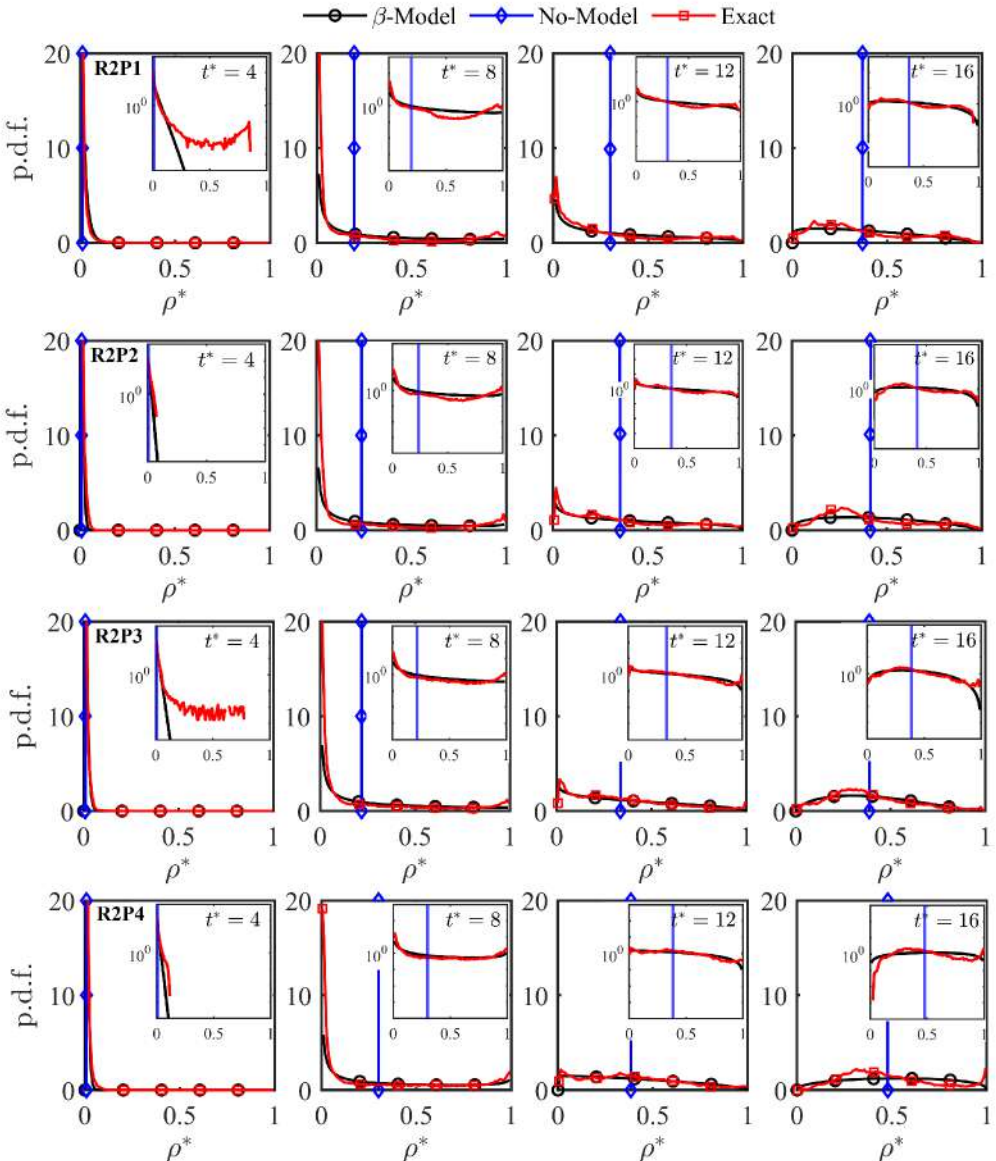


Figure 61: Non-dimensional density ρ^* pdf at 4-different reduced pressure levels and respective 4-time instances, with additional subplot in semi-logarithmic scale, computed at $y/H_{jet} = 0$.

The pdf study along the jet central line i.e. $y/H_{jet} = 0$ can be carried out for thermodynamic variables such as non-dimensional enthalpy ξ , density ρ^* , isobaric specific heat capacity C_p^* , and Prandtl number Pr^* . The comparison among *exact pdf*; obtained from the DNS data. β -*pdf*; computed with the mean and variance and *Dirac-delta*; which is nothing but the no-

model approximation equation 108 or 97, has been made. The subplot in semi-logarithmic scale for each study, is for better visualization. Figure 60

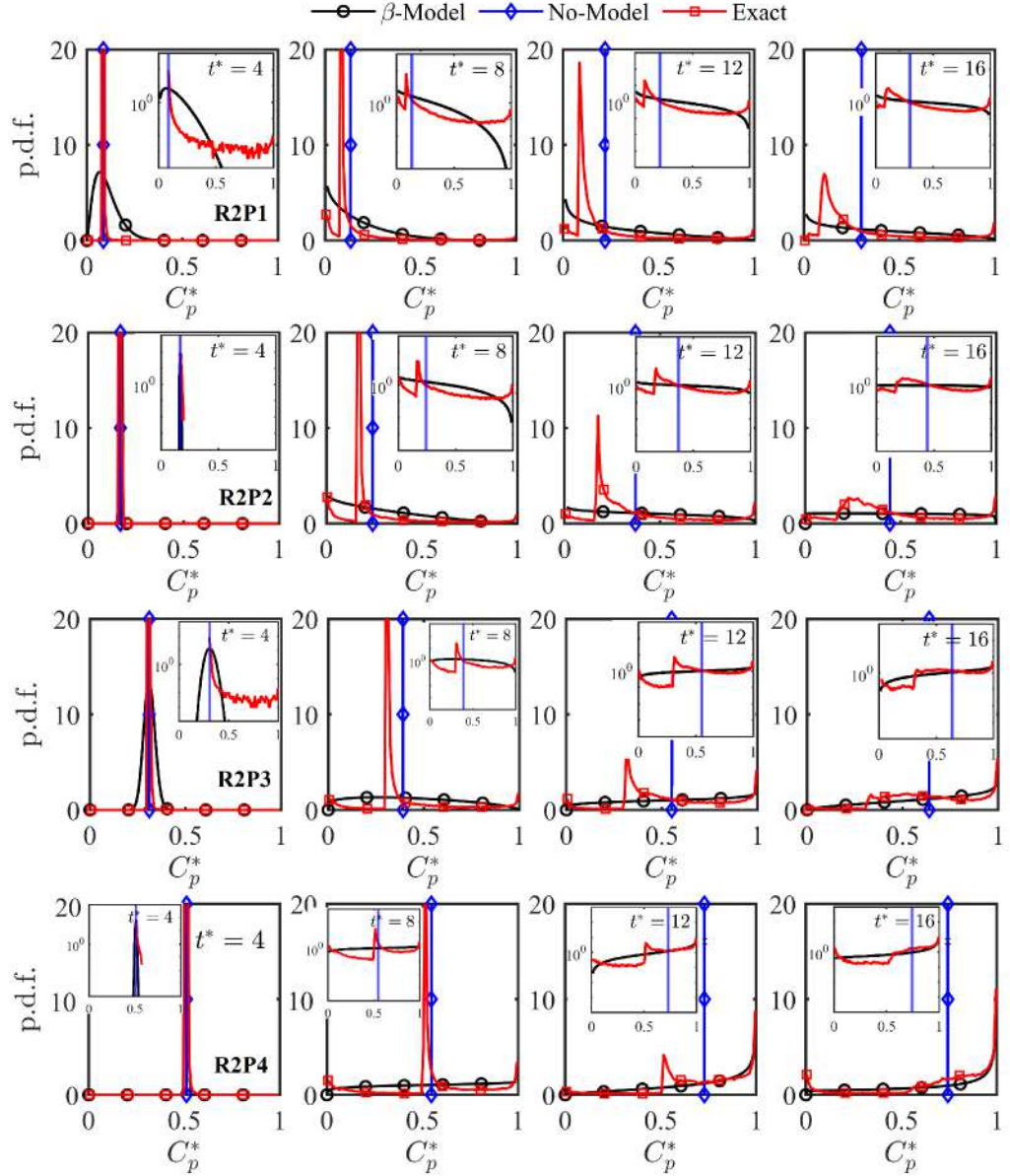


Figure 62: Non-dimensional isobaric specific heat capacity C_p^* pdf at 4-different reduced pressure levels and respective 4-time instances, with additional subplot in semi-logarithmic scale, computed at $y/H_{jet} = 0$.

shows the comparison of non-dimensional enthalpy $\xi = (h - h_{jet}) / (h_{env} - h_{jet})$ ($\epsilon \in [0, 1]$; cold jet: $\xi = 0$, $T = 100 K$ and warm environment: $\xi = 1$, $T = 300 K$). Since the β function is dependent on the mean and variance, it's accuracy in describing the DNS (exact) pdf can be understood with the help of Figure 56. The variance $\overline{\xi' \xi'}$ in this case range from about 0.001 to 0.14. It has been reported in the literature [83, Wang,X., Yang,V. et al., 2018], [53, 54, Lapenna, P.E., & Creta,F., et al., 2016, 2017] that, β -function distribution can accurately describe the pdf of the DNS data at low variance but deviates

at higher variance.

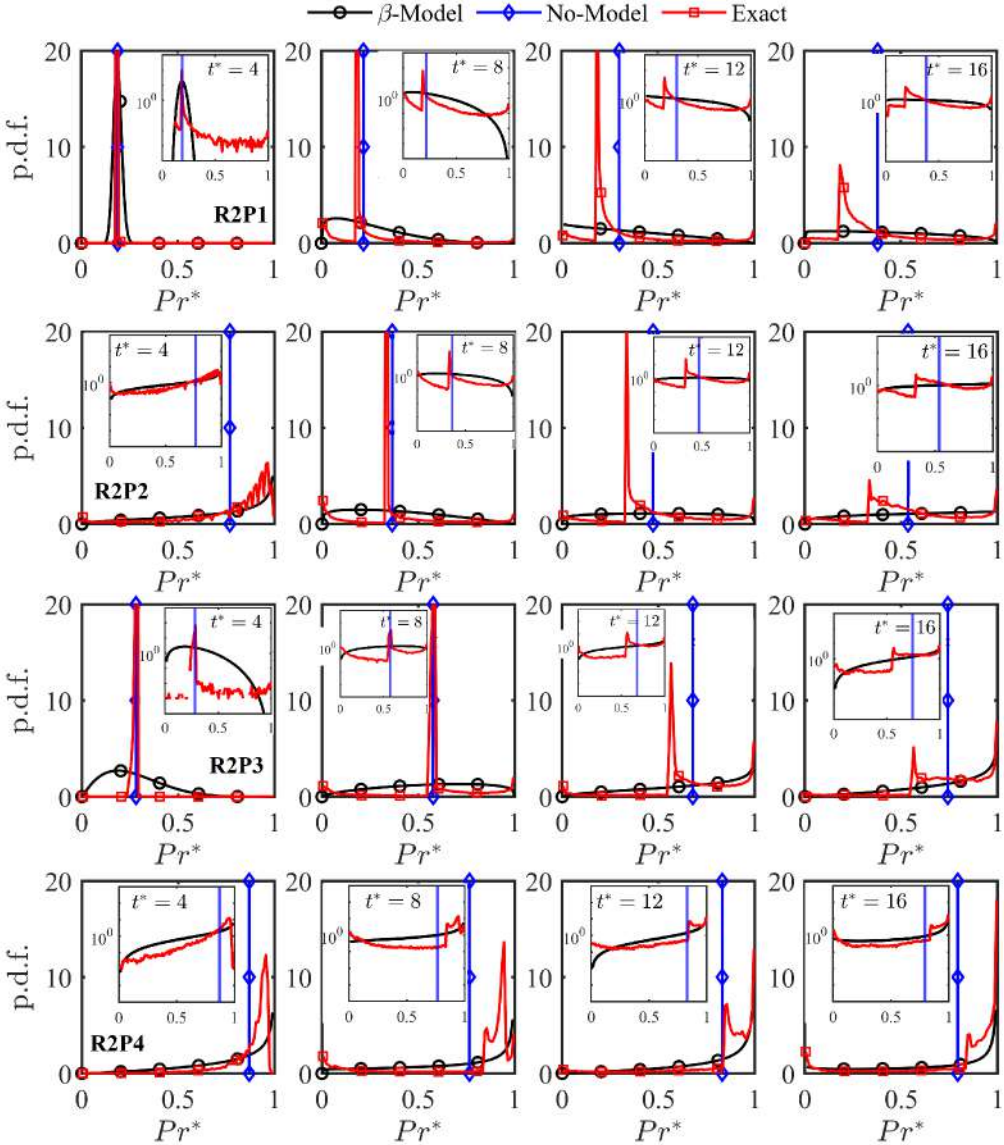


Figure 63: Prandtl number Pr^* pdf at 4-different reduced pressure levels and respective 4-time instances, with additional subplot in semi-logarithmic scale, computed at $y/H_{jet} = 0$.

It is very much noticeable in the pdf study of ρ^* and ξ (see Figure 61 and 60, respectively), that the Dirac-delta function accurately describes the exact pdf for the first time instance $t/t_{jet} = 4$, where the variance is considerably low. While, the second time instance $t/t_{jet} = 8$ is dominated by the growth of large scale KH structures giving raise to variance, and therefore the β -function tend to deviate quite a bit like in the case of R2P3 and R2P4, while the last time instance $t/t_{jet} = 16$ is characterized by higher variance due to the fact that the mixing is very much prevalent in that time instant, which is also

equivalent to farthest downstream in the spatially evolving jet.

Figure 61 shows the similar comparison of the non-dimensional density ρ^* by its maximum value in the simulation and the similar is true for the case of non-dimensional isobaric specific heat capacity C_p^* ; Figure 62 and Prandtl number Pr^* ; Figure 63.

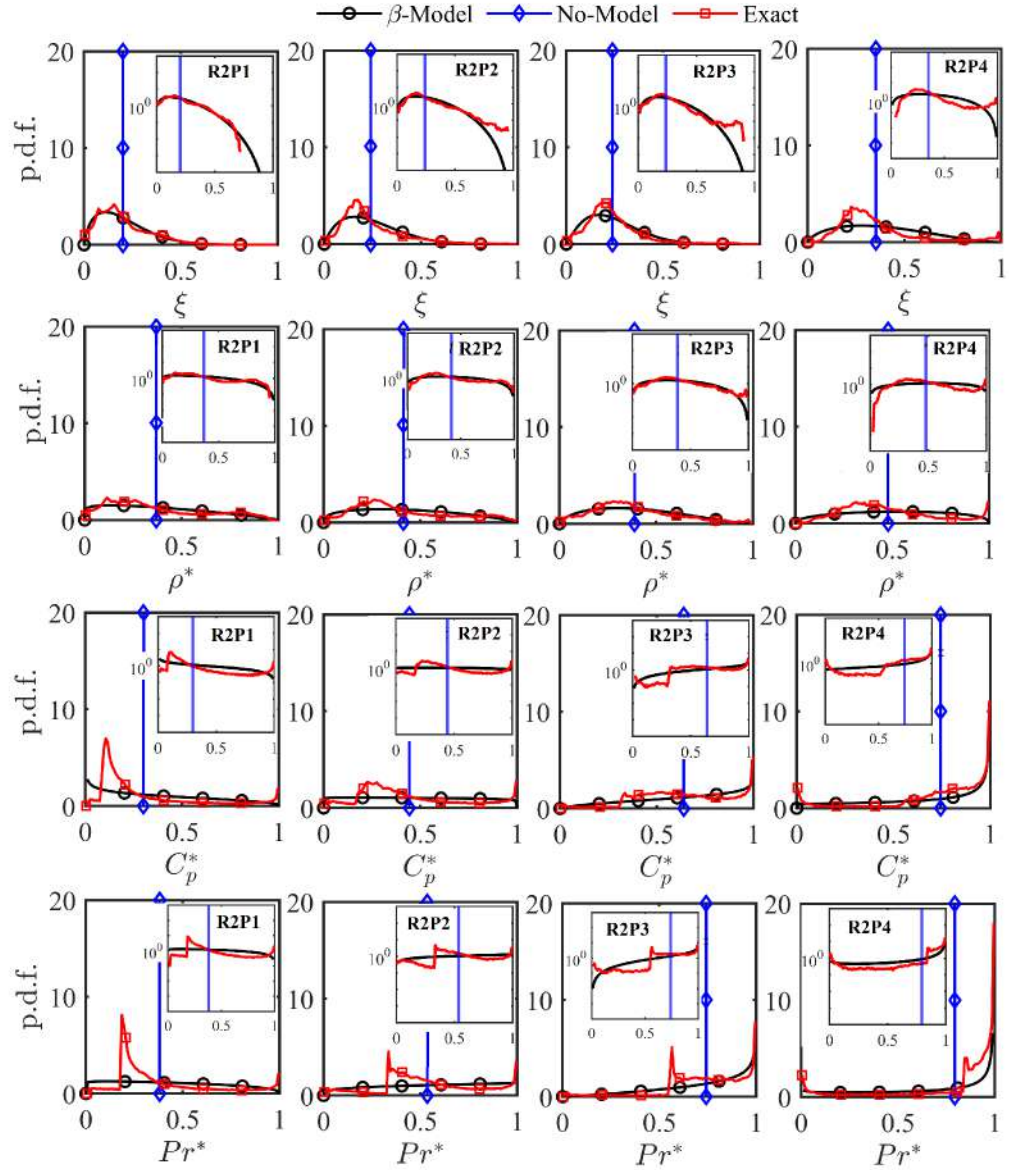


Figure 64: The non-dimensional enthalpy ξ , density ρ^* , isobaric heat capacity C_p^* and Prandtl number Pr^* pdf at 4-different reduced pressure levels, with additional subplot in semi-logarithmic scale, computed at $y/H_{jet} = 16$.

The β -function accuracy to describe the exact-pdf can be tested intensively with the C_p^* profiles because the C_p is characterized by considerably high value of variance especially in near-to-critical regime (case R2P1), see Figure

48 and 57. This should cause disagreement among the exact- and beta- pdfs, as one can observe in Figure 62, especially in the case of R2P1, the strong disagreement in the second time instant $t/t_{jet} = 8$ is due to the presence of large scale KH structures. Since, Prandtl number behaves similar to the isobaric heat capacity, it suffers the similar effect as that of C_p^* .

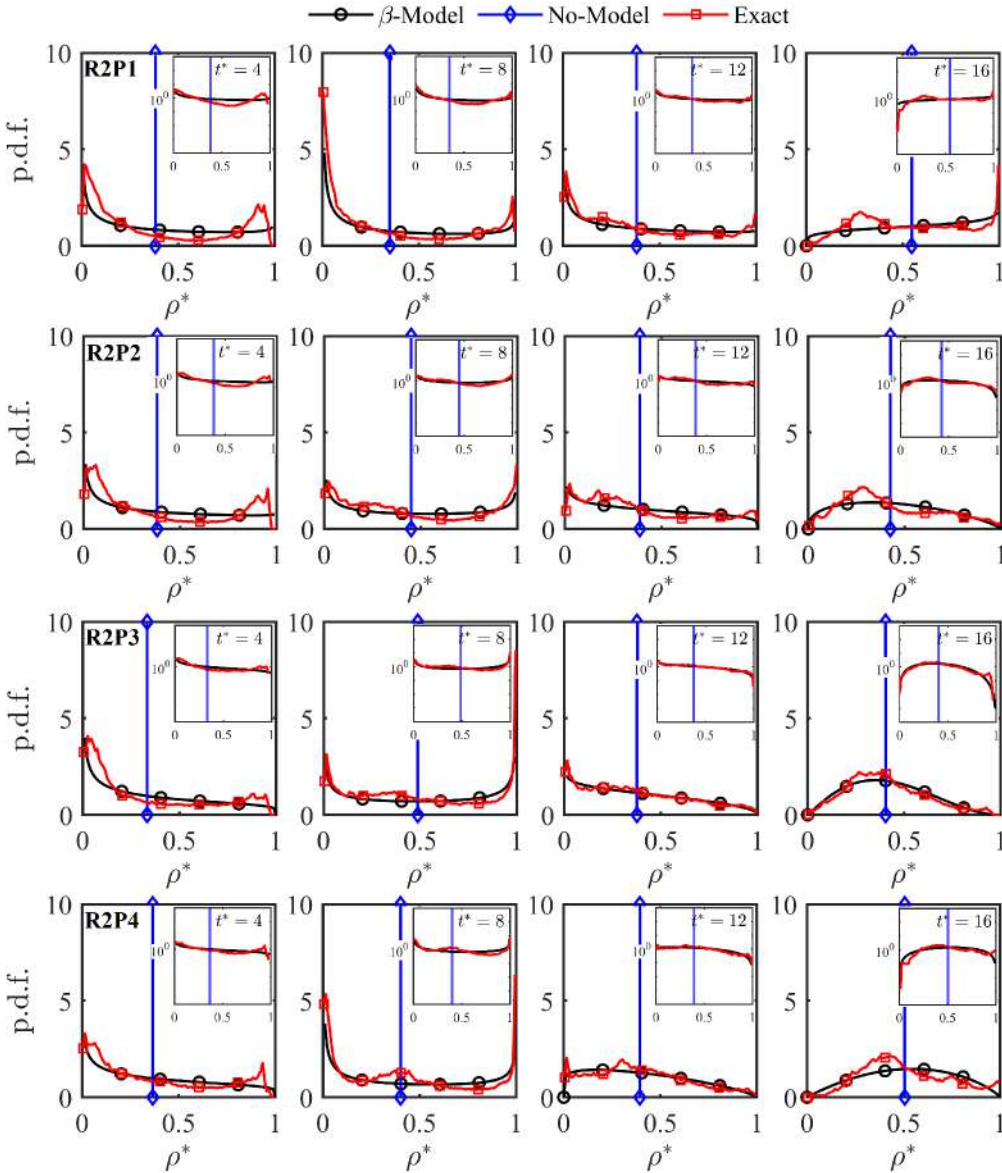


Figure 65: Non-dimensional density ρ^* pdf at 4-different reduced pressure levels and respective 4-time instances, with additional subplot in semi-logarithmic scale, computed at $y/H_{jet} = pb$.

The pressure dependencies on the pdf predictions for the last time instance $/t_{jet} = 16$ can be studied with Figure 64. A careful observation on the enthalpy profile shows that, strong disagreement between β and exact pdf distribution exists in R2P4. The β function usually seem to underestimate

the peaks, which is even more sever for higher variance cases, which is consistent to [83, Wang,X., Yang,V. *et al.*, 2018] findings. The other noticeable disagreement is in C_p^* and Pr^* ; R2P1 which is due to strong thermodynamic non-linearities which β - function clearly cannot appreciate.

Other than, jet centerline $y/H_{jet} = 0$, possible location of an interest could be the region of highest thermo-physical change i.e. in the shear/mixing region undergoing the pseudo-vaporization process $y/H_{jet} = pb$. This region is characterized by high label of variance, therefore, it is expected to have disagreement between beta-function and the exact-pdf. This is very evident in Figure 65. Some peculiar features such as the presences of U-shaped exact pdf at the second time instant $t/t_{jet} = 8$ is noticeable due to the fact that the large scale KH structures causes entrainments leading to considerably large value of mean as well as variance. Additional, *Gaussian-like* distribution is also noticeable in $t/t_{jet} = 8$ R2P4. As previously discussed and in also this case, the β -distribution also show poor performance with exact-pdf, while underestimating the peaks, in the mixing dominant time instance $t/t_{jet} = 16$.

Furthermore, since the β pdf and dirac delta has been generated, we can now look at the spatial evolution of properties like $C_p(\xi(y,t), y, t)$ and $\rho(\xi(y,t), y, t)$ with a concept of computing mean or filtered value as in equation 101. The mean or filtered quantity so obtained can be expressed as;

$$\bar{\rho}(\xi(y,t), y, t) = \int_0^1 \rho(\xi|\xi^*) \mathcal{P}(\xi^*; y, t) d\xi^* \quad (109)$$

$$\overline{C}_p(\xi(y,t), y, t) = \int_0^1 C_p(\xi|\xi^*) \mathcal{P}(\xi^*; y, t) d\xi^* \quad (110)$$

Where, ξ^* the sample space value of ξ during pdf computation. Note that, C_p and ρ depend on the non-dimensional enthalpy ξ (or non-dimensional temperature θ) and on background pressure p_0 . The value of $\rho(\xi|\xi^*)$ and $C_p(\xi|\xi^*)$ are nothing but the laminar profiles (see Figure 36b and 36a respectively). Let us recall the three definitions used to compute the averages; Since the

Name	Approach
Exact	pdf $\mathcal{P}(\xi \xi^*; y, t)$, is extracted from DNS data
β - model	pdf $\mathcal{P}(\xi \xi^*; y, t)$, is constructed with mean $\bar{\xi}$ and variance $\bar{\xi}'\bar{\xi}'$ obtained from the DNS data
No- model	pdf is assumed to be Dirac-delta at $\bar{\xi}$ of DNS data equation 97

Table 16: Three approaches used to obtain the mean or filtered values along cross wise direction in the present work.

focus of the study in the mixing process, the relevant time instances are $t/t_{jet} = 12$ and 16 . To study the influence of pressure on spatial evolution of thermodynamic variable predicted by the above mentioned approaches,

all four reduced pressure values are considered. The result for third time instant $t/t_{jet} = 8$ and fourth time instant $t/t_{jet} = 16$ are shown in figure 66 and 67 respectively.

The results show that, there exist good agreement among the β -model (\bullet), no-model (\triangle) and exact/DNS (\star); see figure 66 and 67, in the region with no disturbance (until $y/H_{jet} \approx 2$). Thereafter, the no-model behaviour shows significant contradiction to exact average of the DNS data. In early stage of the variation, both no-model and beta-model seem to underestimate the exact value, the former seem to underestimate even more. As, the region of pseudo-vaporization is approached ($y/H_{jet} \approx 0.5$), the no-model totally fails to do its job and over estimates the exact value by several folds. This gives high inaccuracy, totally away from the real behaviour of the thermodynamic variables, used in the RANS/LES framework.

Figure 66 shows the averages of isobaric heat capacity \bar{C}_p and the density $\bar{\rho}$. Previously mentioned disagreement among no-model and exact is even severe for R2P1. It has been pointed out that, the no-model approach doesn't have enough information about the SGS fluctuations of the stochastic variables, but just have limited information about its mean [53, 54, Lapenna,P.E. & Creta,F., 2016, 2017]. They also showed that, the large errors due to lack modelling of SGS fluctuations can be as high as 250 %, especially in the pseudo-boiling region as ξ tends to ξ_{pb} . This can be clearly, seen in the \bar{C}_p figure 66- left column and figure 67- left column. The large fluctuations encountered during the pseudo-boiling process in R2P1 leads to largest divergence/overestimation with \bar{C}_p peaking upto ≈ 14 and it reduces significantly to match the exact DNS value in the core region with now variance level.

4.5 REYNOLDS STRESS AND TURBULENT HEAT FLUX

4.5.1 *Reynolds stress*

Reynolds stress is a second order symmetric tensor, which arises along with viscous stress in RANS equation from the turbulent transport of momentum. These stresses lead to additional deformation of fluid parcel. Reynolds stresses are those contributing to the unclosed terms (unknowns values which cannot be computed directly due to lack of measures of fluctuating fields) in the Navier-stokes equation and therefore, demands closure to the problem, which is also popularly known as the Closure Problem, i.e. somehow it is necessary to express Reynolds stress as function of mean quantities. One of the solution to such problem is eddy viscosity closure model. Reynolds stress (appearing in the momentum equation) are initially due to the convective momentum exchanges due to turbulent velocity fluctuations. The fluctuating velocity field in turbulence attribute to convective momentum exchange and therefore, to the Reynold stress. Fluid particles carry away the momentum in the process of mixing and thus, the Reynolds stress too

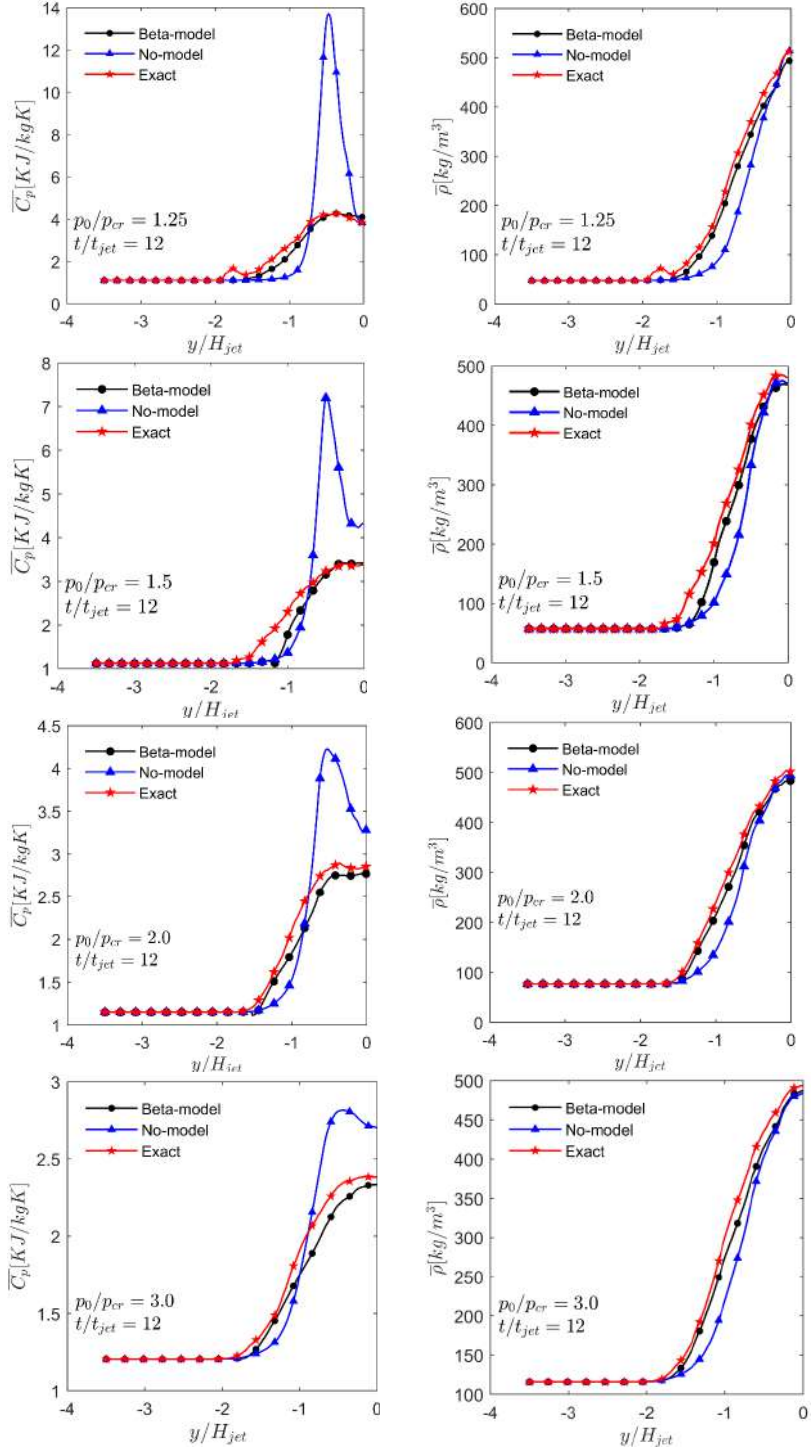


Figure 66: The average thermodynamic properties \bar{C}_p (left column) and $\bar{\rho}$ (right column) computed along the cross-wise direction $Y - axis$ at $t/t_{jet} = 12$, for various reduced pressure levels, with three different approaches (see Table ??).

are carried along. Turbulent fluctuations contribute to and always have 3-dimensional spatial character, where the rotational flow structures consist

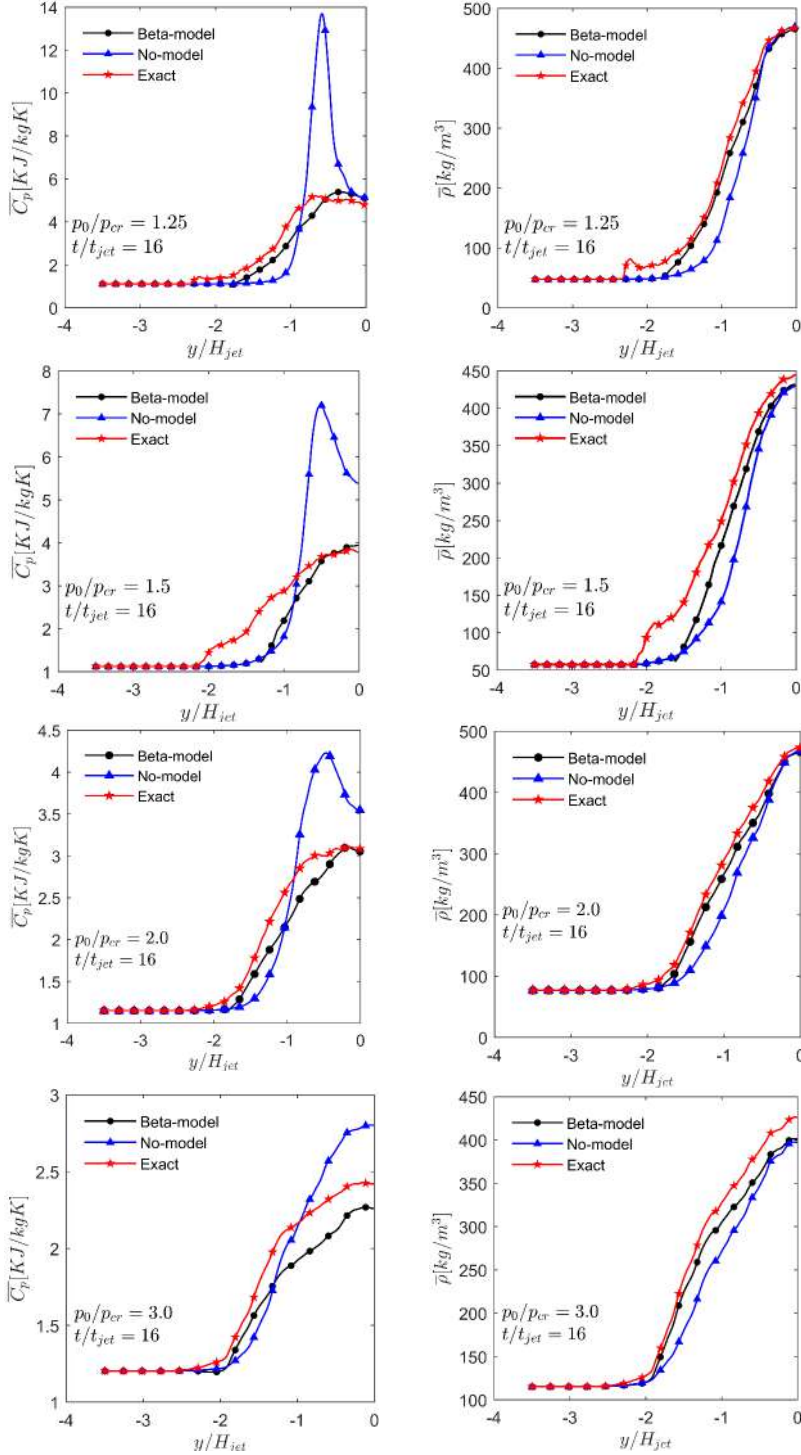


Figure 67: The average thermodynamic properties \bar{C}_p (left column) and $\bar{\rho}$ (right column) computed along the cross-wise direction $Y - axis$ at $t/t_{jet} = 16$, for various reduced pressure levels, with three different approaches (see Table ??).

wide range of length and time scales [37, Malasekara,H.K., et al., 2005].

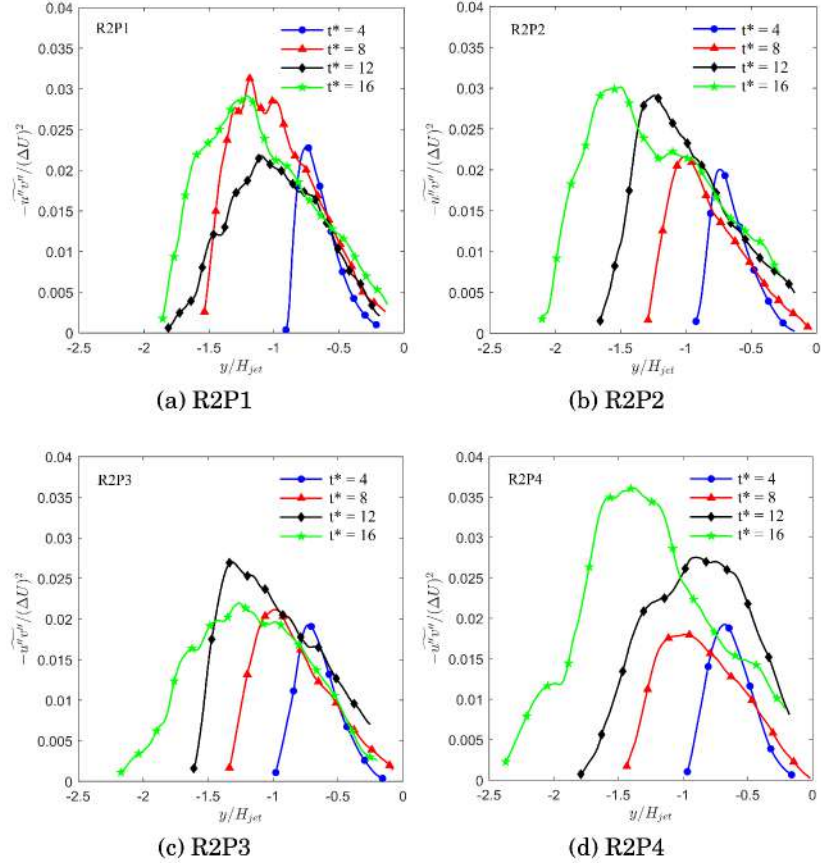


Figure 68: The Reynolds stress normalized by squared mean shear computed for all reduced pressure level for all time instances $t/t_{jet} = t^*$.

In our case of temporally evolving jet, the initial evolving jet consists of 2-dimensional turbulent structures which grow over time while extracting energy from the the mean flow. Such growing Kelvin-Helmholtz vortices trigger instability allowing mixing process to begin. However, pressure has a role to play along, i.e. considerable confinement of mixing layer width can be observed in the case of near-critical pressure (referring to the Figure 68a, the last time instant-green plot), the mixing is limited to a value close to $y/H_{jet} = 2$, while the mixing width gradually increases as pressure is elevated to supercritical regime upto around $y/H_{jet} = 2.5$. The large Kelvin-Helmholtz vortices with most of the energy content in the energy spectrum is evident in the second time instant (Figure: 68a red line in top-left plot), which is also associated with comparatively high value of Reynolds stress in the near-critical pressure.

4.5.2 Turbulent heat flux

Strong thermo-physical property variations encountered in the supercritical pressure fluid has an influence on the heat transfer mechanism of the fluid. Turbulent convective heat transfer to supercritical fluid is strong affected

by such variations in the region near critical point [61, Pizzarelli,M., 2018]. The diffusion of heat (both due to molecular and turbulent) can be strongly affected by significant variations in thermo-physical properties. Th density stratification can affect the turbulent production, in addition to it the sharp variations in C_p and k may have significant consequences in the heat transfer effectiveness [85, Yoo,J.Y., 2013]. Near critical and pseudo-critical points maximum value of the convective heat-transfer coefficient is due to significant variations in thermo-physical properties of the fluid as pointed out by [84, Yamagata,K. et al., 1972].

The rise in the turbulent heat flux is accompanied by the raise in specific heat at constant pressure, a signature of pseudo vaporization, which provides an evidence of their relationship. The turbulent heat flux raises with due as the mixing process process.

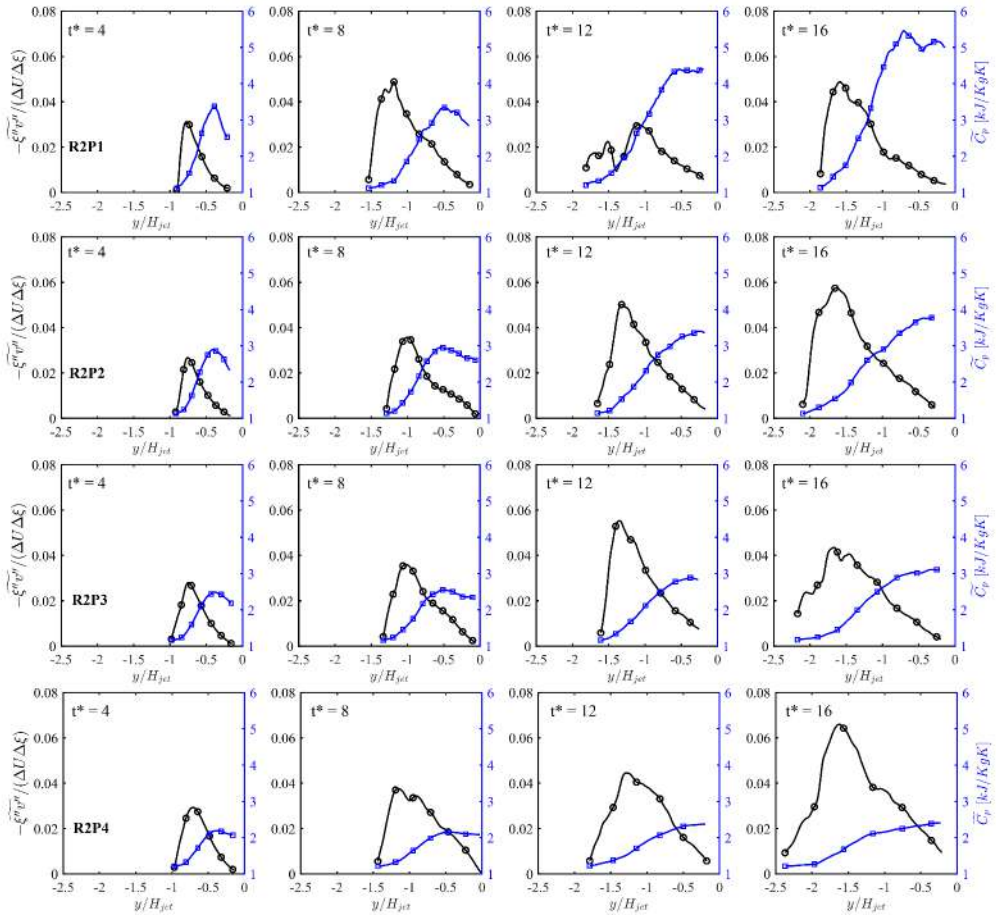


Figure 69: The turbulent heat flux normalized by the product of enthalpy and mean shear computed for at all reduced pressure level for all time instances $t/t_{jet} = t^*$.

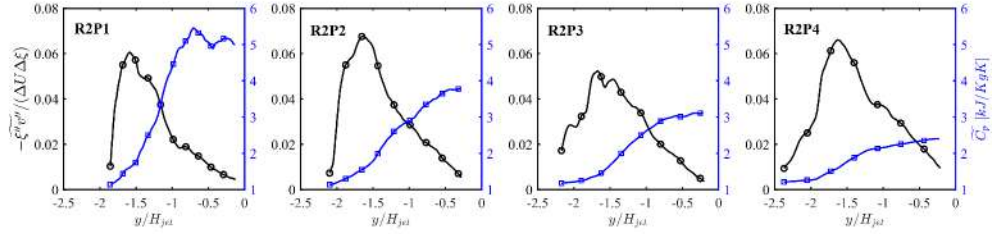


Figure 70: Turbulent heat flux at the last time instant $t/t_{jet} = 16$, for all 4-reduced pressure levels.

4.5.3 *Turbulent Prandtl number*

The heat transfer is related to the fluid flow by Prandtl number [77, Tiam,R., et al., 2018], a ratio between momentum diffusivity and heat transfer diffusivity. The turbulent Prandtl number Pr_t accounts for turbulence contribution to the energy transfer. The fluids at supercritical pressures with strong thermo-physical properties variation, most common approximation of $Pr_t = 1$ is questionable. The turbulent heat flux vector q_t , is usually modelled with the classical analogy [Reynolds (1874)] between momentum and heat transfer, as a closure approximation. In this approximation, the turbulent heat flux q_t is assumed to be proportional to the mean temperature gradient;

$$q_{t_i} = \widetilde{\rho v'' h''} = -\frac{\mu_t C_p \partial \widetilde{T}}{Pr_t \partial y_i} = -\frac{\mu_t \partial \widetilde{h}}{Pr_t \partial y_i} \quad (111)$$

Where Pr_t is the turbulent Prandtl number, which is approximated to be a constant value ranging between 0.5 to 1. However, the simplest model which assumes the momentum diffusivity and heat diffusivity to be the same yields $Pr_t = 1$, known as *Reynolds analogy*. It has been pointed out that, in shock free flows up to low supersonic speeds with low heat transfer rate, the assumption of constant- Pr_t gives good satisfactory result [82, Wilcox,D.C., 2006]. The assumption of the constant value of Pr_t doesn't capture the heat transfer process very well [85, Yoo,J.Y., 2013] due to inadequate turbulent heat flux modelling. Such turbulence models are unable to reproduce the turbulent heat flux recovery. In fact, [77, Tiam,R., et al., 2018] suggested that, for fluids with significant property variations at supercritical pressures, new Pr_t model is required that can show the influence of property variations, and constant Pr_t is unreasonable.

$$Pr_t = \frac{\nu_t}{\alpha_t} \quad (112)$$

$$\nu_t = \frac{-\widetilde{u''v''}}{(\partial \widetilde{u}/\partial y)} \quad (113)$$

$$\alpha_t = \frac{-\widetilde{h''v''}}{\widetilde{C}_p(\partial \widetilde{T}/\partial y)} = \frac{-\widetilde{\xi''v''}}{(\partial \widetilde{\xi}/\partial y)} \quad (114)$$

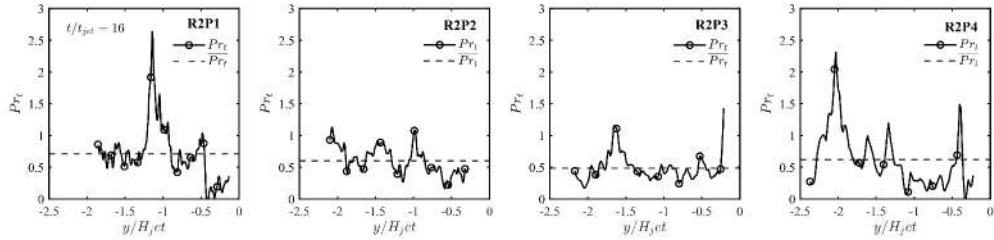


Figure 71: Turbulent Prandtl number Pr_t at the last time instant $t/t_{jet} = 16$, for all 4-reduced pressure levels.

4.6 ANISOTROPY STUDY

Turbulent heat fluxes, which are often modelled with Linear eddy diffusivity hypothesis as [66, Ries,F. et al., 2017]:

$$\widetilde{u''\theta''} = -\alpha_T \nabla_i \widetilde{\theta} \quad (115)$$

Where, i=1,2,3 corresponding to directions along x (streamwise-inhomogeneous), y (crosswise-homogeneous) and z (spanwise-inhomogeneous) respectively. $\widetilde{u''\theta''}$ is the turbulent heat flux vector and is proportional to the corresponding temperature gradient $\nabla_i \widetilde{\theta}$ with turbulent/ eddy diffusivity (α_T) as a constant of proportionality. θ is the non-dimensional temperature. In other words, turbulent transport of a scalar is taken to be proportional to the gradient of the mean value of the transported quantity [37, Malasekara,H.K., et al., 2005]. In our case of study, the anisotropy of the heat flux can be studied as:

$$\widetilde{u''\theta''} = -\alpha_T \nabla_x \widetilde{\theta} \quad (116)$$

$$\widetilde{v''\theta''} = -\alpha_T \nabla_y \widetilde{\theta} \quad (117)$$

$$(118)$$

According to the linear diffusivity hypothesis (from equations 117 and 118):

$$\widetilde{u''\theta''} \nabla_y \widetilde{\theta} = \widetilde{v''\theta''} \nabla_x \widetilde{\theta} \quad (119)$$

The Reynolds number in case of Ries et al.'s analysis is little higher than in our case. Therefore, to have comparative study, the heat fluxes have been divided by injection-jet velocity in both our and Ries et al.'s cases ($U_{inj|Ries} = 0.151 \text{ m/s}$ while in our case $U_{inj|Our} = 0.089 \text{ m/s}$ R2P1 respectively). The reduced pressure of 1.25 is chosen because it's closest to the analysis of Ries et al. ($p_0/p_{cr} = 1.172$). The large value of anisotropy in Ries et al. case (pink diamond) close to injection must be because of the larger value of shear and density gradient as his analysis is with larger Reynold's number and nearer to critical pressure.

It has been pointed out that the cause for anisotropy is shear and the thermodynamics of the fluid flow. Since all four cases are carried out at same

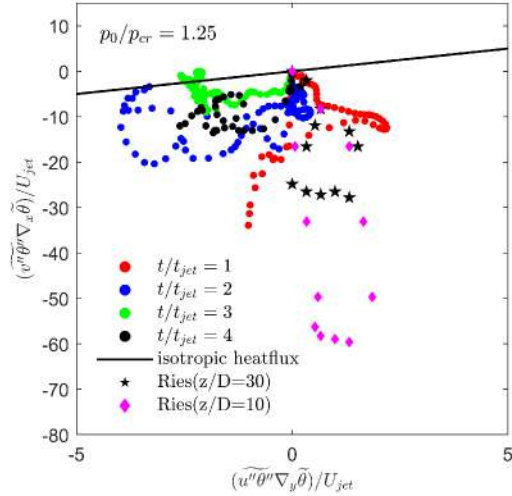


Figure 72: Comparison of anisotropy with that by Ries et al. [66, Ries,F. et al., 2017].

Re it is wiser to study the effect of thermodynamics on anisotropy at by looking at 4 reduced pressure levels. The anisotropy is comparatively high at the first time instant while reduces towards isotropic behaviour as mixing progresses, even though its far away from fully isotropic condition. Steep thermodynamic gradient and non-linearities is expected to have influence on it, and therefore, near-to-critical case (R2P1) is characterize with higher level of anisotropy which is even more evident in figures shown in Figure 74. It has been pointed out by [66, Ries,F. et al., 2017] that the anisotropy is higher for fluids with strong liquid-like character which in our case is at near-to-critical R2P1 (see Figure ??), and thus demand for tensorial heat diffusivity models/extended heat flux/SGS heat flux model (which also accounts for SGS heat flux in terms of large scale strain-rate tensor and temperature gradient [60, Peng,S.H. et al., 2002]) over linear eddy diffusivity model.

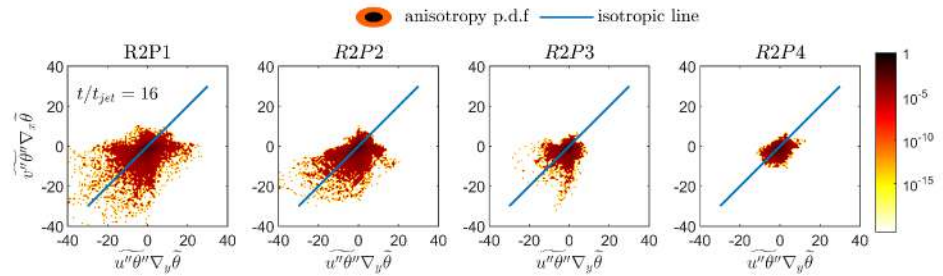


Figure 73: Joint pdf of anisotropy at 4-reduced pressure levels and last time instant $t/t_{jet} = 16$.

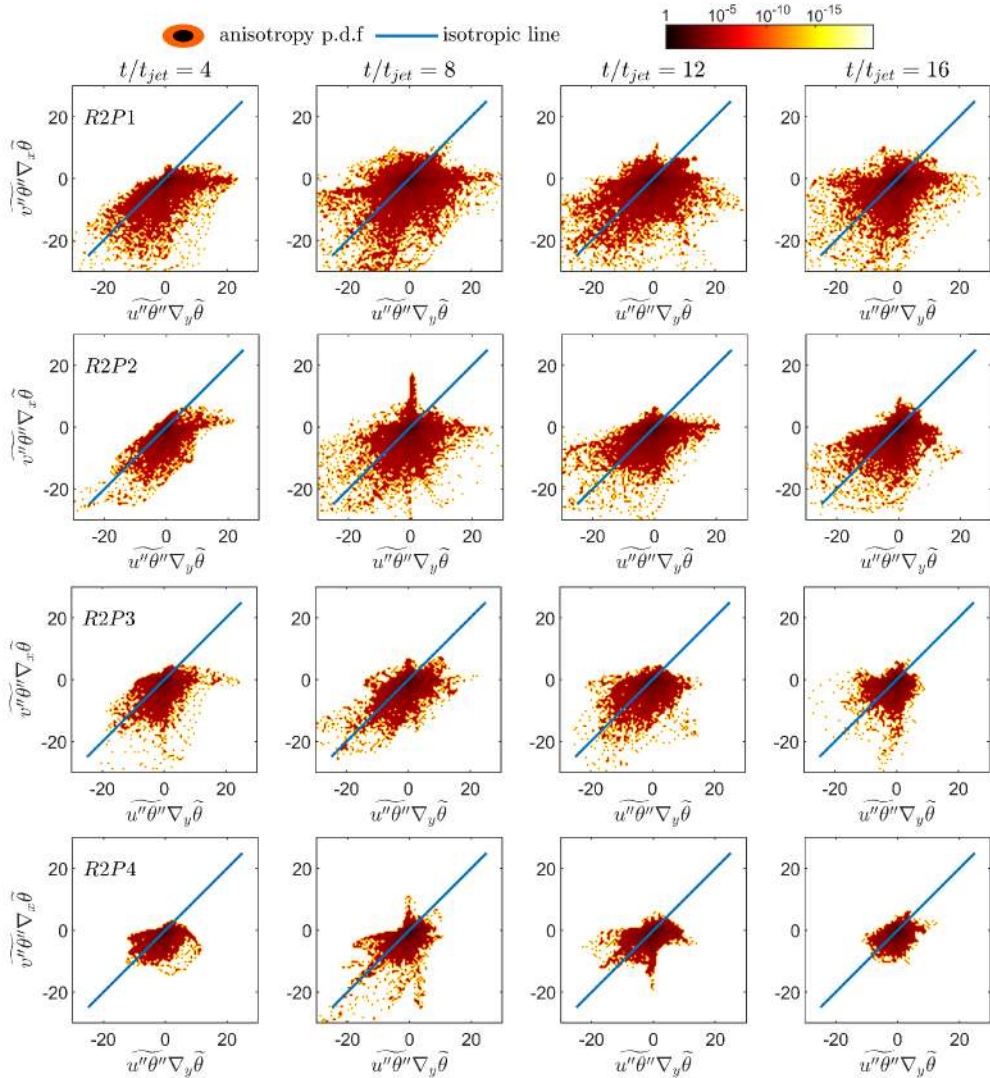


Figure 74: Joint pdf of the anisotropy computed at all 4-reduced pressure levels and their 4-respective time instances.

4.7 SUMMARY

Summary

- Some important signatures during the transition from liquid-like to gas-like, especially as it crosses the Widom line are peak in isobaric specific heat capacity, strongest density gradient with respect to temperature, highest iso-thermal compressibility, poorest thermal diffusivity, and highest molecular Prandtl number, these signatures become even more evident at near-to-the critical point.
- The molecular Pr (ratio of momentum diffusivity and thermal diffusivity), usually assumed to be close to unity for gases indicating is not true for transcritical nitrogen jet, where its value in the vicinity of pseudo-boiling temperature reaches close to 6.

- The temperature sensitivity of C_p strongly depends on pressure, and becomes even more rapid as temperature approaches to the critical point, implying that much more energy is needed to heat up the fluid across Widom line as such isobaric process is nearer to the critical point. At the critical point, the C_p theoretically stretches to infinity.
- The initial disturbance in the flow field by the injection triggers a shear layer instabilities while it grows giving raise to a large scale structures popularly known as Kelvin-Helmoltz (KH), these large scale instabilities are due to shearing induced by large velocity and density gradients.
- The liquid-like jet core remains in its liquid-like state until significant amount of time for near-to-the critical transcritical injection, which is not true for the far-from-the critical point injection.
- The sharp peak of isobaric specific heat in the near-to-the critical point refers to significantly large contribution of the structural energy, which is required to overcome for the transition, and it acts as a heat-shield (the process known as solid-wall effect) in the near-to-the critical point injection, so the liquid jet core remains in liquid like state for significant time (in temporal) or length (for spatial) simulations. Such effect reduces, for higher pressure regime, so that the process of pseudo-vaporization is fast with faster vanishing liquid jet core.
- The solid-wall in the flow that reduces the velocity fluctuations in the cross-wise direction and amplifies in the stream-wise direction. This behaviour allows the transfer of the turbulent kinetic energy from its cross-wise component to the stream-wise component. This process of energy redistribution among spatial components due to solid wall effect as a consequence of density stratification, significantly modifies the amount of available energy for fluid mixing at the density interface.
- Reynolds and Favre averages are pretty much same in the region of low variance such as jet core and undisturbed region while they exhibit different behaviour in the mixing zone.
- The β - function distribution can describe the pdf of the DNS data considerably well at low variance but deviates at higher variances. Also the Dirac-delta function performs very poor the mixing dominated regions, as it completely ignores the contribution of sub-grid scales.

- The turbulent Prandtl number value peaks as maximum as 2.5 in R2P1 (characterized by maximum thermodynamic nonlinearities) and R2P4 (characterized by intense mixing). However, its average value is within the classical assumption between 0.5 and 1.
- The linearity between the turbulent heat flux and the temperature gradient (i.e. linear eddy hypothesis) is found to be violated in the pressure closer-to-the critical point while more linear (isotropic) behaviour is found in far-from-the critical point.

5 Summary and Outlook

The primary objective of the present work was to understand the pressure dependencies on the mixing process of an inert element (nitrogen) under high-pressure conditions. Such conditions are becoming more and more popular these days in modern engineering applications such as in liquid rocket engines, modern diesel engines, carbon free power generation system, gas turbines, etc. due to higher efficiency and compactness. The operating pressure and temperature of such devices are well above the critical pressure and temperature of the operating fluid (propellants, in LREs), which are usually stored in a compressed liquid state at low sub-critical temperatures to allow for high densities and compact storage, prior to the injection. The injection of such compressed propellants into high pressure-temperature environments has typically been described by turbulent dense fluid mixing with no surface tension, which is in contrary to classical jet disintegration followed by atomization process. With multi-component systems this phenomenon get even more complicated and might undergo both of the above behaviours due to absence of a single critical point in multi-component system. In fact, the critical pressure of a mixture often exceeds many times the critical pressure of the pure components, causing the existence of sub-critical regions in the flow even though the operating pressure is well above the critical pressure of the injected propellants.

Such complex process govern by turbulent mixing (and thermo-chemistry for a reacting flow) is extremely difficult to study to its minute detail with experimental procedures, due to harsh conditions like that in LREs, gas-turbines and diesel engines. However, the development of highly advanced laser spectroscopy technique has and will contribute in studying such process in an extreme pressure conditions. The other way to study such behaviour is with numerical tool, which can provide details insight into the physics of the flow. The present work involves the later methodology. The state-of-the art Direct Numerical Simulation (DNS) of trans-critical nitrogen injection capable of resolving the smallest scales both in space and time has been carried out by Prof. Dr. Francesco Creta and Dr. Pasquale E. Lapenna (La Sapienza University of Rome) with the grant at the Italian Super-Computing Inter-university Consortium CINECA for support and high-performance computing resources under the Iscra B Grant DNS-LS. The accuracy of thermodynamic and the transport property was guaranteed by employing the reference nitrogen EoS - independent low-Mach number version of the open source, massively parallel code nek5000 which is based on high-order numerical framework based on Spectral Element Method (SEM).

One of the challenges with the DNS is huge data generated from the numerical computation ($\sim 1TB$ in the present work). Such data needs careful post-processing to acquire the useful informations on the statistics. I've been involved with such post-processing the the generated DNS dataset and thus, the results presented in this thesis are obtained from the same. With the help of such statistical analysis, the behaviour of the flow can be studied in detail plus it is also possible to validate the current popular numerical models employed in less computationally intensive numerical techniques like Reynolds Averaged Navier-Stokes (RANS) and Large Eddy Simulation (LES), where the contribution of small scales are usually modelled. Such numerical models are ad hoc and are suited the best in a particular situation while they might be totally wrong in some other cases or vice-versa. Therefore, it is very important to validate the accuracy of such numerical models in the case of high pressure conditions such as the transcritical injection, so that RANS and LES perform well in such flow analysis. This has been one of the objective of the present thesis work.

The numerical simulation so carried out was of temporally evolving nitrogen planar jet injected into a cubical configuration with a warm nitrogen at four different pressure conditions. One near-to-the critical point of nitrogen all the way upto far-from the critical point. Note that all the simulations were carried out at the same Reynolds number. This allows us to understand the pressure dependencies in the mixing process. The first part of the result analysis discuss in the present thesis work involves the general overview to the simulation configuration, followed by the averaged flow field and variance which gives an important illustration of the solid-wall effect which acts as a heat-shield which restricts the velocity fluctuations in crosswise direction while amplifying them in the streamwise direction, changing the energy distribution of the flow field and thus modifying the dynamics of the mixing layer.

It is thereafter followed by investigation of the statistical modelling, in particular the use of pre-assumed pdf of temperature to compute the thermodynamic variables like isobaric specific heat and density. The results show that the performance of β -pdf based on pre-assumed mean and variance is way better as compared to that no-model approximation (which completely ignores the sub-grid scale contributions). Its performance is even better in the region characterised by low variance. The very important quantities in the study of mixing such as the Reynolds stress, Turbulent heat flux and the Turbulent Prandtl number has also been studied and discussed for all the pressure levels.

Last but not least, the behaviour of the anisotropy of the turbulent heat fluxes with pressure is analysed and discussed. The popularly assumed isotropic behaviour of heat fluxes (in the linear eddy diffusivity hypothesis, used in RANS simulation) is questionable in the flow with large thermody-

namic non-linearities like that in the present work. This hypothesis has been put in test and explored in this thesis. The results show that the near-to-the critical point with largest thermodynamic non-linearities has the largest level of anisotropy while far-from the critical point show more isotropic behaviour. This suggests need for careful and better turbulent heat flux modelling especially in the case near-to the critical point.

Some of the future work worth carrying out are;

- More statistical analysis to study the sub-grid scale contribution to study the validation of SGS models and filtering techniques with the present DNS dataset,
- The simulations at higher Reynolds number this allows the study of more intensive mixing (closer to realistic engineering applications) induced due to larger shear along with thermodynamic non-linearities,
- DNS of multi-component transcritical injection (very much like propellant injection e.g. H and O) either or both in cold or reacting configurations

Part IV
BIBLIOGRAPHY

Bibliography

- [1] **Aleksandar Vujinović** (2015)
Kelvin-Helmholtz Instability Seminar on Kelvin-Helmholtz Instability, Department of Physics, Univerza V Ljubljani.
- [2] **Bellan, J.** (2000)
Supercritical (and subcritical) fluid behavior and modeling: drops, streams and mixing layers, jets and sprays. Progress in Energy and Combustion Science, pages 329–366.
[https://doi.org/10.1016/S0360-1285\(00\)00008-3](https://doi.org/10.1016/S0360-1285(00)00008-3)
- [3] **Miller, R. S., Harstad, K. G., & Bellan, J.** (2001)
Direct numerical simulations of supercritical fluid mixing layers applied to heptane-nitrogen. In Journal of Fluid Mechanics (Vol. 436).
<https://doi.org/10.1017/S0022112001003895>
- [4] **Bellan, J.** (2006)
Theory, modeling and analysis of turbulent supercritical mixing. Combustion Science and Technology, 178:253–281.
<https://doi.org/10.1080/00102200500292241>
- [5] **Bellan, J.** (2017)
Direct numerical simulation of a high-pressure turbulent reacting temporal mixing layer. Combustion and Flame, 176, 245–262.
<https://doi.org/10.1016/j.combustflame.2016.09.026>
- [6] **Gnanaskandan, A. & Bellan, J.** (2017)
Numerical Simulation of Jet Injection and Species Mixing under High-Pressure Conditions. Conference: 1st International Seminar on Non-Ideal Compressible-Fluid Dynamics for Propulsion & Power, Volume: 821
<https://doi.org/10.1088/1742-6596/821/1/012020>
- [7] **Banauti, D. T.** (2015)
Thermodynamic Analysis and Numerical Modeling of Supercritical Injection, PhD dissertation- University of Stuttgart.
- [8] **Banauti ,D. T.** (2015)
(2015). *Crossing the Widom-line - Supercritical pseudo-boiling*, Journal of Supercritical Fluids98, 12–16.
<https://doi.org/10.1016/j.supflu.2014.12.019>
- [9] **Banuti, D. T., Raju, M., Ma, P. C., Ihme, M., & Hickey, J. P.** (2017)
Seven questions about supercritical fluids – towards a new fluid state

diagram. AIAA SciTech Forum - 55th AIAA Aerospace Sciences Meeting, (January), 1–15.

<https://doi.org/10.2514/6.2017-1106>

- [10] **Banuti, D. T., Hannemann, V., Hannemann, K., and Weigand, B.** (2016) *An Efficient Multi-Fluid-Mixing Model for Real Gas Reacting Flows in Liquid Propellant Rocket Engines*, Combustion and Flame, Vol. 168, June 2016, pp. 98–112.
[doi:10.1016/j.combustflame.2016.03.029](https://doi.org/10.1016/j.combustflame.2016.03.029)
- [11] **Bianchi D.** (2016-17) *Chemical Rocket Propellant Performance Analysis*, Notes on Space Propulsion, La Sapienza University of Rome.
- [12] **Mayer W, Telaar J, Branam R, Schneider G.** (2001) *Characterization of cryogenic injection at supercritical pressure*. AIAA paper 2001-3275 <https://doi.org/10.2514/2.6138>
- [13] **Carbone, M., & Bragg, A. D.** (2019) *Is vortex stretching the main cause of the turbulent energy cascade?* <http://arxiv.org/abs/1906.07144>, (2019).
- [14] **Chehroudi B.** (2012) *Recent experimental efforts on high-pressure supercritical injection for liquid rockets and their implications*. International Journal of Aerospace Engineering Volume 2012, Article ID 121802, 31 pages <https://doi.org/10.1155/2012/121802>
- [15] **Chen, C.-S., Chang, K. C. & Chen, J.-Y.** (1994) *Application of a Robust β -pdf Treatment to Analysis of Thermal NO Formation in Nonpremixed Hydrogen-Air Flame* Combust. Flame, Vol. 98, pp. 375–390.
[https://doi.org/10.1016/0010-2180\(94\)90176-7](https://doi.org/10.1016/0010-2180(94)90176-7)
- [16] **Chong, S. T., Tang, Y., Hassanaly, M., & Raman, V.** (2017) *Turbulent mixing and combustion of supercritical jets*. AIAA SciTech Forum - 55th AIAA Aerospace Sciences Meeting, (January).
<https://doi.org/10.2514/6.2017-0141>
- [17] **Chung K Law** (2012) *Combustion Physics*. In Cambridge University Press, (Princeton University) (Vol. 66).
- [18] **Chung,T.H., Mohammad Ajlan, Lloyd L. Lee, Kenneth E. Starling** (1988) *Generalized multiparameter correlation for nonpolar and polar fluid transport properties*, Eng. Chem. Fundamen., 27:671–679, 1988.
<https://doi.org/10.1021/ie00076a024>

- [19] **Cox, J. D., D. D. Wagman, and V. A. Medvedev** (1989)
CODATA Key Values for Thermodynamics, Final Report of the CO-DATA Task Group on Key Values for Thermodynamics Hemisphere, New York, 1989.
- [20] **Datt P.** (2011)
Latent Heat of Vaporization / Condensation
In: Singh V.P., Singh P., Haritashya U.K. (eds) Encyclopedia of Snow, Ice and Glaciers. Encyclopedia of Earth Sciences Series. Springer, Dordrecht https://doi.org/10.1007/978-90-481-2642-2_327
- [21] **Davidson, L., & Billson, M.** (2006)
Hybrid LES-RANS using synthesized turbulent fluctuations for forcing in the interface region.
International Journal of Heat and Fluid Flow, 27(6), 1028-1042.
<https://doi.org/10.1016/j.ijheatfluidflow.2006.02.025>
- [22] **D'angelo G., Lissauer, J. J.** (2018)
Formation of Giant Planets, Handbook of Exoplanets. Springer International Publishing AG, part of Springer Nature. pp. 2319–2343 - 2018,
https://doi.org/10.1007/978-3-319-55333-7_140
- [23] **Diez A.** (2018)
Liquid water on Mars, Insight,
3 August 2018 Vol 361 Issue 6401. Pg.444-449.
- [24] **Fischer, P. F., Lottes, J.W., and Kerkemeier, S. G.** (2008)
“nek5000Web Page,” <http://nek5000.mcs.anl.gov>
- [25] **Gratton, Julio.** (1991)
Similarity and self similarity in fluid dynamics. Fundamentals of Cosmic Physics 15 (1991): 1-106.
- [26] **Jeremy A. Gibbs** (2016)
LES of turbulent flows: Lecture 5, University of Utah, Fall 2016.
- [27] **F. Gorelli, M. Santoro, T. Scopigno, M. Krisch, & G. Ruocco** (2006)
Liquid-like behavior of supercritical fluids. Physical Review Letters, 97:245702–1 – 245702–4, 2006
<https://doi.org/10.1103/PhysRevLett.97.245702>
- [28] **Hanasz, M., & Sol, H.** (1996)
Kelvin-Helmholtz instability of stratified jets Astronomy and Astrophysics, 315(3), 355–364.
<https://arxiv.org/abs/astro-ph/9604156>
- [29] **Dr. Sven Horstmann** (2000)
Persönlich übergeben von Sven Horstmann. In ähnlicher Form verwendet in: Horstmann S., "Theoretische und experimentelle Untersuchungen zum.

- [30] **Huzel and Huang** (1971)
Design of Liquid Propellant Rocket Engine, AIAA (American Institute of Aeronautics & Astronautics); NASA (1971).
- [31] **Hosangadi,A., Lee,C., Kannepalli,C., and Arunajatesan,A.** (2008)
Three-Dimensional Hybrid RANS/LES Simulations of a Supercritical Liquid Nitrogen Jet, AIAA paper 2008– 5227; 2012,
<https://doi.org/10.2514/6.2008-5227>
- [32] **Kerkemeier, Stefan Georg** (2010)
Direct numerical simulation of combustion on petascale platforms: Application to turbulent non-premixed hydrogen auto-ignition, Doctoral thesis submitted at ETH Zürich
[https://doi.org/10.3929/ethz-a-006194036 Rights](https://doi.org/10.3929/ethz-a-006194036)
- [33] **Karus A. et. al.** (2011)
Introduction to thermal and fluid engineering, Allan D Kraus, James R. Welty, and Abdul Aziz, 2011.
- [34] **Lamioni, R.** (2016)
Numerical Investigation of Hydrodynamic Instability in Turbulent Premixed Flames A Masters thesis submitted at La Sapienza University of Rome
- [35] **Lemmon, E., Huber, M., and McLinden, M.** (2007)
Refprop: Reference Fluid Thermodynamic and Transport Properties, NIST Standard Reference Database, Vol. 23, No. 8, 2007
- [36] **Lemmon, E., and Jacobsen, R.** (2004)
Viscosity and Thermal Conductivity Equations for Nitrogen, Oxygen, Argon, and Air, International Journal of Thermophysics, Vol. 25, No. 1, 2004, pp. 21–69.
<https://doi.org/10.1023/B:IJOT.0000022327.04529.f3>
- [37] **Malasekera, H. K. V. and W.** (2005)
An Introduction to Computational Fluid Dynamics: The Finite Volume Method. In IEEE Concurrency (Vol. 6).
<https://doi.org/10.1109/mcc.1998.736434>, 2005.
- [38] **Maries A., MD. A. Haque, S. L. Yilmaz, M. B. Nik, G. E. Marai** (2012)
Interactive Exploration of Stress Tensors Used in Computational Turbulent Combustion
https://doi.org/10.1007/978-3-642-27343-8_7
- [39] **Mayer, W., & Tamura, H.** (1996)
Propellant injection in a liquid oxygen/gaseous hydrogen rocket engine. Journal of Propulsion and Power, 12(6), 1137–1147.
<https://doi.org/10.2514/3.24154>

- [40] **Mayer W., Schik A., Vielle V., Chauveau C., Gokalp I.,Talley D.G., & Woodward R.D.** (1998) *Atomization and breakup of cryogenic propellants under high-pressure subcritical and supercritical conditions.* Journal of Propulsion and Power, 14:835–842, (1998).
<https://doi.org/10.2514/2.5348>
- [41] **Mayer, W. & Telaar, Jürgen & Branam, Richard & Schneider, G. & Hussong, J.** (2003) *Raman Measurements of Cryogenic Injection at Supercritical Pressure.* Heat and Mass Transfer. 39. 709-719.
<https://doi.org/10.1007/s00231-002-0315-x>
- [42] **McMillan, P. F., & Stanley, H. E.** (2010). *Fluid phases: Going supercritical.* Nature Physics, 6(7),479–480.,
<https://doi.org/10.1038/nphys1711>
- [43] **Moin P., & Kim J.** (1997) *Tackling turbulence with supercomputers.* Scientific American, 276(1), 46–52. (1997)
<https://doi.org/10.1038/scientificamerican0197-62>
- [44] **Moin, P., & Mahesh, K.** (1998) *Direct Numerical Simulation : A Tool in Turbulence Research.*
<https://doi.org/10.1146/annurev.fluid.30.1.539>
- [45] **Müller, H., Pfitzner, M., Mattheis, J., & Hickel, S.** (2016) *Large-eddy simulation of coaxial LN2/GH2 injection at trans- and supercritical conditions.* Journal of Propulsion and Power, 32(1), 46–56.
<https://doi.org/10.2514/1.B35827>
- [46] **Nash K.L. et al.** (2017) *Nature Ecol. Evol-1* 1625 (2017).
- [47] **Nowak, P., R. Kleinrahm, & W. Wagner** (1997) *Measurement and correlation of the (p,ρ,T) relation of nitrogen. II. Saturated-liquid and saturated-vapour densities and vapour pressures along the entire coexistence curve* J. Chem. Thermodyn. 29, 1157-1997,
<https://doi.org/10.1006/jcht.1997.0231>
- [48] **Oefelein, Joseph C., & Vigor Yang.** (1998) *Modeling high-pressure mixing and combustion processes in liquid rocket engines.* Journal of Propulsion and Power 14.5 (1998): 843-857.
<https://doi.org/10.2514/2.5349>
- [49] **N. Okong'0 & J. Bellan** (2002) *Direct numerical simulation of O₂/H₂ tem- poral mixing layers under supercritical conditions.* AIAA Journal, 40:914–926
<https://doi.org/10.2514/6.2002-779>

- [50] **Orszag, S. A. and Patera, A. T.** (1984)
Spectral Element Method for Fluid Dynamics: Laminar Flow in a Channel Expansion, Journal of Computational Physics, Vol. 54, p. 468.
[https://doi.org/10.1016/0021-9991\(84\)90128-1](https://doi.org/10.1016/0021-9991(84)90128-1)
- [51] **Orszag, S. A. and Patterson, G. S.** (1972)
Numerical Simulation of Three-dimensional Homogeneous Isotropic Turbulence, Phys. Rev. Lett., Vol. 28, pp. 76–79.
<https://doi.org/10.1103/PhysRevLett.28.76>
- [52] **Oshawald M., Chehroudi B., & Talley D.** (2006)
Injection of fluids into supercritical environment, Combustion Science and Technology, 2006,
<https://doi.org/10.1080/00102200500292464>.
- [53] **Lapenna, P. E.** (2016)
Mixing and non - premixed combustion at supercritical pressures, PhD dissertation, La Sapienza University of Rome (2016).
- [54] **Lapenna, P. E., & Creta, F.** (2017)
Mixing under transcritical conditions: An a-priori study using direct numerical simulation. Journal of Supercritical Fluids, 128(May), 263–278.
<https://doi.org/10.1016/j.supflu.2017.05.005>
- [55] **Lapenna, P. E., & Creta, F.** (2019)
Direct numerical simulation of transcritical jets at moderate Reynolds number. AIAA Journal, 57(6), 2254–2263.
<https://doi.org/10.2514/1.J058360>
- [56] **Lapenna, P. E., Lamioni, R., Ciottoli, P. P., & Creta, F.** (2018)
Low-mach number simulations of transcritical flows AIAA Aerospace Sciences Meeting, 2018, (210059).
<https://doi.org/10.2514/6.2018-0346>
- [57] **Lapenna, P. E.** (2018)
Characterization of pseudo-boiling in a transcritical nitrogen jet. Physics of Fluids, 30(7).
<https://doi.org/10.1063/1.5038674>
- [58] **Lapenna, P. E., Indelicato, G., & Creta, F.** (2019)
The effect of pressure on transcritical jets : a DNS study.
<https://doi.org/10.13009/EUCASS2019-355>
- [59] **Ding-Yu Peng & Donald B. Robinson** (1976)
A New Two-Constant Equation of State, Industrial & Engineering Chemistry Fundamentals, 15(1):59–64, 1976.
<https://doi.org/10.1021/i160057a011>
- [60] **Peng, S. H., & Davidson, L.** (2002)
On a subgrid-scale heat flux model for large eddy simulation of turbulent thermal flow. International Journal of Heat and Mass Transfer,

- 45(7), 1393–1405.
[https://doi.org/10.1016/S0017-9310\(01\)00254-X](https://doi.org/10.1016/S0017-9310(01)00254-X)
- [61] **Pizzarelli, M.** (2018)
The status of the research on the heat transfer deterioration in super-critical fluids: A review. International Communications in Heat and Mass Transfer, 95(May), 132-138.
<https://doi.org/10.1016/j.icheatmasstransfer.2018.04.006>
- [62] **Pointot, T. & Veynante, D.** (2001)
Theoretical and Numerical Combustion. R.T. Ed- wards, Philadelphia, 2001
- [63] **Pope S. B.** (2000)
Turbulent Flows, Cornell University, New York, Cambridge University Press,
<https://doi.org/10.1017/CBO9780511840531>
- [64] **Raju, M., Banuti, D. T., Ma, P. C., & Ihme, M.** (2017)
Widom lines in binary mixtures of supercritical fluids. Scientific Reports, 7(1), 1–10.
<https://doi.org/10.1038/s41598-017-03334-3>
- [65] **Otto. Redlich & J. N. S. Kwong** (1949)
On the Thermodynamics of Solutions. V. An Equation of State. Fugacities of Gaseous Solutions. Chemical Reviews 1949 44 (1), 233-244
<https://doi.org/10.1021/cr60137a013>
- [66] **Ries F., Janicka J., & Sadiki A.** (2017)
Thermal Transport and Entropy Production Mechanisms in a Turbulent Round Jet at Supercritical Thermodynamic Condition, Entropy, 2017,
<https://doi.org/10.3390/e19080404>.
- [67] **Ries, F., Obando, P., Shevchuck, I., Janicka, J., & Sadiki, A.** (2017)
Numerical analysis of turbulent flow dynamics and heat transport in a round jet at supercritical conditions. International Journal of Heat and Fluid Flow, 66, 172–184.
<https://doi.org/10.1016/j.ijheatfluidflow.2017.06.007>
- [68] **M. Santoro and F.A. Gorelli.** (2008)
Structural changes in supercritical fluids at high pressures. Physical Review B, 77:212103–1 – 212103–4, 2008
<https://doi.org/10.1103/PhysRevB.77.212103>
- [69] **Selle, L., & Ribert, G.** (2008)
Modeling requirements for large-eddy simulation of turbulent flows under supercritical thermodynamic conditions. Proceedings of the Summer Program, 195–207. Retrieved from
http://ctr.stanford.edu/Summer/SP08/3_5_Selle.pdf

- [70] **Selle, L. C., Bellan, J., & Harstad, K. G.** (2007)
Novel subgrid modeling of the LES equations under supercritical pressure. 5th US Combustion Meeting 2007, 5, 3148–3166.
<https://doi.org/10.2514/6.2007-568>
- [71] **Singla, G., Scouflaire, P., Rolon, C., & Candel, S.** (2005)
Transcritical oxygen / transcritical or supercritical methane combustion. Proceedings of the Combustion Institute, 30(2), 2921–2928.
<https://doi.org/10.1016/j.proci.2004.08.063>
- [72] **Giorgio Soave** (1972)
Equilibrium constants from a modified Redlich-Kwong equation of state, Chemical Engineering Science, Volume 27, Issue 6, 1972, Pages 1197-1203, ISSN 0009-2509,
[https://doi.org/10.1016/0009-2509\(72\)80096-4.](https://doi.org/10.1016/0009-2509(72)80096-4)
- [73] **Stoll, R.** (2014)
LES of turbulent flows (ME EN 7960-003). University of Utah.
- [74] **Sutton G. P., & Seifert, H. S.** (2001)
Rocket Propulsion Elements 7th edition,. New York, John Wiley & Sons.
<https://doi.org/10.1063/1.3066790>
- [75] **Tani, H., Teramoto, S., Yamanishi, N., & Okamoto, K.** (2013)
A numerical study on a temporal mixing layer under transcritical conditions. Computers and Fluids, 85, 93–104.
<https://doi.org/10.1016/j.compfluid.2012.10.022>
- [76] **Terashima, H., Soshi K., & Nobuhiro Y.** (2011)
High-Resolution Numerical Method for Supercritical Flows with Large Density Variations. AIAA JOURNAL Vol. 49, No. 12, December 2011.
<https://doi.org/10.2514/1.J051079>
- [77] **Tian, R., Dai, X., Wang, D., & Shi, L.** (2018)
Study of Variable Turbulent Prandtl Number Model for Heat Transfer to Supercritical Fluids in Vertical Tubes Journal of Thermal Science, 27(3), 213–222.
<https://doi.org/10.1007/s11630-018-1002-7>
- [78] **Timmermans, LJP, Jansen, JKM & Vosse, van de, FN** (1990)
A description of the fundamentals of the spectral element method. DCT rapporten, vol. 1990.041, Technische Universiteit Eindhoven, Eindhoven.
- [79] **Trachenko K., Brazhkin V.V., & Bolmatov D.** (2014)
Dynamic transition of supercritical hydrogen: Defining the boundary between interior and atmosphere in gas giants, Physical Review E - Statistical, Nonlinear, and Soft Matter Physics, 89(3), 1–5.
<https://doi.org/10.1103/PhysRevE.89.032126>

- [80] **J.D. van der Waals.** (1873)
Over de Continuiteit van den Gas- en Vloeistoftoestand, PhD thesis, University of Leiden.
- [81] **Wagner, W., Span, R., Lemmon, E. W., Jacobsen, R. T., & Yokozeki, A.** (2000)
A Reference Equation of State for the Thermodynamic Properties of Nitrogen for Temperatures from 63 . 151 to 1000 K and Pressures to 2200 MPa. Journal of Physical and Chemical Reference Data, Vol. 29, No. 6, 2000, pp. 1361–1433.
<https://doi.org/10.1063/1.1349047>
- [82] **Wilcox, D. C.** (2006)
Turbulence Modeling for CFD.
<https://doi.org/10.1017/S0022112095211388>
- [83] **Wang, X., Huo, H., Unnikrishnan, U., & Yang, V.** (2018)
A systematic approach to high-fidelity modeling and efficient simulation of supercritical fluid mixing and combustion. Combustion and Flame, 195(May), 203–215.
<https://doi.org/10.1016/j.combustflame.2018.04.030>
- [84] **Yamagata, K., Nishikawa, S., Hasegawa, S., Fujii, T., & Yoshida, S.** (1972)
Forced convective heat transfer to supercritical water flowing in tubes. International Journal of Heat and Mass Transfer, 15(12), 2575–2593.
[https://doi.org/10.1016/0017-9310\(72\)90148-2](https://doi.org/10.1016/0017-9310(72)90148-2)
- [85] **Yoo, J. Y.** (2013)
The Turbulent Flows of Supercritical Fluids with Heat Transfer. Annual Review of Fluid Mechanics, 45(1), 495–525.
<https://doi.org/10.1146/annurev-fluid-120710-101234>
- [86] **Zistl, C.** (2014)
File-based post-processing of DNS results for turbulent flames using Matlab. PhD thesis submitted at Otto-von-Guericke-Universität Magdeburg; Retrieved from
<https://d-nb.info/1073584380/34>
- [87] **Zong N, Yang V.** (2006)
Cryogenic fluid jets and mixing layers in transcritical and supercritical environments. Combust Sci Technol 2006;178:193–227.
<https://doi.org/10.1080/00102200500287613>
- [88] **Zong, N., Meng, H., Hsieh, S. Y., & Yang, V.** (2004)
A numerical study of cryogenic fluid injection and mixing under supercritical conditions. Physics of Fluids, 16(12), 4248–4261.
<https://doi.org/10.1063/1.1795011>